

INVESTIGATING BLOOD FLOW AND ANTIBIOTIC DOSING USING TRADITIONAL  
MICROFLUIDICS AND NOVEL 3D PRINTED DEVICES

By

Jayda Erkal Meisel

A DISSERTATION

Submitted  
to Michigan State University  
in partial fulfillment of the requirements  
for the degree of

Chemistry – Doctor of Philosophy

2015

## ABSTRACT

### INVESTIGATING BLOOD FLOW AND ANTIBIOTIC DOSING USING TRADITIONAL MICROFLUIDICS AND NOVEL 3D PRINTED DEVICES

By

Jayda Erkal Meisel

Over the last 25 years, it has been established that the red blood cell (RBC) is a major determinant in blood flow, which it can modulate through release of adenosine triphosphate (ATP). Although RBCs store intracellular ATP in mM concentrations, measurements indicate that the cells release nM concentrations when stimulated by deformation, hypoxia (lowered oxygen tension), or incubation with pharmacological stimuli such as hydroxyurea (HU), which is the only approved drug for treatment of sickle cell disease. Upon release, RBC-derived ATP can induce vessel dilation via activation of endothelial cell nitric oxide synthase (eNOS) to produce nitric oxide (NO).

To probe the fate of increased ATP release from human RBCs incubated with the drug hydroxyurea, a traditional soft polymer platform was utilized to facilitate measurement of cell-to-cell communication between RBCs and a cultured endothelium. This device contained an array of micron-scale channels through which RBC samples were pumped. The sample flow was separated from a detection well by a porous polycarbonate membrane. Stimulated ATP released from the RBCs diffused across the membrane to the detection wells and was measured using the luciferin-luciferase chemiluminescence assay, integrated with a plate reader for detection. RBCs incubated with 100  $\mu$ M of HU released on average  $2.06 \pm 0.37$  times more ATP relative to the control sample. Through the use of various inhibitors, this increase in ATP release was subsequently demonstrated to depend on RBC deformability, RBC NOS activity, and the cystic fibrosis transmembrane conductance regulator protein (CFTR). The fate of the measured RBC-derived ATP was also investigated by probing ATP signalling to an adjacent cultured endothelium.

ATP release from RBCs increases in response to hypoxia, or lowered oxygen tension; however, the dependence of RBC ATP release on oxygen tension has not been investigated. To enable



measurement of RBC ATP release and oxygen tension in a flowing stream of RBCs, a 3D printed device was designed to accommodate commercial transwell inserts for ATP measurements, as well as threaded Clark-type electrodes for amperometric oxygen measurements. The device consisted of a channel 2 mm wide and 0.5 mm in height with two ports for analyte detection and one threaded port for an electrode. The Clark-type electrode was fabricated from gold and silver wires secured into a finger tight fitting. Oxygen standards and RBC samples were prepared using air and argon purged buffers. Using the 3D printed device, RBC ATP release and oxygen tension were measured simultaneously from prepared RBC samples. Relative to controls, RBC ATP release increased significantly in response to systematically lowered oxygen tension with a maximum increase of  $2.38 \pm 0.43$  fold more ATP when exposed to  $5.35 \pm 0.12$  ppm  $O_2$ . ATP release saturated, i.e., was not significantly different, at lower oxygen tensions. This increase in ATP release was inhibited by incubating RBCs with the cell stiffening agent, diamide. The dependence of hypoxic RBC ATP release on the conformation of heme in hemoglobin (Hb) is demonstrated by converting measured oxygen tensions to Hb saturation.

The 3D printed platforms presented herein were also utilized as *in vitro* tools to model pharmacokinetic dosing profiles, specifically with applications for studying antibiotic resistance. The World Health Organization, Centers for Disease Control, and the White House have issued reports that outline strategies to combat antibiotic resistance. The Spence lab has developed a 3D printed device to mimic *in vivo* drug dosing profiles on an *in vitro* platform for applications in drug discovery. This 3D printed diffusion-based dynamic dosing device mimics the dosing capabilities of the hollow fiber chamber reactor (HFCR). The *in vitro* 3D printed device contains 6 ports to house commercial polyester transwell membrane inserts (0.4  $\mu\text{m}$ ) and in house fabricated 0.2  $\mu\text{m}$  pore size inserts (polyester), which can be loaded with a sample of *Escherichia coli*. Chemically competent, kanamycin resistant *E. coli* were dosed with the DNA gyrase and topoisomerase IV inhibitor levofloxacin, which reached a maximum concentration ( $C_{max}$ ) of  $21.0 \pm 5.7$   $\mu\text{M}$  (0.4  $\mu\text{m}$  pore size) and  $68.5 \pm 5.0$   $\mu\text{M}$  (0.2  $\mu\text{m}$  pore size) of levofloxacin in approximately 1 hour. After dosing, the viability of the bacteria samples was measured using standard plating methods.

Copyright by  
JAYDA ERKAL MEISEL  
2015

To Zach

## ACKNOWLEDGEMENTS

I would like to thank the sources of funding that have supported me throughout my time in graduate school, specifically the National Institutes of Health, the College of Natural Science and The Graduate School. I would like to thank the Department of Chemistry for financial support as well as the Society for Laboratory Automation and Screening for travel support. I would also like to thank the MSU RTSF Mass Spectrometry Facility for instrument usage and also Brian Wright in the Department of Electrical and Computer Engineering for help with 3D printing.

Many thanks to the numerous faculty and staff in the Department of Chemistry who have entertained my questions, helped me with a request, or have helped me with instrumentation in the department. Specifically, I would like to acknowledge Tom Carter, Melissa Parsons, Bill Flick, and Bob Rasico, Glen Wesley, and Tom Geissinger (now retired). You all truly make the department a more enjoyable place to work.

I would also like to thank Kathy Severin, who I taught for by far the most time in graduate school. Teaching for her was such a great opportunity because pretty much all the practical knowledge of classical analytical instrumentation I learned was from her. I can't thank her enough for the time and effort she puts into training students (graduate and undergraduate). The protocol for HU detection in Chapter 2 would not have been possible to adapt without her expertise and advice.

I owe much of my specialized knowledge gained in graduate school to the former graduate students in the group. Suzanne Summers, Stephen Halpin, and Kari Brooke-Anderson were indispensable in passing practical laboratory knowledge down to younger students. I am truly indebted to them, as they took time out of their schedules to help me prepare for oral exams and conference presentations, and they always provided feedback. The nature of the work in the Spence lab depends highly upon team work, and so I would also like to say thank you to the current Spence group members: Bethany Gross, Sarah Lockwood, Kristen Entwistle, Chengpeng Chen, Yueli Liu, Suzanne Summers, Tiffany Bell, and Ruipeng Mu. Without their help, much of the work presented

in this thesis would not have been possible. Specifically, I would like to thank Sarah Lockwood for her work on the hydroxyurea and pharmacokinetics projects and also Tiffany Bell for help with mass spec. A big thank you goes to Suzanne Summers for always being willing to help and for her pep talks and Bethany Gross for research discussions and comedic relief. A special thank you goes to my hard-working undergraduate researchers Stephen McNamara and Eric Walton. I truly have enjoyed working with you all.

Outside the Spence lab, I would like to acknowledge Nicholas White. Nick was always willing listen to whatever research problem I was having. There are other graduate students who I would like to thank for making graduate school more enjoyable: Stephen Baumler, Omid Zandi, Steve Quinn, Anthony Schneider, and Kelley Young. I will miss playing softball in the summers and seeing you guys around the lab, and at Crunchy's.

I would also like to thank my advisor Dana Spence for guidance and encouragement. He may not agree with this statement, but I feel as though I have significantly improved my scientific writing and presentation skills over the last 5 years. He makes it a point to give extensive feedback on presentations and papers, and I would like to thank him for the time he takes to meticulously go through presentations and drafts with every graduate student in the group including myself. His advising style is rare, and I appreciate the openness he has with all of his students. I feel that I have advanced as a scientist and as a person. I would also like to thank my committee (Dan Jones, John McCracken, and Kris Chan) for providing valuable feedback.

The last year of graduate school was difficult, and I would like to thank my family. Specifically, thanks to Becky and Paul, Johnna and Will, and Katy and Collin for being incredibly supportive. I would also like to thank Sofi, Larry, and Reggie for their companionship. None of this would be possible without the support of my father, whose commitment to my education, from grade school to graduate school, was unwavering. Finally, I would like to thank Zach. Thank you for being an engaging fellow scientist, a loving and supportive husband, and my best friend. I am looking forward to our conversations being just as enjoyable when we are old as they are now. I am the luckiest.

## TABLE OF CONTENTS

LIST OF TABLES . . . . .	xi
LIST OF FIGURES . . . . .	xii
CHAPTER 1 INTRODUCTION . . . . .	1
1.1 The Red Blood Cell . . . . .	1
1.1.1 Physical Properties . . . . .	1
1.1.2 Properties of the Membrane . . . . .	2
1.1.3 Metabolism . . . . .	2
1.2 Roles in the Circulation . . . . .	4
1.2.1 The RBC as an O <sub>2</sub> Carrier . . . . .	4
1.2.1.1 Hemoglobin . . . . .	5
1.2.2 The RBC as a Regulator of pH . . . . .	8
1.2.3 Regulator of Vascular Tone . . . . .	9
1.2.3.1 The RBC as a Direct Regulator of Vascular Tone (RBC NO Induced Vessel Dilation) . . . . .	9
1.2.3.2 RBC-Derived ATP as a Mediator of Vessel Dilation . . . . .	12
1.3 Physiological Significance: RBC ATP Release as an Indicator of Disease . . . . .	13
1.3.1 Diabetes, Cystic Fibrosis, and Multiple Sclerosis . . . . .	13
1.3.2 Motivations . . . . .	14
CHAPTER 2 MONITORING RBC-ENDOTHELIAL CELL SIGNALING IN A MI- CROFLUIDIC DEVICE: IMPLICATIONS FOR THE TREATMENT OF SICKLE CELL DISEASE . . . . .	16
2.1 Hydroxyurea Use in the Treatment of Sickle Cell Disease . . . . .	16
2.1.1 Hypothesized Mechanisms of Action of Hydroxyurea . . . . .	17
2.1.2 Effect of Hydroxyurea on RBCs . . . . .	18
2.1.3 Multilayer Fluidic Devices to Monitor Cell-to-Cell Communication . . . . .	19
2.1.4 Probing the HU-RBC Interaction by Measuring HU Uptake . . . . .	20
2.1.5 Motivations . . . . .	21
2.2 Methods . . . . .	21
2.2.1 Collection and Purification of RBCs . . . . .	21
2.2.2 Endothelial Cell Culture . . . . .	21
2.2.3 Preparation of RBC ATP Release Agonists, Antagonists, and Reagents . . . . .	23
2.2.4 Preparation of Extracellular NO Probe DAF-FM and Reagents . . . . .	23
2.2.5 Fabrication of Microfluidic Devices . . . . .	24
2.2.6 Chemiluminescence Assay to Measure ATP Release . . . . .	27
2.2.7 Fluorescence Measurement of NO Release from a Cultured Endothelium . . . . .	29
2.2.8 HU-Incubated RBC Preparation for GC-MS Analysis . . . . .	29
2.2.9 GC-MS Instrumentation . . . . .	30
2.2.10 Treatment of Data . . . . .	31

2.3	Results and Discussion . . . . .	32
2.3.1	Flow-Induced Deformation is Required for ATP Release from HU-Incubated RBCs . . . . .	32
2.3.2	HU-Induced ATP Release from Human RBCs on a Microfluidic Device . .	33
2.3.3	ATP-Mediated NO release from bPAECs . . . . .	35
2.3.4	Measuring HU Uptake by RBCs . . . . .	35
2.4	Conclusions and Future Work . . . . .	37
CHAPTER 3 3D PRINTED TECHNOLOGIES TO ENABLE STUDY OF HYPOXIA-INDUCED RELEASE OF RBC SIGNALLING MOLECULES . . . . .		40
3.1	Hypoxia-Induced ATP Release: A Deformation-Induced Stimulus . . . . .	40
3.2	3D Printed Devices for Applications in Chemistry . . . . .	41
3.3	Classical Oxygen Detection Methods and Integration with Microfluidics . . . . .	45
3.4	Controlling Oxygen Tension in a Flowing Sample . . . . .	47
3.5	Methods . . . . .	49
3.5.1	Fabrication of 3D Printed Device . . . . .	49
3.5.2	Fabrication of Electrodes and Surface Modifications . . . . .	50
3.5.2.1	Au and Ag/AgCl Electrode for Oxygen Measurements . . . . .	50
3.5.2.2	Pt/Pt-black Electrodes for Measurement of NO . . . . .	53
3.5.3	Preparation of Reagents . . . . .	53
3.5.3.1	Oxygen Standards . . . . .	53
3.5.4	Preparation of RBC Samples . . . . .	54
3.5.4.1	NO Standards . . . . .	55
3.5.5	Electrochemical Methods . . . . .	55
3.5.5.1	Voltammetric Measurements . . . . .	55
3.5.5.2	Chronoamperometric Measurements . . . . .	57
3.5.5.3	Flow Injection Analysis . . . . .	57
3.6	Results and Discussion . . . . .	58
3.6.1	Validation of Oxygen Electrode Using Electrochemical Methods . . . . .	58
3.6.2	Validation of Oxygen Electrode Using Potassium Ferricyanide . . . . .	58
3.6.3	Validation Using Oxygen Standards with and without RBCs . . . . .	59
3.6.4	Measuring Oxygen Tension in Hypoxic RBC Samples . . . . .	61
3.6.5	Measuring ATP Release from Hypoxic RBC Samples in a 3D Printed Device	63
3.6.6	Correlating RBC ATP Release with Oxygen Tension . . . . .	64
3.7	Measuring NO Release Released From Hypoxic RBCs . . . . .	67
3.7.1	NO Detection Using a Pt-black Electrode Integrated with a 3D Printed Microfluidic Device . . . . .	68
3.7.2	NO Measurements Using Pt-black Modified Glassy Carbon Electrodes Integrated with a Planar Soft Polymer Microfluidic Device . . . . .	69
3.8	Conclusions and Future Work . . . . .	72
3.8.1	Mechanism of Hypoxic ATP Release . . . . .	72
3.8.2	Mechanism of Hypoxic Vasodilation . . . . .	73
3.8.3	Correlating RBC NO Release with Oxygen Tension for Stored Blood Applications . . . . .	73
3.8.4	High Throughput Potential . . . . .	74

CHAPTER 4	<i>IN VITRO</i> DYNAMIC DOSING OF <i>ESCHERICHIA COLI</i> WITH LEV- OFLOXACIN USING A 3D PRINTED MICROFLUIDIC DEVICE CA- PABLE OF GENERATING PHARMACOKINETIC CURVES . . . . .	76
4.1	Antibiotic Resistance . . . . .	76
4.2	<i>In Vitro</i> Models of Dynamic Dosing . . . . .	77
4.3	Methods . . . . .	81
4.3.1	Fabrication of Devices . . . . .	81
4.3.2	Preparation of Reagents . . . . .	83
4.3.3	Monitoring Levofloxacin Concentration Using Liquid Chromatography Mass Spectrometry . . . . .	84
4.3.4	Bacteria Growth and Purification . . . . .	85
4.3.5	Dosing Methods . . . . .	86
4.3.6	Standard Plating Methods . . . . .	87
4.4	Results and Discussion . . . . .	88
4.4.1	Confirmation of <i>E. coli</i> Viability in Device . . . . .	88
4.4.2	Dosing <i>E. coli</i> with Dynamic Profiles of Levofloxacin . . . . .	89
4.4.3	Application to AMR . . . . .	92
4.5	Conclusions and Future Work . . . . .	92
4.5.1	Extension of the Existing Empirical Model . . . . .	92
4.5.2	Extending the Half Life for Levofloxacin to Better Mimic <i>In Vivo</i> Dose Profiles . . . . .	93
4.5.3	Multi-day Dosing of <i>E. Coli</i> or other Bacterial Strains . . . . .	93
CHAPTER 5	CONCLUSIONS . . . . .	94
5.1	Future of HU and Hypoxia Studies: Applications in Sickle Cell Disease and RBC ATP Release . . . . .	94
5.2	Blood and Bacteria: An <i>In Vitro</i> Model for Sepsis and Infections on Chip . . . . .	95
5.2.1	RBC Response to Sepsis . . . . .	96
5.2.2	Future of 3D Printed Device for Dynamic Dosing of Bacteria . . . . .	97
REFERENCES	. . . . .	100



## LIST OF TABLES

Table 1.1	Oxygen levels in various tissues in the human body. Values were compiled from literature reports and reviews. <sup>1-4</sup> . . . . .	5
Table 2.1	Comparison of parameters from studies on deformability of RBCs exposed to HU. Using the parameters listed and other known values including volume of blood in the human body (5 L), volume of an RBC (92 fL), and molar mass of HU (76.05 g/L), the moles of HU per RBC was calculated for each study. *This study directly measures ATP release from the RBC, which is an indirect measurement of RBC deformability. . . . .	18
Table 2.2	Parameters for GC-MS analysis of RBC samples incubated with HU. . . . .	31
Table 3.1	Preparation of oxygen standards. Oxygen concentrations in various units are listed for convenience. The ratio of air-purged and argon-purged solutions for each sample is also listed. . . . .	54
Table 4.1	Solvent program for detection of ciprofloxacin and levofloxacin using (A) methanol, (B) acetonitrile, and (C) 1% formic acid + water. . . . .	85
Table 4.2	Mass spectrometry parameters for detection of ciprofloxacin and levofloxacin. . .	85

## LIST OF FIGURES

Figure 1.1	Anaerobic glycolysis diagram. GLUT1 on the RBC membrane facilitates glucose flux into the cell. Glucose is then converted to lactate while producing a net gain of 2 ATP molecules. Glutathione cycling is also regulated by this pathway through generation of NADPH, and 2,3-BPG, an allosteric regulator of Hb, is generated as an intermediate. . . . .	3
Figure 1.2	Tense (T) and relaxed (R) states of hemoglobin. In the T state, the iron atom in the center of each heme is positioned out of the plane of the heme molecule. When oxygen binds, $\text{Fe}^{2+}$ oxidizes to $\text{Fe}^{3+}$ , and the Fe atom comes into the plane of the heme group. . . . .	6
Figure 1.3	The Hb Dissociation Curve and Relevant Oxygen Tensions <i>In Vivo</i> . The sigmoidal $\text{PO}_2$ - Hb dissociation curve for Adult Hemoglobin (HbA) (Left) highlights the cooperative binding of $\text{O}_2$ to HbA. The interaction is cooperative because as the oxygen tension in solution increases, Hb- $\text{O}_2$ increases non-linearly and in a sigmoidal fashion, which is a hallmark of cooperative binding. This indicates that as $\text{O}_2$ binds to Hb, it is easier for more $\text{O}_2$ to bind, until Hb is saturated. The relevant oxygen tensions are also displayed (Right) to set the context of the Hb- $\text{O}_2$ dissociation curve. Note that the physiologically relevant region of the curve lies between about 40 mmHg and 100 mmHg, between venous and arterial blood. . . . .	7
Figure 1.4	Empirical relationship relating partial pressure of oxygen to Hb saturation. $\text{SO}_2$ and $\text{PO}_2$ are Hb saturation and partial pressure of oxygen, respectively. The maximal error in Hb saturation values obtained from partial pressure measurements is 0.5%. . . . .	8
Figure 1.5	Cross section of a resistance vessel. In response to particular stimuli, such as hypoxia, the RBC can release nM quantities of ATP. This ATP can diffuse to the endothelium and bind $\text{P}_2\text{Y}$ receptors, increasing intracellular $\text{Ca}^{2+}$ and activating eNOS via $\text{Ca}^{2+}$ -calmodulin. NO is synthesized in the endothelial cells and subsequently released. The released NO diffuses to the adjacent smooth muscle cells and induces vasodilation. Alternative theories for hypoxic vasodilation suggest that NO released by RBCs in response to hypoxia diffuses through the endothelium and directly to the smooth muscle cells to induce vessel dilation. . . . .	10

Figure 1.6	Mechanism of hypoxic ATP release from the RBC. The signal cascade begins with activation of the G-protein coupled receptor on the surface of the RBC. How this activation occurs under hypoxic conditions is not established, but many postulate that deoxygenated Hb plays a role. Some even hypothesize that deoxygenation is a subset of deformation. The signal cascade activates the heterotrimeric G-protein subunits, which stimulate adenylyl cyclase, which induces an increase in intracellular (cAMP). Increased cAMP activates PKA which induces phosphorylation of CFTR. It is not established through which protein ATP is translocated. . . . .	13
Figure 2.1	Whole blood collection and RBC purification procedure. Whole blood is obtained via venipuncture from consenting, informed donors. The whole blood is centrifuged and plasma is aspirated from the tube as described. The packed RBCs are then transferred to a secondary tube with PSS or the appropriate buffer. The RBCs are centrifuged and aspirated twice more for a total of three washes with PSS. Once washed, packed RBCs are obtained, the hematocrit is measured, and the purified RBCs are ready for use. . . . .	22
Figure 2.2	Reaction of NO with extracellular probe DAF-FM. . . . .	24
Figure 2.3	Photolithographic fabrication of the silicon master and soft lithographic fabrication of polymer microfluidic devices. Masters were fabricated by spin coating photoresist as described. The completed polymer device for experiments was assembled by placing strips of polycarbonate membrane (0.4 $\mu\text{m}$ i.d.) over channels after which a blank PDMS slab with punched detection wells was placed on the top. The assembled device was baked for 10 minutes to establish a reversible seal. . . . .	25
Figure 2.4	Cross section of the microfluidic device adapted from Lockwood et al. The top panel displays the cross section of the whole microfluidic device. RBCs are flowed through a channel and are separated from the detection well by a porous, polycarbonate membrane (0.4 $\mu\text{m}$ i.d.). ATP that is released from the RBCs can diffuse across the membrane and can interact with cultured endothelial cells (Top). If DAF-FM is loaded into the wells with a cultured endothelium, bPAEC-derived NO can be measured (Middle). When the endothelium is not cultured in the detection well, RBC-derived ATP can be directly measured using LL (Bottom). . . . .	26
Figure 2.5	Chemiluminescence reaction of ATP with D-luciferin. The reaction requires the enzyme luciferase, $\text{Mg}^{2+}$ , and oxygen to go to completion. The luminescence signal can be collected with a photomultiplier tube in homemade systems or with commercial instrumentation such as a plate reader. . . . .	27

Figure 2.6	Experimental setup for flowing RBCs on the device in Figures 2.4. RBC samples were prepared offline as described and were loaded into 500 $\mu$ L syringes. After loading detection wells with the appropriate detection reagent (LL for ATP only or later DAF-FM for bPAEC NO only), syringes were loaded onto a syringe pump, and samples were flowed for 30 minutes. After the allotted time, the device was removed from the pump and taken to the plate reader for detection. . . . .	28
Figure 2.7	In-house system for measuring ATP release from RBCs. Samples and LL mixture were prepared as described and were loaded into 500 $\mu$ L syringes. Syringes were loaded onto a syringe pump and samples were pumped at 6 $\mu$ L/min through the capillary system. Sample and LL mix at the T-junction, and the reaction between ATP and the LL reagent occurs. The mixed sample flows a fixed distance to a PMT, where light from the reaction can be detected. Data is displayed and saved using a Labview program. Image is not to scale. . . . .	29
Figure 2.8	Representative chromatograms and mass spectra of derivatized HU and naphthalene with and without SIM. Note that the background from derivatization reagent and resulting products dominate the chromatogram, making SIM necessary to quantify the derivatized product of HU. . . . .	32
Figure 2.9	ATP Release from 7% RBCs under static (non-flow) conditions (left) and under flow conditions (right). <sup>5</sup> 7% RBCs were incubated with and without 100 $\mu$ M HU for 30 minutes. The static ATP release was measured by mixing equal volumes of LL and sample and then reading the resulting chemiluminescence using a plate reader (N = 3 plates. Error is S.E.M.). ATP release from HU-incubated human RBCs was not significantly different than controls under static conditions. HU-incubated human RBCs released significantly more ATP relative to controls when pumped through silica capillary tubing. Flow data was collected using the method outlined in Figure 2.7. ATP release from RBCs increased with increasing concentration of HU until about 100 $\mu$ M HU. With more HU added to the sample, the RBC ATP release decreased to basal levels, which suggests that HU can act to either increase RBC deformability or to stiffen the cell. N $\geq$ 3 donors, except 150 $\mu$ M (N = 2) and Ca <sup>2+</sup> free (N = 1). Error is S.E.M. . . . .	33
Figure 2.10	ATP Release from human RBCs incubated with HU and with various inhibitors. <sup>5</sup> Data were collected by employing the device shown in Figure 2.6. When incubated with HU, 7% RBCs released significantly more ATP (2-fold more) than controls (*p < 0.001). When 7% RBCs were incubated with various inhibitors, ATP release significantly decreased in all inhibitor trials with or without HU incubation (p < 0.05) regardless of the presence of HU. N $\geq$ 3 donors. Error is S.E.M. . . . .	34

Figure 2.11	NO Release from cultured bPAECs stimulated with 7% RBCs incubated with and without HU. <sup>5</sup> When 7% RBCs incubated with HU are flowed under a cultured endothelium, the NO released from the endothelium increases approximately by 30% compared to controls (first set of bars). When the P <sub>2</sub> Y receptor of the endothelium is blocked using the antagonist PPADS, the NO release from the endothelium decreases significantly (second set of bars). When NOS in the endothelial cell is inhibited with competitive inhibitor L-NAME, NO release is also lowered (third set of bars), as is the case when RBCs are incubated with L-NAME (fourth set of bars) and when both RBCs and endothelial cells are incubated with the NOS inhibitor (fifth set of bars). The asterisk (*) indicates that the NO release from bPAECs incubated with HU is statistically different than the release observed in controls and in all inhibitor samples. N ≥ 3 donors. Error is S.E.M.*p < 0.005. . . . .	36
Figure 2.12	HU uptake by RBCs. RBCs were incubated with 0 and 100 μM HU in PSS for 1 hour after which the extraction method described was performed. Measurement of supernatant HU suggests that the RBCs incubated with HU for 1 hour uptake nearly all HU in the sample. N = 2 donors. Error is S.E.M. . . . .	37
Figure 3.1	3D printing process from part file to device printing and cleaning. . . . .	49
Figure 3.2	Device to measure dissolved oxygen and ATP in a flowing sample. <sup>6</sup> The device has threaded ports for sample introduction and a channel (7 mm x 3 mm x 0.5 mm) through which samples were flowed. The device also has two wells to hold transwell membrane inserts for ATP detection and another threaded port to accommodate the oxygen electrode. All threading was fabricated during the printing process, i.e., threads were not tapped into the device post-print. A side profile of the device is shown in (A) a top view in (B) and a solid body profile in (C). The right panel of the figure shows the actual device with inlet, channel and threaded electrode port printed in VeroClear in (D), the transwell insert sitting in the detection wells in (E), and the arrangement of the electrodes in the channel when the electrode assembly is screwed into the device in (F). . . . .	51
Figure 3.3	Fabrication of PEEK embedded electrodes for Oxygen Detection. Microscopy images of Au and Ag/AgCl electrodes detailing surface and position in the PEEK fitting (left and middle). Electrode materials were secured to insulated copper wires using conductive epoxy as described and as shown above (right). The electrode-lead connection was secured with quick weld, and the electrodes were positioned inside a PEEK fitting and C-7 epoxy was poured into the fitting. The fabrication procedure for Pt electrodes shown in Figure 3.14 used for detection of NO was similar. . . . .	52

Figure 3.4	Oxygen standard preparation. Volumes of air saturated and argon purged HBSS were drawn into a syringe to create the desired standard. Standards were pumped and chronoamperometric measurements were performed as described. RBC samples were made similarly by drawing up volumes of buffer and then a volume of RBCs to yield a 7% sample (v/v). The volume of RBCs was taken into account in the calculation of the standards, i.e., RBCs were taken to be air saturated and the required volume was accounted for in the air saturated volume of buffer. The sample was allowed to mix using inversion and rolling before pumping was started to ensure a homogenous solution of RBCs. . . . .	55
Figure 3.5	A Representative cyclic voltammagram of an air purged solution. See Figure 3.8 for cyclic voltammagrams from various oxygen standards. . . . .	56
Figure 3.6	(Left) Voltammetric detection of ferricyanide using bare Au and Ag/AgCl electrodes. The voltage was scanned at 0.1 V/s from 0.5 V to -0.1 V to obtain cyclic voltammagrams of ferricyanide standards flowing through the prototype 3D printed device similar to the device in Figure 3.2. As the ferricyanide concentration increases, the intensity of the reduction peak of ferricyanide becomes larger. Plotting the peak current against the corresponding ferricyanide standard yields a calibration curve, indicating that the electrode system functions as anticipated. (Right) Calibration curves were obtained by plotting $i_p$ of each cyclic voltammagram against the corresponding standard concentration. N = 3 electrodes. Error = STD. . . . .	59
Figure 3.7	(Left) Example of chronoamperometric perturbation signal and corresponding current response. The voltage of the working electrode is stepped from a voltage where no or minimal redox of the analyte occurs to a voltage where redox of the analyte occurs and is diffusion limited (see Figure 3.5). The corresponding current response (bottom left) begins at the same time the voltage is stepped and the response takes the form of an exponential decay. The bare Au and Ag/AgCl electrode from Figure 3.3 was used to chronoamperometrically detect ferricyanide standards flowing through a 3D printed device. (Right) Current responses to the pulsed chronoamperometric reduction of ferricyanide to ferrocyanide ( $E^\circ = 0.361$ V) are shown in the above plot. The voltage was stepped from +0.2 V to -0.3 V, and the current was measured using a commercial potentiostat. Plotting the current value at 0.3 seconds from each chronoamperogram against its corresponding concentration yields a linear calibration curve. N = 3 electrodes. Error = STD. . . . .	60

- Figure 3.8 Cyclic voltammograms of flowing oxygen standards. Oxygen standards were prepared as described and as shown in Figure 3.4 and were flowed through a prototype of the device shown in Figure 3.2. The electrode, coated with 2.5% Nafion, described in Figure 3.3 was used in the measurement. The voltage was scanned at 0.1 V/s from 0 V to -1.1 V. The resulting voltammograms from various concentrations of ferricyanide are plotted above. The reduction of oxygen occurs at around -0.4 V. Other reactions for reduction of oxygen at the electrode surface are typically performed under acidic conditions, and as the pH of buffers used in these experiments is 7.4, the bolded reaction above is likely occurring at the working electrode surface. Since the peak currents are difficult to identify, likely due to the variability in the actual oxygen reduction mechanism at the electrode surface, voltammetry was not used to calibrate the electrode for experiments with RBCs. . . . . 61
- Figure 3.9 Calibration curves generated by the chronoamperometric detection of flowing oxygen standards. Samples were prepared as described in Figure 3.4 and were flowed through the device in Figure 3.2 at 6  $\mu\text{L}/\text{min}$ . The potential was stepped from 0 V to -1 V using the Nafion coated electrode show in Figure 3.3, and the current value at various times were plotted against the concentration of oxygen in the sample. From the linear fits obtained from each curve, it can be shown that using calibration values earlier in the chronoamperometric current decay result in a more sensitive measurement (comparing the slopes in the table). However, this compromises the low background that is observed when using current values at 0.3 seconds. N = 3 electrodes. Error = STD. . . . . 62
- Figure 3.10 Calibration curves for oxygenated standards with or without RBCs. The sensitivity of the curve decreases and the background increases when RBCs are incorporated into the flowing sample: buffer only ( $y = 1.13 \times 10^{-7} + 1.26 \times 10^{-7}$ ;  $R^2 = 0.98$ ) and for buffer + RBCs ( $y = 8.15 \times 10^{-8} + 2.50 \times 10^{-7}$ ;  $R^2 = 0.93$ ). N = 1 electrode with triplicate measurement. Error = STD. . . . . 63
- Figure 3.11 Measuring hypoxic RBC samples on a 3D printed device. (A) Cross section of the device shown in Figure 3.2 details the path of the flowing sample and the fate of ATP released from RBCs. The sample can be pumped through the device, and ATP released from RBCs can diffuse across the porous, polyester membrane of the transwell inserts to be detected offline using luciferin-luciferase. The electrodes described in Figure 3.3 can be screwed into the threaded port of the device to measure the oxygen tension of the flowing sample. B) Image of the device in action. The RBCs can be seen in red flowing through the device while the set of electrodes is connected to the potentiostat from the leads with alligator clips. C) When a hypoxic sample of RBCs ( $4.76 \pm 0.53$  ppm O<sub>2</sub>) is flowed through the device, the RBCs release approximately  $2.38 \pm 0.28$  times more ATP compared to a normoxic control ( $5.66 \pm 0.6$  ppm O<sub>2</sub>). N = 3 donors. Error = S.E.M. \*p < 0.05. . . . . 64

- Figure 3.12 RBC ATP Release in Response to Decreasing Oxygen Tension. The RBC ATP release, which is directly proportional to chemiluminescence intensity, increases as oxygen tension is lowered systematically. It is important to note that the release appears to saturate at  $O_2$  tensions below about 5 ppm  $O_2$ . Relative to the normoxic control ( $7.79 \pm 0.14$  ppm  $O_2$ ), RBCs release on average  $1.70 \pm 0.43$  ( $6.74 \pm 0.31$  ppm  $O_2$ ),  $2.38 \pm 0.43$  ( $5.35 \pm 0.12$  ppm  $O_2$ ),  $2.38 \pm 0.35$  ( $2.75 \pm 0.28$  ppm  $O_2$ ),  $2.01 \pm 0.20$  ( $0.66 \pm 0.05$  ppm  $O_2$ ) fold more ATP when exposed to the corresponding oxygen tension. When 7% RBCs are incubated with 100  $\mu$ M diamide prior to reconstitution in anoxic buffer at 7%, the ATP release is significantly lower compared to other hypoxic samples,  $1.42 \pm 0.31$  ( $0.66 \pm 0.21$  ppm  $O_2$ ) (\*\*p < 0.005). N  $\geq$  3 donors and error = S.E.M. \*p < 0.05. . . . . 65
- Figure 3.13 RBC ATP Release in Response to Decreasing Oxygen Tension Plotted as a Function of Hb Saturation. The RBC ATP release, which is directly proportional to chemiluminescence intensity, increases as oxygen tension is lowered systematically. Hb saturations were calculated using the equation developed by Severinghaus, presented in Chapter 1. All Hb saturations are significantly different from the 8.74 ppm control sample (\*p < 0.001), except for the most hypoxic RBC sample and its corresponding RBC sample that was incubated with 100  $\mu$ M diamide (purple box). N  $\geq$  3 donors and error = S.E.M . . . . . 66
- Figure 3.14 3D printed device used in characterization of Pt electrodes used for NO detection.<sup>6</sup> The part file of the device details the threaded inlet/outlet and the threaded port for the electrode (left). The alignment of the electrode when tightened into the threaded port is shown in the middle panel, with the Pt working and reference electrodes serially aligned in the square shaped channel (500  $\mu$ m x 500  $\mu$ m). The electrode-device assembly is shown in the right panel with the connection to potentiostat leads and integration of capillary tubing. . . . . 68
- Figure 3.15 Detection of NO using a Pt-black electrode integrated with a 3D printed device.<sup>6</sup> Using the electrode shown above in (A) and the device shown in Figure 3.14, injections of 200 nL plugs of NO standard (190  $\mu$ M) were made, and NO was detected either using bare Pt or Pt-black coated working electrode vs. a Pt quasi-reference electrode. Average peak height (B) for NO detected with Pt-black was  $3.61 \pm 0.02$  nA relative to peak heights obtained with bare Pt ( $0.54 \pm 0.06$  nA). Repeated injections of 200 nL plugs of NO standard (190  $\mu$ M) were made over the Pt-black electrode to show the reproducibility of the system, shown in (C). N = 3. Error = STD. . . . . 69



- Figure 3.16 Pt-black modified glassy carbon detection system for measuring hypoxia-induced RBC NO.<sup>7</sup> The double layer device consists of a glassy carbon electrode embedded into a polystyrene base. The gold pillar array is fabricated using deposition methods directly onto gold wires embedded into the polystyrene base. The polymer layer consists of two microfluidic channels 400  $\mu\text{m}$  in width separated by a 50  $\mu\text{m}$  space to accommodate the gold pillars. . . 70
- Figure 3.17 NO release from hypoxic RBCs.<sup>7</sup> (Left) Amperogram overlay of signals from normoxic 7% RBCs, RBCs with inhibited NO release using L-NAME, and hypoxic RBCs. Peak areas were calculated using the peak picking software in CH Instruments. Quantity of NO detected was calculated using the peak areas from standards. (Right) NO release from 3 RBC donors (N = 3, Error = S.E.M, \* p < 0.05). . . . . 71
- Figure 3.18 NO Release from Stored RBCs Measured Using the Fluorescent Probe DAF-FM. These cells were fed once a week for up to four weeks. The data above is from an RBC sample stored for 4 weeks. Lysis was under 1% and glucose levels were maintained at around 5.5mM in the AS1N samples with feeding (data not shown). . . . . 74
- Figure 3.19 Scaling up the original O<sub>2</sub> and RBC ATP measurement device. The device shown in Figure 3.2 was printed as an array of channels as shown in panels C and D, each with detection wells for NO and ATP and threaded ports for oxygen detection. Alternative views of the original device are displayed in panels A and B. . . . . 75
- Figure 4.1 Antibiotic Resistance Timeline Based on Literature Reports.<sup>8</sup> The left had side of the timeline lists the first observations of antimicrobial resistance in various microbial species, and the date of drug introduction for widespread use is shown to the right of the timeline. Notice that with some particular antibiotic agents – specifically with penicillin, methicillin, ceftazidime, levofloxacin, linezolid, and ceftaroline – resistance is observed within two years of the drug’s introduction to general use. In the case of penicillin, the drug was in limited use prior to its widespread availability in 1943. Note that resistance to levofloxacin was observed the same year it was introduced. Pan-drug resistance (PDR) and extreme drug resistance (XDR) are terms currently appearing in medical and clinical literature that refer to a microbes resistance to all antimicrobial agents and resistance to the majority (susceptible to two or fewer) of antimicrobial agents , respectively.<sup>9</sup> Figure adapted from the CDC. 77

Figure 4.2	Example of a pharmacokinetic curve. <i>In vivo</i> dosing studies in mice are conducted to define parameters such as $C_{max}$ (the maximum concentration that a drug reaches in the plasma), AUC (thought of as total dose), and bioavailability (the ratio of concentration observed to concentration administered). <i>In vitro</i> systems like those discussed below are capable of generating these parameters on an <i>In vitro</i> platform using cultured cells. The goal of a dosing regimen is to keep the $C_{max}$ or AUC within the confines of the therapeutic window, or where the drug exhibits its maximum PD effect. MIC = minimum inhibitory concentration and MTC = maximum tolerable concentration. . . . .	78
Figure 4.3	In vitro models of dosing models. . . . .	79
Figure 4.4	The HFCR. <sup>10</sup> The HFCR is integrated with a circulation pump with multiple reservoirs for circulating fresh media and removing waste. There are various versions of the HFCR from Fiber Cell Systems, one of which is shown above holding a medium sized cartridge (top left). Other photos of the system are shown, including a closer view of the cartridge and a real cross section of the hollow fiber. A schematic of the cross section is at the top right of the figure. The cartridge contains many 200 $\mu\text{m}$ i.d. semi-permeable fibers that allow small molecules to diffuse across the wall of the fiber. This allows diffusion of drug and fresh media into the extracapillary space to reach cultured cells and diffusion of waste products into the capillaries to be pushed to waste. Photos reproduced with permission from Fiber Cell Systems. . . . .	80
Figure 4.5	3D Printed Device for Dosing Bacteria. A picture of the device is shown on the left, and a cross section of the device is shown on the right. Each of the six channels is 2 mm in width and 0.5 mm in height. The device has threaded ports (right handed 10-32) to accommodate commercial fittings and capillary tubing that allow connection to syringe pumps. Capillaries can be fitted into each inlet/outlet using the finger tight fittings. Photo repurposed with permission from Sarah Y. Lockwood. . . . .	82
Figure 4.6	Basis of PK loading and depletion profiles. The neutral colored pentagons represent a drug molecule. When concentrated drug, e.g., levofloxacin, is flowed through the channels of the device shown in Figure 4.5, a concentration gradient develops across the membrane of the well insert. The drug will diffuse with the gradient, across the membrane, and into the well until the gradient is minimized. For the case on the right, drug has been loaded into the well insert of the device for some time, and then pure buffer is flowed through the channels, reversing the gradient. This time, the drug will diffuse out of the well insert to diffuse with the concentration gradient. This is the relationship, described by Fick's laws of diffusion, governs the generation of PK profiles shown in Figure 4.9 and Figure 4.10. . . . .	83

- Figure 4.7 *E. coli* growth and purification protocol. Colonies were grown overnight by streaking frozen stock (cryostored in 50% glycerol/water) onto an agar plate with kanamycin phosphate. The next day, one colony was picked from the agar using an inoculation loop, and approximately 50 mL of LB was inoculated with the colony. This was allowed to grow for 3 hours with shaking, and the cells were subsequently purified. . . . . 86
- Figure 4.8 Flow and Non-flow studies to confirm bacteria viability in the 3D printed device. Bacteria were loaded into commercial transwell inserts on the 3D printed device and were subjected to flow of buffer for 24 hours. A non-flow comparison was performed by placing loaded inserts into culture plates loaded with buffer. Viability was probed using standard plating methods described above. From the plot above, the viability of the samples exposed to static conditions in a plate (Non-Flow,  $\text{Log}(\text{CFU/mL}) = 7.4 \pm 0.1$ ) and flow conditions (Flow,  $\text{Log}(\text{CFU/mL}) = 7.5 \pm 0.2$ ) in the 3D printed device were not significantly different relative to the purified sample of *E. coli* (Live Control,  $\text{Log}(\text{CFU/mL}) = 7.4 \pm 0.1$ ). This confirmed that the device conditions were not adversely affecting the viability of the cells, at least over the course of 24 hours.  $N = 3$  trials. Error = standard deviation. . . . . 89
- Figure 4.9 Dosing *E. coli* using a profile with a  $C_{\text{max}}$  of 25  $\mu\text{M}$ . The dose curve shown in the middle panel was measured from the well insert, and the bacterial viability was measured after dosing. The concentration of levofloxacin in the insert rises to a  $C_{\text{max}}$  of  $21.0 \pm 5.7$  in 1.5 hours. The viability of the *E. coli* after dosing, with respect to the live control ( $\text{log}(\text{CFU/mL}) = 7.4 \pm 0.1$ ), was  $\text{Log}(\text{CFU/mL}) = 4.7 \pm 1.0$ . A static dose of 25  $\mu\text{M}$  for 5 hours killed more bacteria on average ( $\text{log}(\text{CFU/mL}) = 1.0 \pm 1.1$ ) compared to the dosed sample.  $N = 3$ . Error = standard deviation.  $*p < 0.05$ . . . . . 90
- Figure 4.10 Dosing *E. coli* using a profile with a  $C_{\text{max}}$  of nearly 70  $\mu\text{M}$ . The dose curve shown in the middle panel was measured from the well insert, and the bacterial viability was measured after dosing. The concentration of levofloxacin in the insert rises to a  $C_{\text{max}}$  of  $68.0 \pm 7.1$   $\mu\text{M}$  in 1 hour. The viability of the *E. coli* after dosing, with respect to the live control ( $\text{log}(\text{CFU/mL}) = 6.9 \pm 0.6$ ), was  $\text{Log}(\text{CFU/mL}) = 0.4 \pm 0.6$ . A static dose of 70  $\mu\text{M}$  for 5 hours killed all the bacteria in the sample (no colonies to count or TFTC) compared to the dosed sample.  $N = 3$ . Error = standard deviation.  $*p < 0.05$ . . . . . 91

Figure 5.1	Dot plots of <i>E. coli</i> samples from dosing experiments. The x-axis represents the fluorescence signal from SYTO 9, a nuclear stain that is membrane permeable, which allows labeling of all bacteria. The y-axis represents the fluorescence signal from PI, which is only permeable to cells with compromised membranes. From the live control, it is clear there is a single distribution of cells, which some potentially dead or dying portion. The statically dosed samples look similar, and it is clear from their dot plots that at least 3 separate distributions of cells exist: live, dead, and viable but not culturable. For the dynamically dosed sample, it appears that VBNC and dead bacteria are present in the sample. This could explain why nearly a full kill is observed on the dynamically dosed sample in Chapter 4. . . . .	98
Figure 5.2	"Piled Higher and Deeper" by Jorge Chan. <a href="http://www.phdcomics.com">www.phdcomics.com</a> . . . . .	99

# CHAPTER 1

## INTRODUCTION

### 1.1 The Red Blood Cell

#### 1.1.1 Physical Properties

The red blood cell (RBC) is the most abundant cell in circulating whole blood, of which it comprises 40-45% by volume. Males generally have a higher hematocrit, or percent by volume of RBCs, than females. The average volume of whole blood in an adult human is approximately 5 L, with RBCs comprising up to 2.25 L of the total volume *in vivo*. White blood cells and platelets, the cells responsible for the body's immune response and blood clotting, make up < 1% of whole blood by volume, and plasma is the remaining volume (approximately 55%). The viscosity of whole blood changes in response to shear force or stress because it is a non-Newtonian fluid. In particular, whole blood is “shear-thinning”, meaning that its apparent viscosity decreases with an increase in shear stress. This is due to whole blood being a mixture of plasma and cells. Blood flow velocity varies *in vivo*, with flow rates slowing as the cells reach the microvasculature. In the microvasculature, vessel diameters are typically less than 100  $\mu\text{m}$ , and resistance to flow is high. The resistance to flow in the circulatory system is attributed to resistance in the microcirculation, which contains the smallest diameter vessels.<sup>11</sup> More importantly, the microvasculature is where oxygen transfer is the most efficient because of the large surface area exposure of vessels relative to the rest of the vasculature. Circulating hematocrit, confirmed by real-time microscopy and by modeling, varies in circulation from 45% in vessels with large diameters down to less than 10% in parts of the microcirculation.<sup>12-14</sup>

The biconcave RBC measures approximately 6-8  $\mu\text{m}$  in diameter, is approximately 92 fL in volume, and has an average life span of 120 days in the circulation.<sup>15</sup> The mature RBC is anucleated and also lacks organelles that are present in other cell types, such as mitochondria and the

Golgi body. The RBC is thus incapable of synthesizing proteins.<sup>16</sup> Hemoglobin (Hb), a tetramer protein composed of 2  $\alpha$ - and 2  $\beta$ - subunits, is > 90% of the dry mass of RBCs, making it the most abundant protein in the cell. Until the mid-1990s, it was generally assumed that the sole role of the RBC was to deliver oxygen to peripheral tissue.

### **1.1.2 Properties of the Membrane**

The structure of the RBC membrane contains 3 distinct layers: outer lipids, inner lipids with their directly associated proteins, and peripheral proteins associated with the inner leaflet of the membrane. This third component contains the membrane skeletal structure called the spectrin-actin network. This network is secured to the inner membrane leaflet through the protein ankyrin, which is associated with the protein Band 3, also known as Anion Exchanger 1 (AE1).<sup>17</sup> The network of spectrin-actin determines the deformability of the cell. The RBC must traverse the circulatory system including the microcirculation, which contains single digit micron-sized capillaries in some tissues.<sup>18</sup> The RBC must deform in order to move through the circulation, and the deformability of the RBC membrane enables the cell to pass through vessels with diameters that may be smaller than the RBC itself. The deformability of the RBC can be probed by using a St. George's blood filterometer.<sup>19</sup> This device, used in early studies on RBC deformability, consists of a flow cell with a porous membrane. The measurement is performed by flowing purified RBCs through the flow cell and through the membrane. Deformability is then directly correlated to the transit time. There are alternative methods to measure the relative deformability of RBCs, one of which was developed in the Spence lab in the 1990s.<sup>20,21</sup>

### **1.1.3 Metabolism**

The predominant way for the RBC to generate adenosine triphosphate (ATP) is by metabolizing glucose through aerobic glycolysis (10%) but mostly through anaerobic glycolysis (90%), shown in Figure 1.1, due to the absence of mitochondria and other organelles. The RBC contains glucose transporter protein 1 (GLUT1) to facilitate glucose uptake into the cell,<sup>22</sup> and individuals deficient

in GLUT1 exhibit serious neurological problems such as seizures and developmental delay.<sup>23</sup> There are other metabolic pathways utilized by the cell during glycolysis including the pentose phosphate pathway (PPP) and the 2,3-bisphosphoglycerate (2,3 – BPG) shunt, which are responsible for production of NADPH and 2,3 – BPG, an allosteric regulator of Hb. NADPH acts as a cofactor to reduce oxidized glutathione (GSSG) to its reduced form (GSH), which is a reducing agent present at approximately 2 mM in the RBC and is used as a redox buffer to protect against oxidative stress.<sup>24</sup> Intracellular ATP is present at approximately 5 mM<sup>25</sup> and is used for a variety of RBC functions, such as intracellular metabolic processes and extracellular signaling.<sup>16,26–28</sup>

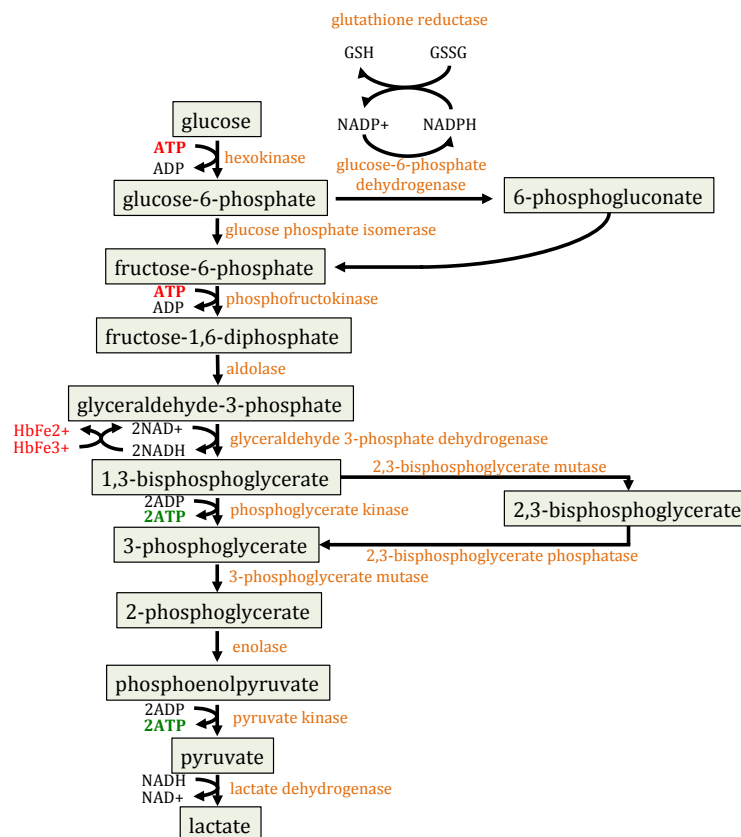


**Figure 1.1** Anaerobic glycolysis diagram. GLUT1 on the RBC membrane facilitates glucose flux into the cell. Glucose is then converted to lactate while producing a net gain of 2 ATP molecules. Glutathione cycling is also regulated by this pathway through generation of NADPH, and 2,3-BPG, an allosteric regulator of Hb, is generated as an intermediate.

## 1.2 Roles in the Circulation

It is now accepted that the role of the RBC *in vivo* is more than just a bag of Hb. However, the RBC's role in oxygen delivery to peripheral tissue is arguably its most critical role in the body. A recent example of how this role is harnessed is a case of fraud in the sport of cycling. The United States Postal Service cycling team, namely Lance Armstrong, became the focal point of an investigation by the United States Anti-Doping Agency. In the evidence presented by the agency, Armstrong's teammates described receiving transfusions of their own blood, drawn and stored one month before the date, to increase their circulating RBC count (Hct), i.e., their oxygen carrying capacity, for a race. By increasing their hematocrits, they increased their oxygen carrying capacity, giving them an edge over the competition.

### 1.2.1 The RBC as an O<sub>2</sub> Carrier

One RBC contains approximately  $3 \times 10^8$  hemoglobin (Hb) molecules, each of which can carry 4 molecules of O<sub>2</sub>, making one RBC capable of carrying  $1.2 \times 10^9$  molecules of O<sub>2</sub> if fully oxygenated. If all the RBCs released their O<sub>2</sub> at the same time into the blood stream (total volume of 5 L), this would result in an oxygen concentration of 0.2 M. This does not occur *in vivo* as it is known that the sigmoidal binding of oxygen to the RBC and its release is dictated by the partial pressure of O<sub>2</sub> in solution, an observation made by Christian Bohr in 1904.<sup>29</sup> The above values serve to highlight the high oxygen carrying capacity of the human RBC relative to what is dissolved in plasma. This carrying capacity of the RBC is required in order to meet the demands of relatively hypoxic peripheral tissue. A table of peripheral tissue oxygenation is presented below to give the reader perspective on what types of oxygen gradients occur *in vivo*.



Tissue	% Oxygen Tension	mmHg
Air	21	160
Alveoli	13	110
Arterial Blood	10-13	100
Venous Blood	5	40
Liver	5	41
Brain	4.4	34
Intestine	8	58
Muscle	4	29
Tumour	2	15

**Table 1.1** Oxygen levels in various tissues in the human body. Values were compiled from literature reports and reviews.<sup>1–4</sup>

### 1.2.1.1 Hemoglobin

The tetrameric structure of Adult Hb consists of two  $\alpha$ - and two  $\beta$ -subunits (both alpha helical in structure) held together with non-covalent linkages. Each globulin subunit contains a planar porphyrin ring with an  $\text{Fe}^{2+}$  or  $\text{Fe}^{3+}$  atom in the center. The Fe-heme assembly is stabilized by binding with a proximal histidine group as shown in Figure 1.2. A distal histidine group (not shown) also exists to modulate binding of  $\text{CO}_2$  to the  $\text{Fe}^{3+}$  atom after heme becomes deoxygenated.

In the lungs, molecular oxygen binds the iron atom only in its 2+ oxidation state, and the binding subsequently oxidizes the iron atom to its 3+ state. The heme groups release the oxygen in response to lowered oxygen tension caused by respiring tissue, and the Fe atoms remain in the 3+ charged state (methemoglobin). Methemoglobin cannot bind oxygen but does more favorably bind  $\text{CO}_2$  at its terminal amino groups in its deoxygenated state.<sup>30</sup> Hb is restored to its  $\text{Fe}^{2+}$  state primarily by NADH but also by redox systems implicated in combating oxidative stress such as glutathione.

Currently, two models exist to describe the binding between Hb and oxygen: the Monod-Wyman-Changeux (MWC) model and the Koshland-Nemethy-Filmer (KNF) model. In the KNF model, Hb exists in one conformation when it is not bound to oxygen. When oxygen binds, conformational changes in one subunit are propagated to other subunits, increasing the protein's affinity

for oxygen.<sup>31,32</sup> The MWC model proposes that Hb has two distinct states, the relaxed (R) oxygenated state and the tense (T) deoxygenated state. These two models were combined by Perutz, who first reported the crystal structure of horse Hb 1959. Perutz suggested that the two distinct states (T and R) would be in equilibrium via propagation of conformational changes between subunits.

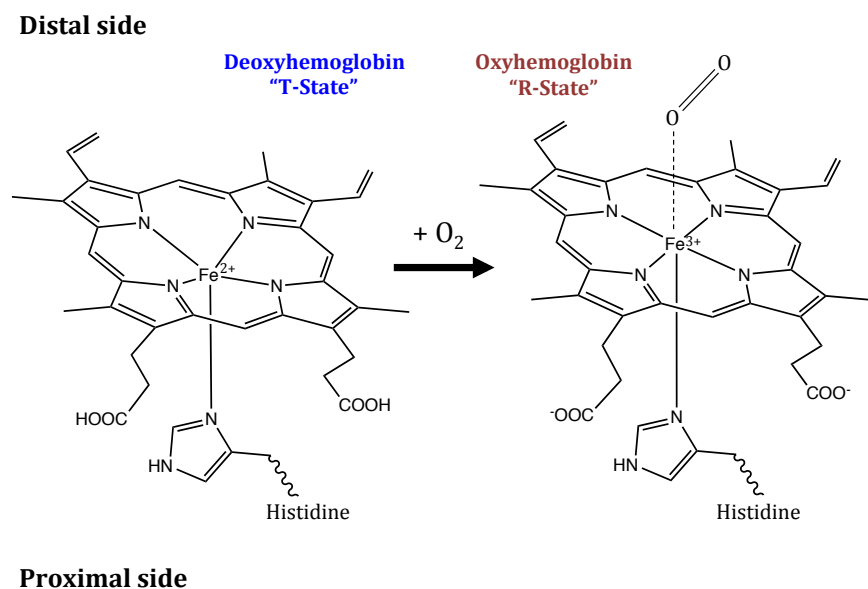


**Figure 1.2** Tense (T) and relaxed (R) states of hemoglobin. In the T state, the iron atom in the center of each heme is positioned out of the plane of the heme molecule. When oxygen binds, Fe<sup>2+</sup> oxidizes to Fe<sup>3+</sup>, and the Fe atom comes into the plane of the heme group.

When oxygen is bound to the Fe atom at the distal position, Fe<sup>2+</sup> oxidizes to Fe<sup>3+</sup>, and Hb takes on the R-state conformation, where the Fe atom is in alignment with the planar porphyrin ring. The loss of oxygen, e.g., in response to hypoxia, causes the Fe atom to move out of the heme plane, approximately 0.7 Å,<sup>33</sup> and Hb takes on the T-state conformation. This conformation change is hypothesized to physically pull on the RBC membrane to stimulate deformation induced release of RBC signaling molecules.<sup>34</sup>

The cooperative binding of oxygen to Hb, which is shown in Figure 1.3, is allosterically modulated by a number of species including 2,3-BPG, pH, and CO<sub>2</sub>, with these three species stabilizing the deoxygenated form of Hb. Decreases in pH, increases in partial pressure of CO<sub>2</sub>, and increases

in concentration of 2,3-BPG cause the binding curve to shift to the right, resulting in a higher  $P_{50}$  (called the Bohr Effect), which is the oxygen partial pressure required to half-saturate Hb with oxygen. A higher  $P_{50}$  is indicative of lower affinity for oxygen, which has been observed in disease state variants of Hb, e.g., sickle Hb (HbS). Opposite changes in pH,  $CO_2$ , and 2,3-DPG result in shifting the curve, i.e., the  $P_{50}$ , to the left, which is indicative of Hb's increased affinity for oxygen. This is observed in other variants of Hb, e.g., fetal hemoglobin (HbF), which is expressed in human fetuses and in newborns. Still today, the study of Hb allostery is an active area of research,<sup>35</sup> and binding curves are typically generated by modulating and measuring the partial pressure of oxygen in a gas tight chamber or by measuring the saturation using absorbance spectroscopy.

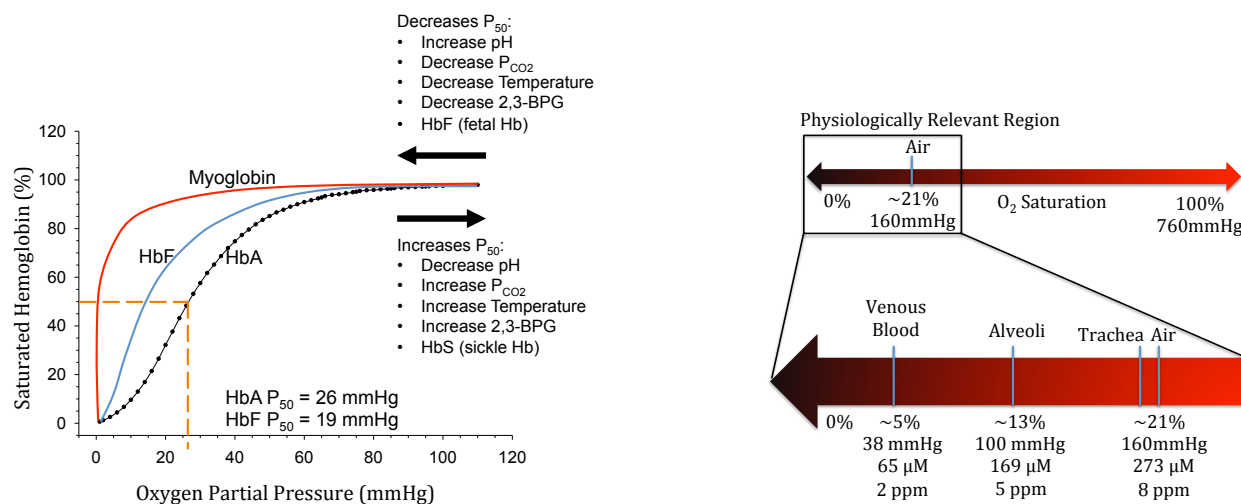


**Figure 1.3** The Hb Dissociation Curve and Relevant Oxygen Tensions *In Vivo*. The sigmoidal  $PO_2$  - Hb dissociation curve for Adult Hemoglobin (HbA) (Left) highlights the cooperative binding of  $O_2$  to HbA. The interaction is cooperative because as the oxygen tension in solution increases, Hb- $O_2$  increases non-linearly and in a sigmoidal fashion, which is a hallmark of cooperative binding. This indicates that as  $O_2$  binds to Hb, it is easier for more  $O_2$  to bind, until Hb is saturated. The relevant oxygen tensions are also displayed (Right) to set the context of the Hb- $O_2$  dissociation curve. Note that the physiologically relevant region of the curve lies between about 40 mmHg and 100 mmHg, between venous and arterial blood.

The oxygen saturation of Hb is controlled by its relationship with the partial pressure of oxygen. The mathematical relationship between  $O_2$  partial pressure and Hb saturation is sigmoidal in nature, and the empirical relationship developed in 1979 by the physiologist John Severinghaus is shown below.<sup>36</sup> This equation is an improvement over the empirical Hill equation, as it better fits

data in the lower oxygen concentration portion of the Hb curve shown in Figure 1.3. This equation is valid for the Hb-O<sub>2</sub> dissociation curve at pH 7.4 and 37°C.

$$SO_2 = \left( \frac{1}{\frac{23,400}{(PO_2^3 + 150PO_2)} + 1} \right)$$

**Figure 1.4** Empirical relationship relating partial pressure of oxygen to Hb saturation.  $SO_2$  and  $PO_2$  are Hb saturation and partial pressure of oxygen, respectively. The maximal error in Hb saturation values obtained from partial pressure measurements is 0.5%.

A plot of the partial pressure of oxygen in solution versus the Hb saturation is shown in Figure 1.3. The binding curve for HbF, shifted to the left, is also displayed in Figure 1.3. The cooperativity of both HbF and HbA is demonstrated in the sigmoidal shape of the binding curve, which is contrasted with the curve of myoglobin. Myoglobin is an oxygen binding protein present in muscle that contains a single Fe-heme moiety. The binding is non-cooperative, as is shown by the hyperbolic shaped curve shown in Figure 1.3.

Typically the oxygen partial pressure in circulating blood is 40 mmHg in venous blood and 100 mmHg in arterial blood, which corresponds to a dissolved oxygen concentration of approximately 68  $\mu$ M and 171  $\mu$ M, respectively. This physiologically relevant region of oxygen tensions are important to emulate in biological studies, as it is known that oxygen tension can have an effect on various cellular processes. However, in many biological studies, experiments are conducted using cocktails of oxygenases that render the sample anoxic (devoid of oxygen), which is not physiologically relevant, barring some tumours.

### 1.2.2 The RBC as a Regulator of pH

The RBC is an active regulator of blood pH through its carbonic anhydrase I and II (CAI or CAII) activity. CA isoform I is present in RBCs predominantly (85%) but the less prevalent form (CA II) has been shown to be more active.<sup>37</sup> CA is a metalloenzyme, containing a single zinc atom.<sup>37</sup> The

enzyme catalyzes the interconversion of  $\text{CO}_2$  and  $\text{H}_2\text{O}$  to  $\text{HCO}_3^-$  and  $\text{H}^+$ . In tissues in the body with low  $\text{O}_2$  and relatively higher  $\text{CO}_2$ , the reaction shifts to favor production of  $\text{HCO}_3^-$ . This  $\text{HCO}_3^-$  exits the cell through Band 3, which is also implicated in other RBC processes such as ATP release, in exchange for  $\text{Cl}^-$  from the plasma. This phenomenon is called the chloride shift or Hamburger shift. Curiously, humans and animal models deficient in CAI display no gross abnormalities,<sup>37</sup> but deficiencies in CA II in humans result in acidosis (lowering of blood pH), increase in bone density, and cerebral calcification.<sup>38,39</sup> Interestingly, there is evidence that CA II can bind the carboxyl terminus of Band 3, which suggests that CA may in some way be able to modulate RBC ATP release.<sup>40–42</sup> It is also known that deoxygenated Hb can bind to the intracellular domain of Band 3, suggesting that Hb can modulate charge exchange across the RBC membrane.<sup>43</sup>

### **1.2.3 Regulator of Vascular Tone**

Physiological studies from the mid-1990s recast the role of the RBC as an active participant in blood flow modulation and vessel dilation.<sup>16,20,21,26,28,44–47</sup> Two hypotheses dominate the field in terms of explaining the RBCs alternative roles in circulation. The first is that in response to a stimulus, the RBC can directly induce vessel dilation by releasing or generating quantities of the radical gas molecule nitric oxide (NO) that diffuse directly to the smooth muscle cells to dilate vessels. The second is that in response to some stimulus, the RBC releases ATP, which binds to adjacent endothelial cells to induce NO release for subsequent smooth muscle relaxation. A schematic of these two theories is shown below in Figure 1.5.

#### **1.2.3.1 The RBC as a Direct Regulator of Vascular Tone (RBC NO Induced Vessel Dilation)**

Since the identification of NO as the endothelial-derived relaxing factor (EDRF) in 1987,<sup>48</sup> for which the Nobel Prize in Physiology or Medicine was awarded in 1998, the role of NO in the hypoxic bloodstream has been debated. It has been established that the RBC has a nitric oxide synthase (NOS), and several groups including the Spence lab have measured RBC NO release, with a 7% (v/v) solution of RBCs releasing concentrations of NO on the order of single digit mi-

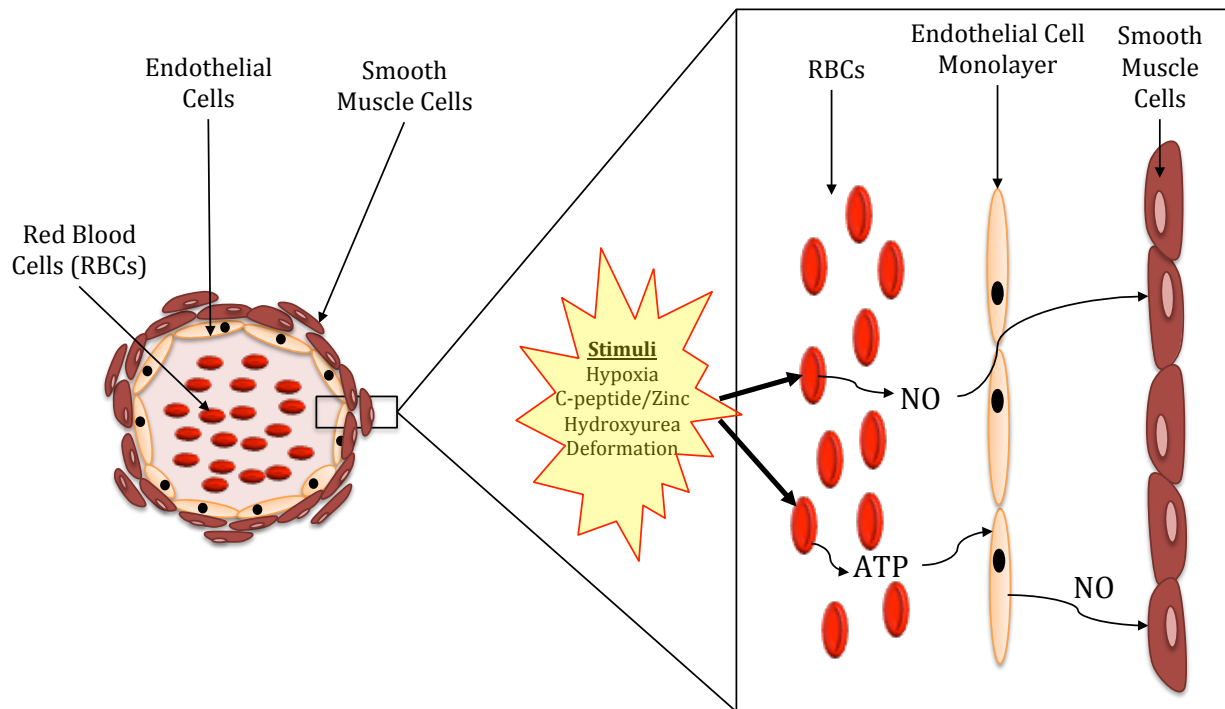


**Figure 1.5** Cross section of a resistance vessel. In response to particular stimuli, such as hypoxia, the RBC can release nM quantities of ATP. This ATP can diffuse to the endothelium and bind  $P_2Y$  receptors, increasing intracellular  $Ca^{2+}$  and activating eNOS via  $Ca^{2+}$ -calmodulin. NO is synthesized in the endothelial cells and subsequently released. The released NO diffuses to the adjacent smooth muscle cells and induces vasodilation. Alternative theories for hypoxic vasodilation suggest that NO released by RBCs in response to hypoxia diffuses through the endothelium and directly to the smooth muscle cells to induce vessel dilation.

cromolar levels.<sup>7,49</sup> However, the source of NO in the bloodstream *in vivo* is not established. There are two leading hypotheses describing the generation of NO *in vivo*. In the hypothesis proposed by Stamler, Hb carries NO through thiol linkages on cysteine groups, specifically on the  $\beta 93Cys$ , of the  $\beta$ -subunit resulting in S-nitrosylated Hb (SNO-Hb)<sup>50,51</sup> or as nitrosylated glutathione (GSH) or any other intracellular thiol. When Hb changes conformation in response to hypoxia, or lowered oxygen tension, from R-state (relaxed, oxygenated) to T-state (tense, deoxygenated), the NO moiety is released and is free to diffuse to the smooth muscle and induce vessel dilation.<sup>52</sup> There is evidence that the interaction of Band 3 protein binds to the deoxygenated form of Hb, which may provide an explanation for translocation of NO groups to and out of the RBC membrane.<sup>53</sup> It has also been shown that SNO-Hb generated NO can induce vessel dilation with control and denuded (endothelium removed) aortic rings.<sup>51,54,55</sup> However, the detectable concentrations of

SNO-Hb in the circulation have been questioned.<sup>54,56–60</sup> Though there is some evidence for the presence of this pathway *in vivo*, there is mounting evidence that this particular pathway may be a non-determinant in blood flow regulation. For example, a study of a knock-in mouse model lacking  $\beta 93\text{Cys}$  but with  $\beta 93\text{Ala}$  indicated that SNO-Hb was not a major determinant in blood flow in response to exercise (hypoxia).<sup>61</sup>

An alternative mechanism, proposed by Gladwin, puts forth that intra- and extracellular Hb functions as a nitrite reductase and can generate quantities of NO from circulating nitrite, present at approximately 500 - 1000 nM *in vivo*.<sup>62</sup> Evidence to support this hypothesis is arguably more convincing than that of Stamler's aortic ring studies, as the nitrite reductase activity of Hb is well known, having first appeared in the literature in 1981.<sup>63</sup> A gradient of nitrite between arterial and venous blood has been observed,<sup>62,64</sup> suggesting that nitrite from arterial blood is depleted in some manner in the circulation, postulated to be through the generation of NO.<sup>65</sup> Infusion of nitrite results in increased blood flow *in vivo*, a strong piece of evidence for this hypothesis, and it is known that the reductase activity of Hb is conferred to the protein in its deoxygenated state,<sup>63</sup> which suggests a coupling of NO and O<sub>2</sub> release.

Regardless of the specific mechanism, any NO generated directly in the flowing bloodstream would have to diffuse through the bloodstream, past other blood cell types such as platelets, to the endothelium. The NO would have to pass through the endothelium and bind to the adjacent smooth muscle cells to induce vasodilation, all while not reacting with oxidizing agents in the bloodstream or the endothelium. Considering the short half-life of the radical NO molecule (approximately 7 seconds in buffer and mere seconds in buffer with free Hb)<sup>66,67</sup> and its potential dependence on oxygen tension,<sup>68</sup> neither mechanism provides a convincing explanation for RBC NO-mediated vessel dilation. Another mechanism to induce vessel dilation, that of RBC-mediated ATP release, is discussed below.

### 1.2.3.2 RBC-Derived ATP as a Mediator of Vessel Dilation

As mentioned previously, RBCs store ATP in mM concentrations,<sup>28,46,69,70</sup> and it has been shown that RBCs isolated from a variety of species release ATP in response to hypoxia. It is postulated that the RBC-derived ATP binds to purinergic receptors, specifically the P<sub>2</sub>Y class of G-protein coupled receptors (GPCRs) on the endothelial cell surface.<sup>71-74</sup> This binding has been demonstrated to activate endothelial NOS (eNOS) and results in the synthesis and subsequent release of NO from the cell.<sup>71,75</sup> This hypothesis is solely for the luminal side of the blood vessel, where RBCs would be in close proximity to the endothelium as well as other blood cell types. There is another set of purinergic receptors (P<sub>2</sub>X), a ligand gated ion channel, on the smooth muscle cells surrounding the vessels. Binding of ATP to these receptors results in smooth muscle contraction<sup>74,76,77</sup> and is postulated to induce vessel constriction in response to ATP release from neural cells in close proximity to the vessel. The hypothesis implicating RBC-derived ATP as a vasodilator, for which the mechanism has been mostly elucidated, is shown below in Figure 1.6.

ATP release under a variety of stimuli has been measured. A 7% solution of RBCs from a control donor releases ATP in high nanomolar concentrations, and this release has been demonstrated to increase during hypoxia,<sup>34,69</sup> reduced pH,<sup>27</sup> physical deformation,<sup>45</sup> incubation with pharmaceutical agents,<sup>5,44,78</sup> and peptide-metal complexes.<sup>79</sup> A general mechanism of RBC ATP release has been developed, and it starts with stimulation of the RBC's G-protein coupled receptor. This recruits the heterotrimeric G protein subunits, which activates adenylyl cyclase to convert ATP to 3',5'-cyclic adenosine monophosphate (cAMP). Increase in intracellular cAMP activates protein kinase A (PKA) which phosphorylates CFTR. It has not been established through which protein ATP exits, but there are hypothesized proteins (pannexin 1). Since ATP has a net charge of 4-, its export from the cell is complemented by import of negative charge in the form of Cl<sup>-</sup> and HCO<sub>3</sub><sup>-</sup> by Band 3 and Band 4.5. Inhibition of these two proteins using sodium methanesulphonate and nitrobenzylthioinosine respectively resulted in compromised ATP release,<sup>69</sup> suggesting that these two membrane-associated proteins play an active role in the mechanism. A schematic of the signaling cascade is shown below in Figure 1.6.



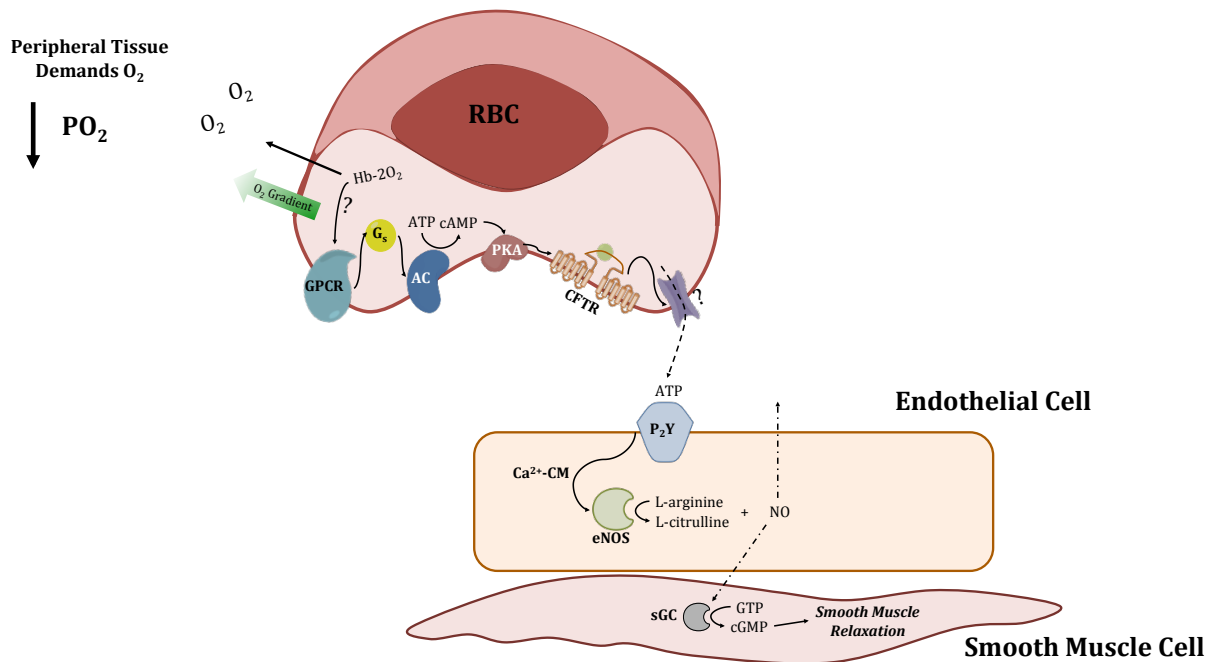


**Figure 1.6** Mechanism of hypoxic ATP release from the RBC. The signal cascade begins with activation of the G-protein coupled receptor on the surface of the RBC. How this activation occurs under hypoxic conditions is not established, but many postulate that deoxygenated Hb plays a role. Some even hypothesize that deoxygenation is a subset of deformation. The signal cascade activates the heterotrimeric G-protein subunits, which stimulate adenylyl cyclase, which induces an increase in intracellular (cAMP). Increased cAMP activates PKA which induces phosphorylation of CFTR. It is not established through which protein ATP is translocated.

## 1.3 Physiological Significance: RBC ATP Release as an Indicator of Disease

### 1.3.1 Diabetes, Cystic Fibrosis, and Multiple Sclerosis

There is mounting evidence in the literature that RBC ATP release is an indicator of some disease states. It was demonstrated by the Spence group in 2008 that RBCs isolated from type 2 diabetic donors released less ATP in response to flow deformation than did RBCs from control donors. In this same study, it was discovered that if the RBCs were incubated with nM quantities of metal-activated C-peptide, a byproduct of insulin secretion *in vivo*, the ATP release from the diabetic RBCs was statistically equivalent to control donors with no C-peptide added.<sup>79</sup> It has been established that CFTR is required for ATP release from the RBC,<sup>45</sup> and it was observed that RBCs from donors with cystic fibrosis do not release ATP in response to deformation.<sup>80</sup> It has been observed

by the Spence lab that a solution of 7% RBCs from donors with multiple sclerosis (MS) release on average 2 times more ATP than control donors.<sup>81</sup>

### 1.3.2 Motivations

It has been established that hydroxyurea, the only FDA-approved drug for the treatment of symptoms associated with sickle cell disease (SCD), increases deformation-induced ATP release from control rabbit RBCs.<sup>78</sup> This increase in ATP release is coupled with an increase in intracellular calcium, and evidence suggested that nitrosylated hemoglobin was also observed. The hypotheses generated from these studies suggest that HU may act in a two-pronged fashion to alleviate symptoms of SCD by improving vascular tone and by combating sickling of the sickle cell RBC.

An extension of these studies is discussed in the next chapter, using RBCs from consenting human donors. In Chapter 2, it is demonstrated that hydroxyurea increases deformation-induced ATP release from human RBCs. It is further shown that the fate of this ATP includes diffusion to an adjacent cultured endothelium to induce NO production and release. Further studies with this system required the development of deoxygenation methods and oxygen detection methods in order to correlate ATP release with oxygen tension in an RBC sample in preparation for anticipated RBCs from sickle-cell donors. Though the sickle-cell donor blood was not available, the correlation is demonstrated in Chapter 3 by using blood from healthy donors and a 3D printed fluidic device with integrated detection wells and integrated oxygen electrodes as the platform. The physiological implications for the ATP measurements in Chapter 3 are significant, as they indicate that ATP release correlates with Hb saturation (heme conformation). Inhibition of ATP release using the cell stiffening agent diamide provides support for the hypothesis that hypoxia is a form of deformation.

Chapter 4 is a departure from RBC studies. A device was developed in the Spence lab in order to mimic *in vivo* dosing profiles observed in traditional pharmacokinetic studies. In Chapter 4, the device is used to dynamically dose a sample of *Escherichia coli*, and it is observed that a higher kill rate correlates with maximum observed concentration in the dose profile. The implications of

this device are significant in that a new *in vitro* platform was developed to mimic *in vivo* dosing profiles of the antibiotic levofloxacin. These dosing profiles were demonstrated to correlate with decreases in *E. coli* viability.

## CHAPTER 2

### MONITORING RBC-ENDOTHELIAL CELL SIGNALING IN A MICROFLUIDIC DEVICE: IMPLICATIONS FOR THE TREATMENT OF SICKLE CELL DISEASE

#### 2.1 Hydroxyurea Use in the Treatment of Sickle Cell Disease

Sickle cell disease (SCD) encompasses a group of autosomal, recessive disorders caused by mutations in adult hemoglobin (HbA), specifically resulting from mutations in the  $\beta$ -globin subunit.<sup>82</sup> The most common form of the disease is sickle-cell anemia, which is characterized by the presence of a point mutation in the  $\beta$ -globin subunit, specifically the replacement of a glutamic acid residue with a valine residue.<sup>83</sup> This type of Hb is termed sickle hemoglobin (HbS), and its electrophoretic mobility was observed to be different compared to HbA's mobility by Linus Pauling and colleagues in 1949.<sup>84</sup> The resulting mutation imparts a more hydrophobic nature to a pocket of the protein that enables HbS to polymerize as the cell becomes deoxygenated.<sup>85,86</sup> This results in bulk crystallization that deforms the cell into the recognizable sickle or crescent shape that was first observed in a dental student by a Chicago doctor in 1921.<sup>87,88</sup> There are other mutations in the  $\beta$ -globin subunit that result in different forms of the disease, which vary in intensity, such as  $\beta$ -thalassaemia.<sup>83</sup> Sickle cell anemia is characterized by chronic anemia and vaso-occlusive crises, where sickled RBCs obstruct blood flow and consequently, the oxygen supply to various parts of the body. While RBCs from healthy individuals have an average lifespan of 120 days,<sup>15</sup> a sickled RBC's lifespan is about 20-30 days.<sup>89,90</sup> This rapid turnover of RBCs can affect the spleen (splenic sequestration crisis) and renders the patient chronically anemic since the bone marrow cannot replenish RBCs at the rate at which RBCs are removed from the circulation.

Typically the disease is managed by treating patients with antibiotics and pain relievers for infections and crises. Blood transfusions aid in the removal of sickled cells, and supplemental oxygen is recommended. For patients whose disease cannot be managed with the strategies listed above, a more invasive bone marrow transplant may be recommended.<sup>91</sup> HU treatment typically begins

with 10-15 mg/kg per day with incremental 5 mg/kg increases every 6-8 weeks until the maximum stable dose is reached.<sup>92</sup> There is no standard way to optimize dosing based on a physiological response, such as an individual's RBC response. However, responses to treatment with HU include increase in fetal hemoglobin (HbF) levels, reduction in frequency of crises, and reduced need for transfusions.<sup>93</sup> Although the impact of long-term hydroxyurea treatment on patient mortality is debated,<sup>94,95</sup> it is desirable to begin treatment with HU in a patient's adolescence or childhood years to stifle the development of chronic complications and organ damage.<sup>96</sup>

### **2.1.1 Hypothesized Mechanisms of Action of Hydroxyurea**

HU is an established ribonucleotide reductase (RNR) inhibitor,<sup>97-99</sup> and the drug has been shown to have other therapeutic properties, namely anti-cancer.<sup>100,101</sup> By inhibiting RNR, HU functions to inhibit the synthesis of deoxyribonucleotides, precursors to DNA synthesis, from ribonucleotides. HU has been demonstrated to increase the expression of HbF in patients with sickle cell disease<sup>102-106</sup> as well as increase the polymerization lag time of HbS,<sup>106-108</sup> which is the time elapsed prior to formation of Hb polymers. The polymerization lag time is reported to be sensitive to relative concentration of HbF to HbS and to RBC hydration status. The benefit to the patient of the observed increase in HbF is rationalized by HbF's higher oxygen affinity relative to HbS and by a dilution effect. The relative increase in HbF levels effectively dilutes the HbS, making the initial nucleation step more difficult,<sup>109</sup> i.e., the RBC is less likely to sickle.<sup>110,111</sup> Although the observed increase in total HbF is approximately 10-30 %, the effect is only observed 4-24 weeks after a patient begins treatment with HU.<sup>94,96</sup> A more recent analysis based on clinical reports of the HbF/HbS ratio in patients after beginning treatment with HU refutes the validity of previous measurements.<sup>112</sup> Regardless, this increase in a patient's HbF levels would be a long-term effect of HU treatment and does not explain the clinically observed, immediate beneficial effects that HU has on a patient, e.g., less hemolysis, fewer sickled RBCs, and improved vascular tone and blood flow.<sup>83,93,96</sup>

### 2.1.2 Effect of Hydroxyurea on RBCs

Observations of how HU impacts RBC deformability, which is directly related to an RBC's ability to release ATP, vary greatly in the literature, with some observing that HU stiffens RBCs<sup>113</sup> or that HU renders RBCs more deformable.<sup>114</sup> The conflicting data can be explained by previous observations from the Spence group and by a numerical analysis of concentrations of HU used in other studies. A simple calculation of moles of HU per RBC in each study using reported parameters (concentration of HU, sample volumes, hematocrit) from the respective studies and also assumptions (hematocrit for healthy versus sickle cell patient), allows comparison of each study and rationalization of observations reported.

Study	Study Type	Deformability	HU	Hct (%)	femtomole HU/RBC
Ballas	in vivo	increase	1000 mg/day	30	0.8
Huang	in vitro	decrease	0.5-50 g/L	24	2.5-252
Spence*	in vitro	increase/decrease	100 $\mu$ M	7	0.1

**Table 2.1** Comparison of parameters from studies on deformability of RBCs exposed to HU. Using the parameters listed and other known values including volume of blood in the human body (5 L), volume of an RBC (92 fL), and molar mass of HU (76.05 g/L), the moles of HU per RBC was calculated for each study. \*This study directly measures ATP release from the RBC, which is an indirect measurement of RBC deformability.

Compared to the observed HU/RBC ratio that yields maximum ATP release from the RBC in the Spence lab (incubation of 7% RBCs with approximately 100  $\mu$ M), it is clear that Huang et al. used at least an order of magnitude more HU per RBC than the two other studies. This could explain why a decrease in RBC deformability was observed and why others have reported increases in RBC deformability. Based on these calculations, observations from previous Spence lab studies<sup>78</sup> and Figure 2.9, it is likely that the study from Huang et al. used high concentrations of HU that have been observed to decrease or not affect RBC deformability.

A previous study from the Spence group demonstrated that RBCs from rabbits released approximately 2-fold more ATP relative to controls when incubated with 0.25 nM of the NO donor spermine NONOate (0.5  $\mu$ M NO) or with 100  $\mu$ M HU.<sup>78</sup> When cells were incubated with varying concentrations of HU (0-200  $\mu$ M, increments of 25  $\mu$ M) or with NO donor (0-1  $\mu$ M, increments

of approximately 100 nM), the magnitude of ATP released from the rabbit RBCs decreased. That is, some concentration of HU or NO donor, 100  $\mu$ M and 0.25  $\mu$ M respectively, corresponded with a maximum ATP release from the rabbit RBCs. Interestingly, when rabbit RBCs were incubated with the NOS inhibitor L-NAME prior to incubation with HU, the observed ATP release decreased, suggesting that RBC NOS and NO are involved in the ATP release mechanism.

In order to investigate the role of RBC NO in this mechanism and if RBCs incubated with HU could elicit endothelial release of NO, a microfluidic device was utilized to facilitate experiments to probe cell-to-cell interactions. The traditional soft polymer device allowed culture of an endothelial cell line in detection wells, which were fabricated above a micron-sized channel through which purified RBCs could be flowed.

### **2.1.3 Multilayer Fluidic Devices to Monitor Cell-to-Cell Communication**

Microfluidics has proven to be an optimal tool for studying cell-to-cell communication. The technology is flexible in its ability to conform to a range of geometric requirements, and the micron scale of the technology is well suited for cellular study because of its biological relevance, i.e., spatial proximity of cells can be well controlled and distances for diffusion of small molecules are biologically relevant. The flexibility of this platform has been demonstrated in multiple disciplines for various purposes including single cell analysis,<sup>115,116</sup> study of cell-cell junctions,<sup>117</sup> scaffolds for multiple cell types,<sup>118,119</sup> stem cell – microenvironment communication,<sup>120</sup> and cell-cell signaling of small molecules and proteins.<sup>121</sup>

The microfluidic device used in the experiments described in this chapter enables measurement of releaseates of RBCs and of cultured endothelial cells while incorporating not only flow but both cell types onto one platform. The endothelial cells are cultured in a detection well and are in physiologically relevant proximity (microns) to a stream of flowing RBCs, which are separated from the well by a porous polycarbonate membrane. The membrane allows small molecules to diffuse between the channel and detection well. The channels in the device shown in Figure 2.4 approximate resistance vessels (approximately 100  $\mu$ m), and capillary inner diameters were chosen

to ensure shear stress on the RBCs flowing from syringe to microfluidic device, specifically to mimic *in vivo* conditions where shear stress can range from 3 to 120 dynes/cm<sup>2</sup>.<sup>122</sup> Shear stress is the force an RBC is subjected to under flow conditions and is proportional to the fluid velocity and inversely proportional to the diameter of the vessel or tubing.<sup>123</sup>

#### **2.1.4 Probing the HU-RBC Interaction by Measuring HU Uptake**

Because the increase in HbF in sickle cell anemia patients taking HU is only observed 1-6 months after a patient begins treatment with the drug,<sup>94,96</sup> a molecular level explanation of the drug's more immediate effects on a patient is needed and might provide evidence to further support the role of the RBC as a direct modulator of blood flow. It has been documented by previous studies that HU exerts effects on rabbit RBC ATP release capability in 30 minutes, suggesting that HU interacts directly with the RBC to alter some property related to ATP release, e.g., deformability. To this end, the interaction between HU and the RBC can be investigated by measuring the uptake of the drug into or on the cell. As it is unknown what the actual mechanism of the drug's interaction with the RBC is, the term "uptake" will be used to describe the interaction. There are reports in the literature suggesting that the RBC membrane composition is altered between sickle cell anemia patients taking HU and patients not taking the drug<sup>108,124</sup> and that HU can be processed in various ways by RBC metabolism.<sup>125,126</sup> There are also reports that HU functions as a carbonic anhydrase (CA) inhibitor.<sup>127</sup> The particular zinc metalloenzyme is present in the human RBC as CA I and II isoforms and is responsible for regulating blood pH levels through the reversible reaction ( $\text{H}_2\text{O} + \text{CO}_2 \rightleftharpoons \text{H}^+ + \text{HCO}_3^-$ ) with carbon dioxide. Reports also suggest that CA interacts with the membrane associated Band 3 protein, which is implicated in the mechanism of ATP release in the RBC as described in Chapter 1. To this end, observation of an interaction of HU with the RBC, if it is one involving binding or uptake, would provide evidence for molecular level effects on the RBC ATP release system.



### **2.1.5 Motivations**

The goal of this chapter is two fold: (1) to confirm that deformation-induced ATP release from HU-incubated *human* RBCs increases relative to controls and (2) to demonstrate that one fate of the increased RBC-derived ATP is stimulation of endothelial NO, which would implicate RBC-derived ATP as a vessel dilator. These aims are accomplished with the device described below. The development of uptake experiments to probe HU's interaction with the RBC are also presented, and future experiments are suggested.

## **2.2 Methods**

### **2.2.1 Collection and Purification of RBCs**

Blood was obtained using procedures approved by the Biomedical, Health Sciences Institutional Review Board (BIRB) at Michigan State University. As depicted in Figure 2.1, human whole blood was collected via venipuncture from consenting donors into lithium heparin-coated Vacutainer tubes (10 mL total volume; BD Biosciences, San Jose, CA) to prevent coagulation. Whole blood was centrifuged at  $500 \times g$  at  $25^{\circ}\text{C}$  for 10 minutes. Supernatant and buffy coat were removed via aspiration, and RBCs were resuspended in PSS (1.2 mM magnesium sulfate, 2.0 mM calcium chloride, 4.7 mM potassium chloride, 5.6 mM glucose, 21.0 mM tris (hydroxymethyl) aminomethane, 140.5 mM sodium chloride in 5% bovine serum albumin, adjusted to pH 7.4). This spin-down procedure with aspiration was repeated twice more, resulting in a total of 3 washes with PSS. After the third wash, the hematocrit of the resulting packed RBCs was determined using a micro-hematocrit centrifuge (Iris Sample Processing, Inc., Westwood, MA).

### **2.2.2 Endothelial Cell Culture**

Bovine pulmonary artery endothelial cells (bPAECs) were cultured in T-25 tissue culture flasks (TPP, MIDSCI, St. Louis, MO) with approximately 15 mL of endothelial growth media (EGM,

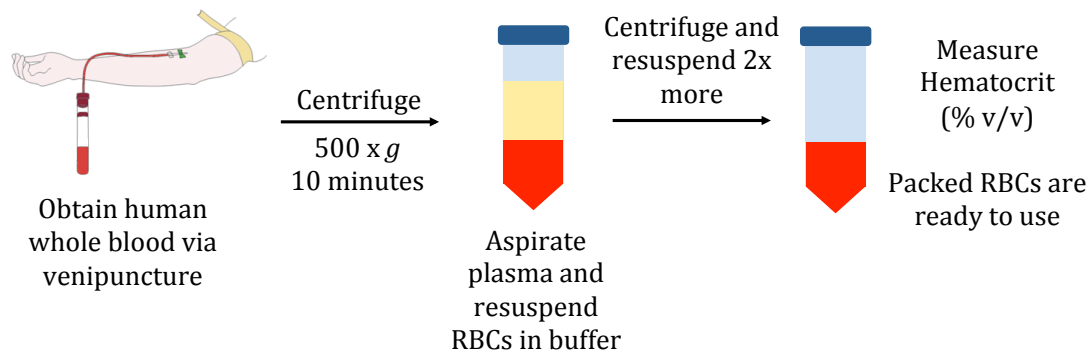


**Figure 2.1** Whole blood collection and RBC purification procedure. Whole blood is obtained via venipuncture from consenting, informed donors. The whole blood is centrifuged and plasma is aspirated from the tube as described. The packed RBCs are then transferred to a secondary tube with PSS or the appropriate buffer. The RBCs are centrifuged and aspirated twice more for a total of three washes with PSS. Once washed, packed RBCs are obtained, the hematocrit is measured, and the purified RBCs are ready for use.

Caisson Laboratories Inc., North Logan, UT). The EGM was prepared as a low glucose medium (5.5 mM glucose) with Dulbecco's Modified Eagles Medium with 2.5% v/v adult bovine serum, 7.5% fetal bovine serum, penicillin, streptomycin, and amphotericin B (MIDSCI). Cell flasks were stored in a 37°C incubator with 5% CO<sub>2</sub>. The EGM was changed every 3 days, and when cells reached confluence, they were subcultured. To subculture, EGM was aspirated from the existing culture, and the confluent cells were washed with HEPES (4-(2-hydroxyethyl)-1-piperazineethane sulfonic acid, MIDSCI). The HEPES was subsequently aspirated, and an aliquot of 0.25% trypsin (4 mL) was added to the flask and was allowed to sit for 2 minutes at 37°C and 5% CO<sub>2</sub>. Trypsin was aspirated from the flask, and cells were detached physically by tapping the base of the flask and by rinsing confluent cells with warm EGM. This cell suspension was distributed to other flasks in the case of subculturing, or the cell suspension was centrifuged and resuspended if adjustment to cell density was needed for culturing on microfluidic devices. To culture cells onto the microfluidic device, an aliquot of fibronectin (100 µM) was added to each well of the device and was allowed to evaporate under UV irradiation for 15 minutes. A 10 µL aliquot of bPAECs in suspension was added to the wells, and the device was incubated at 37°C. EGM was changed every 2 hours until confluent cells were observed using an upright microscope (Olympus MVX10) with a FITC cube to enable visualization of the nuclear stain Hoechst 33342 (excitation: 346 nm/emission: 497 nm).

### 2.2.3 Preparation of RBC ATP Release Agonists, Antagonists, and Reagents

The HU (Sigma) stock solution was prepared as 2 mM in PSS. To prepare RBC samples with HU, an aliquot of 2 mM HU stock was added to buffer to make a 100  $\mu$ M solution. After inverting the solution several times, an aliquot of RBCs could be added to the solution and incubated for 30 minutes. The 7% RBC control samples were prepared by adding an aliquot of packed RBCs to PSS to yield a sample with an RBC volume of 7%.

Ca<sup>2+</sup> free PSS (12 mM magnesium sulfate, 4.7 mM potassium chloride, 5.6 mM glucose, 21.0 mM tris(hydroxymethyl) aminomethane, 140.5 mM sodium chloride with 5% bovine serum albumin and adjusted to pH 7.4) was used to inhibit bPAEC NO and RBC ATP release. For these 7% RBC solutions, samples were prepared as described above but with Ca<sup>2+</sup> free PSS.

Glybenclamide (GLY) stock solution was prepared as previously reported.<sup>45,78</sup> For these experiments, a 5 mM stock solution was prepared by dissolving GLY in a solution containing 20% 0.01 M sodium hydroxide and 80% dextrose (v/v). To prepare RBC samples incubated with GLY, an aliquot of GLY stock was added to buffer to make a 100  $\mu$ M solution. After mixing, an aliquot of RBCs was added, and the sample was allowed to incubate at room temperature for 30 minutes.

A 5 mM L-N<sup>G</sup>-nitroarginine methyl ester (L-NAME, Cayman Chemical Company, Ann Arbor, MI) stock solution was prepared by dissolving L-NAME in DDW. An aliquot of L-NAME stock was added to PSS and mixed, prior to addition of packed RBCs, to yield a 100  $\mu$ M solution. The 7% RBC samples made with L-NAME were allowed to incubate for 1 hour.

Diamide stock solution (1 mM) was prepared by adding diamide (Sigma Aldrich) to DDW. An aliquot of 1 mM stock was added to PSS and mixed, prior to addition of packed RBCs, to yield a 100  $\mu$ M solution. The 7% RBC samples made with diamide were allowed to incubate for 30 minutes.

### 2.2.4 Preparation of Extracellular NO Probe DAF-FM and Reagents

DAF-FM (4-amino-5-methylamino - 2',7' - difluorescein, 7 mM in DMSO, Sigma), was stored frozen as 7  $\mu$ L aliquots until the day of each experiment. A 10  $\mu$ M working solution of DAF-FM

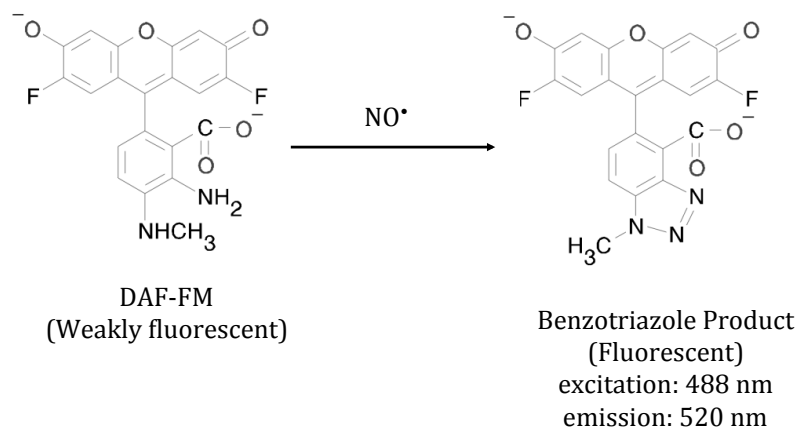


**Figure 2.2** Reaction of NO with extracellular probe DAF-FM.

was prepared by adding an aliquot of thawed 7 mM stock to the buffer HBSS (Hank's Balanced Salt Solution: 1.2 mM anhydrous calcium chloride, 0.5 mM magnesium chloride, 0.4 mM magnesium sulfate, 5.2 mM potassium chloride, 0.4 mM potassium phosphate monobasic, 4.2 mM sodium bicarbonate, 138 mM sodium chloride, 0.3 mM sodium phosphate dibasic, 5.5 mM D-glucose, Sigma). When bPAECs were confluent in the device and ready for experiment, 10  $\mu\text{L}$  of 10  $\mu\text{M}$  DAF-FM was pipetted into the wells.

Cultured bPAECs and RBCs were incubated for 1 hour with L-NAME prior to each experiment to inhibit NO release from each cell type. L-NAME was prepared as a 3 mM working solution in HBSS for studies to measure bPAEC NO release. Cultured bPAECs were incubated with PPADS (pyridoxal phosphate 6-azo (benzene-2', 4'-disulfonic acid, Sigma Aldrich) to block RBC-derived ATP from binding to endothelial  $\text{P}_2\text{Y}$  receptors. PPADS was prepared by diluting a 100  $\mu\text{M}$  stock solution with HBSS to yield a 10  $\mu\text{M}$  working solution. Endothelial cells were incubated with 10  $\mu\text{L}$  of 10  $\mu\text{M}$  PPADS prior to the experiment.

### 2.2.5 Fabrication of Microfluidic Devices

The protocol for rapid fabrication of microfluidic devices was pioneered by the Whitesides group in the 90s.<sup>128,129</sup> To fabricate the silicon master, a layer of SU-8 50 negative photoresist (MicroChem

Corp., Newton, MA) was spin coated (Laurell Technologies, North Wales, PA) onto a 4" wafer (University Wafer, South Boston, MA) using the following program: 500 rpm for 15 seconds, 1000 rpm for 30 seconds. After spin coating, the wafer and SU-8 layer were pre-baked at 95°C for 5 minutes. Then, a transparency mask created using a commercial printer (HP Laserjet 1300) was positioned over the wafer, and the assembly was placed under a UV flood source with timing controllers (Newport). The wafer-mask assembly was exposed to the UV flood source, and after UV exposure, the mask was removed, and the wafer was post-baked at 95°C for 5 minutes to hasten crosslinking of the photoresist. The master was immersed in 2-methoxy-1-methylethyl acetate (Sigma Aldrich, St. Louis, MO), and by agitating the solution-wafer assembly, the uncured SU-8 was dissolved off the wafer. Features were inspected visually using an upright microscope (Olympus MVX10) to confirm the effectiveness of the fabrication procedure, which is detailed in Figure 2.3.

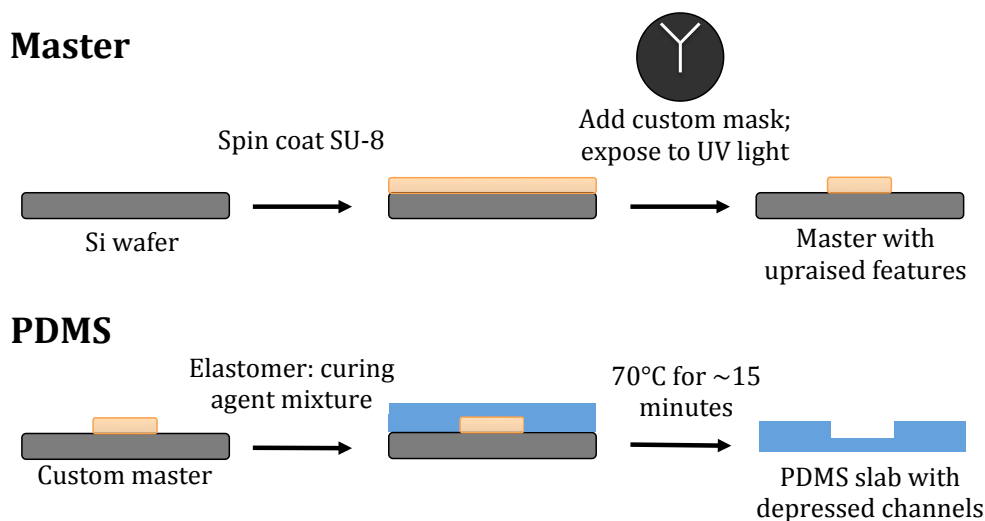


**Figure 2.3** Photolithographic fabrication of the silicon master and soft lithographic fabrication of polymer microfluidic devices. Masters were fabricated by spin coating photoresist as described. The completed polymer device for experiments was assembled by placing strips of polycarbonate membrane (0.4  $\mu\text{m}$  i.d.) over channels after which a blank PDMS slab with punched detection wells was placed on the top. The assembled device was baked for 10 minutes to establish a reversible seal.

Using the master described above and a blank master, PDMS devices were fabricated by pouring a degassed 20:1 mixture of Sylgard 184:curing agent (Ellsworth Adhesives, Germantown, WI)

over the features and over the center of the blank and then baking both at 70°C for 15 minutes. After baking, a 5:1 degassed mixture of polymer and curing agent was poured over the master and blank with subsequent baking again at 70°C for 15 minutes. Using 20:1 over the features and the center of the blank ensured that the seal between the blank and master was stronger where necessary, i.e., to prevent leaking of sample from the channels of the device. PDMS layer removal was aided by using a scalpel. After removal of the polymer layer from the master, a 20-gauge luer stub adapter (BD) was used to bore inlets into the channels. Detection wells were created in the blank slab of PDMS by using a 1/8" die (General) to punch wells into the slab using a 96-well plate template as a guide. Polycarbonate membranes (0.4  $\mu\text{m}$  pore diameter, Steriltech Inc., Kent, WA) were laid over the channels, feature side up, after which the PDMS slab with detection wells was positioned on top to yield the sandwich-like device shown in Figure 2.4.

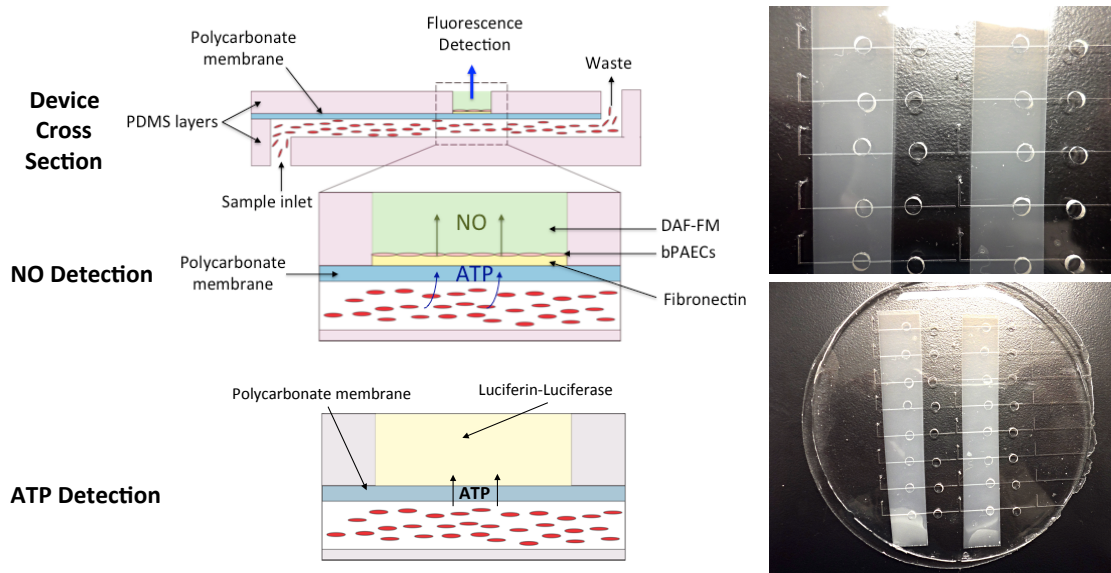


**Figure 2.4** Cross section of the microfluidic device adapted from Lockwood et al. The top panel displays the cross section of the whole microfluidic device. RBCs are flowed through a channel and are separated from the detection well by a porous, polycarbonate membrane (0.4  $\mu\text{m}$  i.d.). ATP that is released from the RBCs can diffuse across the membrane and can interact with cultured endothelial cells (Top). If DAF-FM is loaded into the wells with a cultured endothelium, bPAEC-derived NO can be measured (Middle). When the endothelium is not cultured in the detection well, RBC-derived ATP can be directly measured using LL (Bottom).

The assembled device was then cured at 70°C for 20 minutes to ensure reversible sealing. The end device had channels approximately 200  $\mu\text{m}$  in width and 100  $\mu\text{m}$  in height. The assembled

device was approximately 4" in diameter.

## 2.2.6 Chemiluminescence Assay to Measure ATP Release

ATP release from RBCs was measured by mixing samples with a solution of the enzyme luciferase with added D-luciferin. When ATP reacts with luciferase, light is emitted and can be measured. The chemiluminescence reaction is shown in Figure 2.5. The luciferin-luciferase (LL) mixture was prepared by dissolving 2 mg of D-luciferin (GoldBio, St. Louis, MO) in 5 mL of DDW. This mixture was then poured into a vial of firefly tail extract (Sigma) and shaken until solids were dissolved. The stock LL was aliquoted and frozen until the day of each experiment.

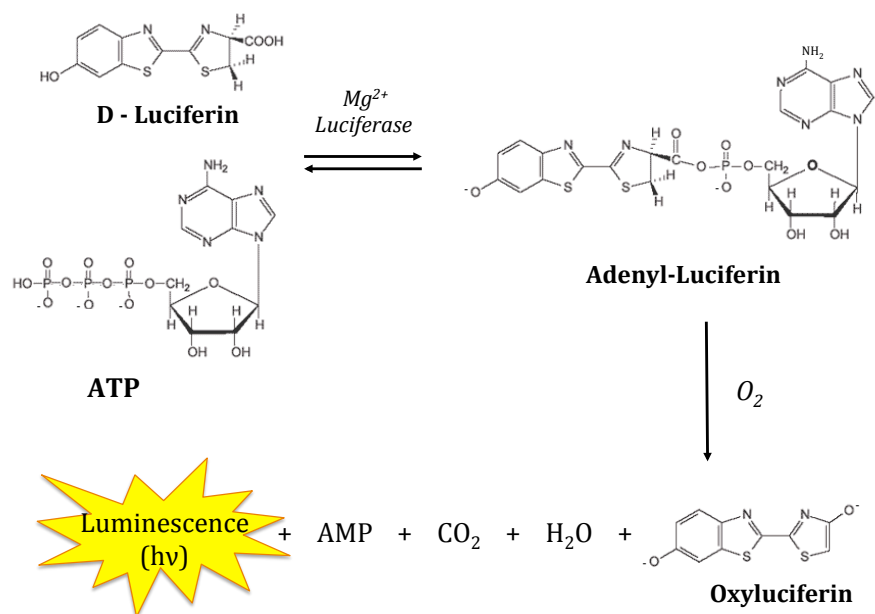


**Figure 2.5** Chemiluminescence reaction of ATP with D-luciferin. The reaction requires the enzyme luciferase,  $Mg^{2+}$ , and oxygen to go to completion. The luminescence signal can be collected with a photomultiplier tube in homemade systems or with commercial instrumentation such as a plate reader.

After RBC samples were prepared, they were loaded into 500  $\mu$ L syringes (Hamilton Company, Reno, NV) and secured to a syringe pump (Harvard Apparatus, Holliston, MA). Wells of the microfluidic device were loaded with 10  $\mu$ L of the luciferin-luciferase mixture, and the samples were flowed at 6  $\mu$ L/min from the syringes through the device for 30 minutes using 50  $\mu$ m i.d. silica

microbore capillaries (Polymicro Technologies, Phoenix, AZ). After 30 minutes, flow was stopped, and the device was taken to the plate reader (Spectramax M4, Molecular Devices, Sunnyvale, CA) for measurement. The device was placed in the plate holder, and a 96-well plate guide was placed over the wells. For non-flow studies, equal volumes of luciferin-luciferase and sample were added to wells of a 96 well plate, and the light emission was measured using the plate reader. The experimental setup is detailed in Figure 2.6.

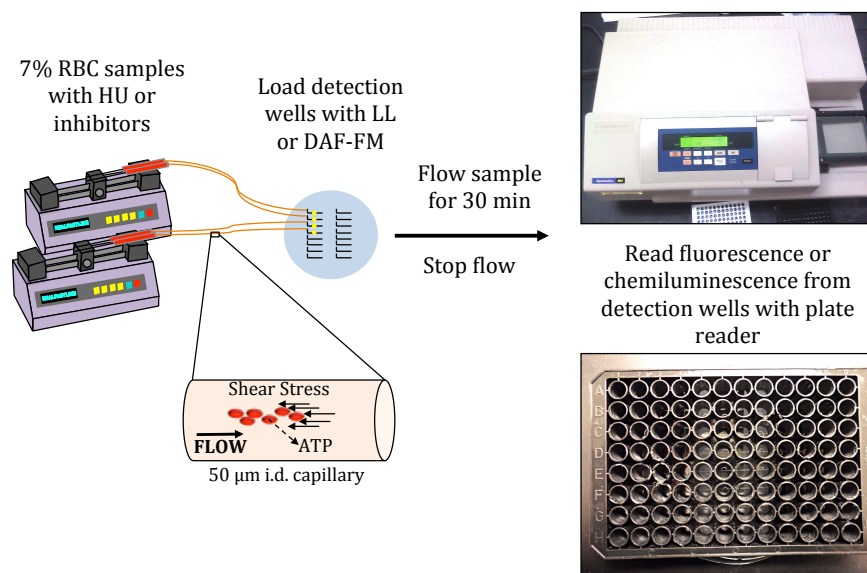


**Figure 2.6** Experimental setup for flowing RBCs on the device in Figures 2.4. RBC samples were prepared offline as described and were loaded into 500  $\mu$ L syringes. After loading detection wells with the appropriate detection reagent (LL for ATP only or later DAF-FM for bPAEC NO only), syringes were loaded onto a syringe pump, and samples were flowed for 30 minutes. After the allotted time, the device was removed from the pump and taken to the plate reader for detection.

ATP data for Figure 2.9 was taken with the in-house developed system<sup>47</sup> shown in Figure 2.7, and methods were performed in a similar fashion to that described above. LL and samples were loaded into syringes and were pumped through 50  $\mu$ m i.d. microbore capillary tubing to a T-junction where the two sample streams mixed. The mixed sample was then passed through a 100  $\mu$ m i.d. capillary over a photomultiplier tube to collect light emitted from the reaction as shown. Data was collected in triplicate for each sample as the average signal over 100 seconds using a Labview program.



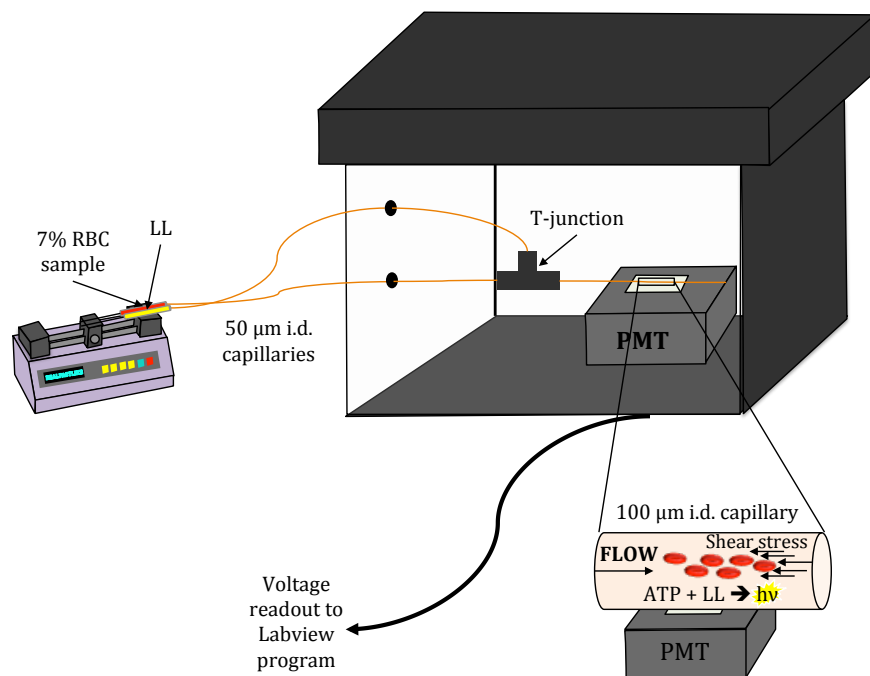


**Figure 2.7** In-house system for measuring ATP release from RBCs. Samples and LL mixture were prepared as described and were loaded into 500 µL syringes. Syringes were loaded onto a syringe pump and samples were pumped at 6 µL/min through the capillary system. Sample and LL mix at the T-junction, and the reaction between ATP and the LL reagent occurs. The mixed sample flows a fixed distance to a PMT, where light from the reaction can be detected. Data is displayed and saved using a Labview program. Image is not to scale.

### 2.2.7 Fluorescence Measurement of NO Release from a Cultured Endothelium

When bPAECs were confluent in the wells of the microfluidic device, EGM was removed, and if applicable, aliquots of inhibitors of bPAEC NO release were added to wells, and cells were allowed to incubate for the allotted time. After the incubation period, inhibitor solutions were removed using a Kimwipe, and 10 µL of 10 µM DAF-FM was added to each well. Then, sample flow was started. After 30 minutes of sample flow, pumps were turned off, and the device was taken to the plate reader for fluorescence measurement (excitation: 488 nm/emission: 520 nm).

### 2.2.8 HU-Incubated RBC Preparation for GC-MS Analysis

HU standards (0 – 100 µM) were prepared in PSS, and RBC samples incubated with HU were prepared as described and incubated for the allotted time. After incubation, cells were spun at

500  $\times$  g for 10 minutes and the supernatant was removed. Naphthalene (0.5 ppm) was added as an internal standard. Supernatant and standards were extracted in a 1:1 ratio with ethyl acetate with periodic shaking for 1 hour. Extraction efficiency, calculated by comparing peak areas from extracted and derivatized samples with peak areas from controls (derivatized only) was calculated to be on average  $0.97\% \pm 0.2\%$  ( $N = 3$ , error = standard deviation). Samples were dried under nitrogen gas and 100  $\mu$ L of the derivatizing agent, N,O-bis(trimethylsilyl) trifluoroacetamide with trimethylchlorosilane (BSTFA+TMCS, 99:1, Sigma), was added to the tube. The samples were heated to 60°C for 30 minutes and were subsequently analyzed.

### **2.2.9 GC-MS Instrumentation**

An Agilent 6890N model gas chromatograph with an Agilent 5975 quadrupole mass analyzer (Agilent Technologies, Santa Clara, CA) was used to quantify derivatized HU supernatant samples. The GC column was an Agilent HP-5MS capillary column (30 m  $\times$  0.25 mm) with a 250  $\mu$ m thick film of 5%-phenyl-methylpolysiloxane as the stationary phase. Ultra high purity helium was the carrier gas with a flow rate of 1mL/min. Samples were manually injected using a 10  $\mu$ L syringe (Hamilton) syringe to inject 1  $\mu$ L of sample. Samples were analyzed using the parameters in Table 2.1 and by using selective ion monitoring (SIM) of  $m/z$  147 and 292 to reduce the background associated with the derivatizing agent and other derivatized products. The protocol below was adapted from several previous studies using GC-MS to quantify HU concentration in biological samples,<sup>130,131</sup> and the inspiration for the measurement was derived from a teaching protocol developed by A/P lab coordinator Kathy Severin in the Department of Chemistry at Michigan State University.

The derivatized HU, identified by established peaks in its mass spectrum ( $m/z$ : 147, 277, and 292), had a retention time of 4.32 minutes. The internal standard had a retention time of 4.11 minutes. The primary  $m/z$  used to identify derivatized HU and naphthalene in the SIM program were 147 and 128, respectively. Secondary ions to identify analyte and internal standard were 292 and 277 for derivatized HU and 102 for naphthalene and are shown below in Figure 2.8.

Parameter	Value
Injection volume	1 $\mu$ L
Inlet Temperature	250°C
Inlet type	splitless
Column	Non-polar HP5MS
Initial Temperature	100°C for 1 minute
Temperature Ramp	20°C/min
Final Temperature	200°C for 1 minute
Total run time	7 minutes
Detector Temperature	280°C
Ion detection range (m/z):	45 – 300

**Table 2.2** Parameters for GC-MS analysis of RBC samples incubated with HU.

The detection limit for HU was approximately 36  $\mu$ M based on the ratios for blank measurements. Peak areas for derivatized HU and naphthalene were obtained by integrating peaks using Chemstation software. Peak areas were normalized to the corresponding naphthalene peak area and were plotted against the amount ratio. The concentration of HU remaining in the sample was calculated using the relationship generated from the linear regression.

#### **2.2.10 Treatment of Data**

Chemiluminescence and fluorescence intensity values for all samples were normalized to the respective 7% RBC control. Error for the normalized control (7% RBCs) was calculated by multiplying the standard deviation of the raw signal (fluorescence or chemiluminescence) by the inverse of the average raw signal. A background subtraction was performed for all NO fluorescence data. The background was determined by measuring the fluorescence intensity of wells after flowing PSS through channels for 30 minutes with 10  $\mu$ M DAF-FM and cultured bPAECs in the detection well. This background was subtracted from fluorescence intensity values of samples with RBCs. Student's t-test was performed to determine statistical significance.

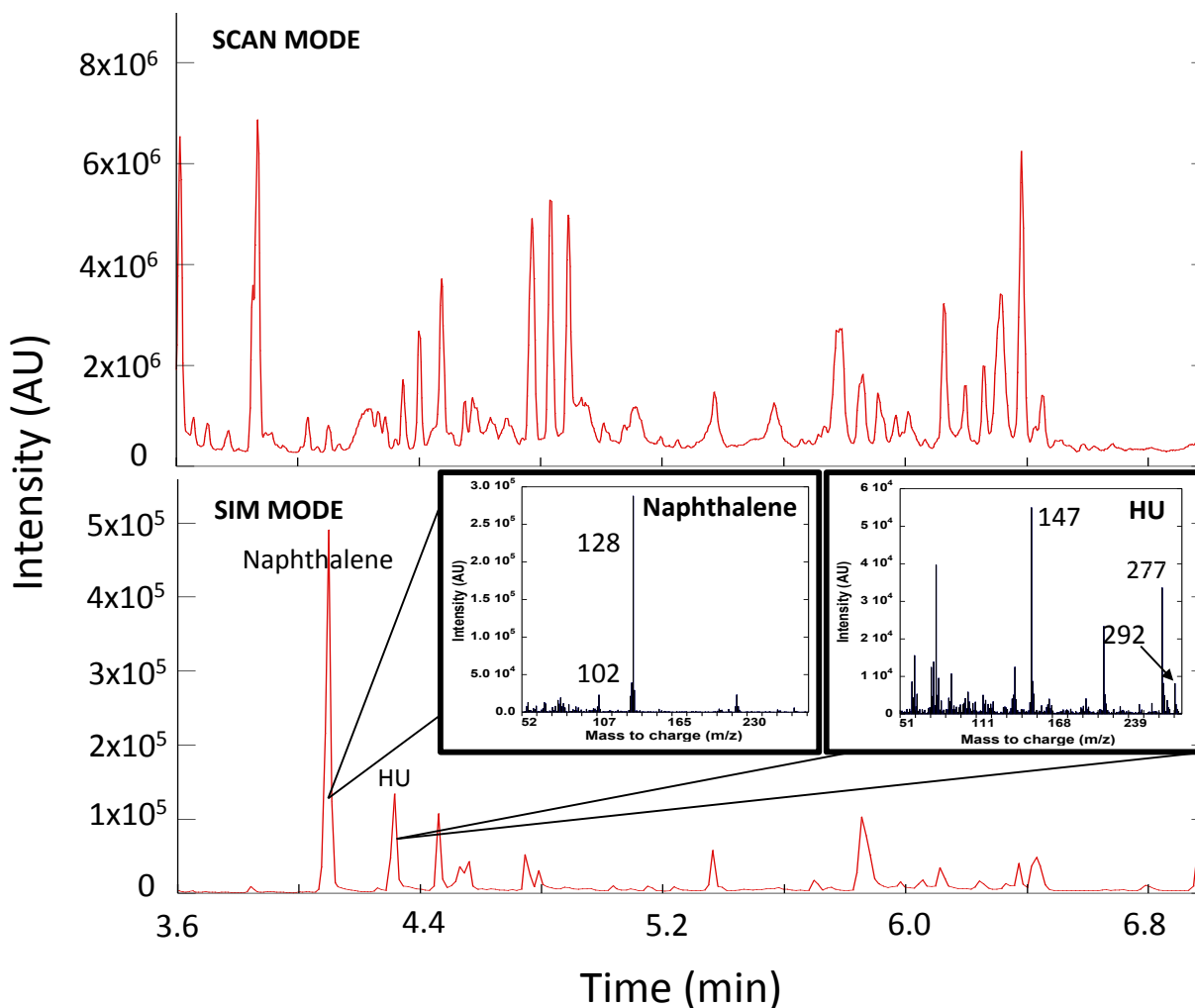


**Figure 2.8** Representative chromatograms and mass spectra of derivatized HU and naphthalene with and without SIM. Note that the background from derivatization reagent and resulting products dominate the chromatogram, making SIM necessary to quantify the derivatized product of HU.

## 2.3 Results and Discussion

### 2.3.1 Flow-Induced Deformation is Required for ATP Release from HU-Incubated RBCs

From previous studies in the Spence lab, it was established that flow deformation is required to observe an increase in ATP release from rabbit RBCs incubated with HU.<sup>78</sup> It was also established that the magnitude of ATP release depended on the concentration of HU in the sample, suggesting that some optimal dose exists that maximizes release of ATP from RBCs.

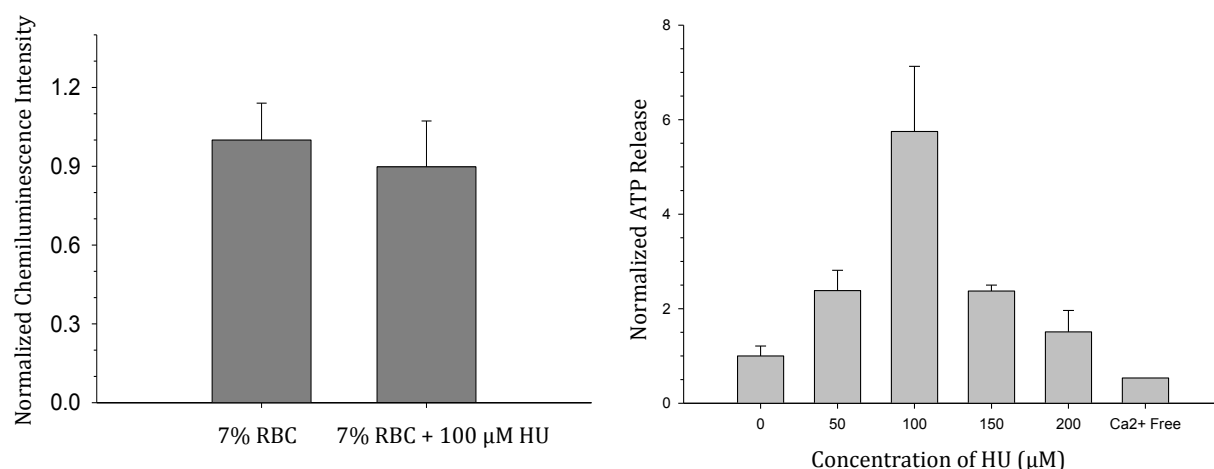


**Figure 2.9** ATP Release from 7% RBCs under static (non-flow) conditions (left) and under flow conditions (right).<sup>5</sup> 7% RBCs were incubated with and without 100  $\mu$ M HU for 30 minutes. The static ATP release was measured by mixing equal volumes of LL and sample and then reading the resulting chemiluminescence using a plate reader (N = 3 plates. Error is S.E.M.). ATP release from HU-incubated human RBCs was not significantly different than controls under static conditions. HU-incubated human RBCs released significantly more ATP relative to controls when pumped through silica capillary tubing. Flow data was collected using the method outlined in Figure 2.7. ATP release from RBCs increased with increasing concentration of HU until about 100  $\mu$ M HU. With more HU added to the sample, the RBC ATP release decreased to basal levels, which suggests that HU can act to either increase RBC deformability or to stiffen the cell. N  $\geq$  3 donors, except 150  $\mu$ M (N = 2) and Ca<sup>2+</sup> free (N = 1). Error is S.E.M.

The requirement of flow deformation to observe an increase in ATP release from HU incubated RBCs holds in the case of human RBCs, as shown in Figure 2.9. The magnitude of ATP release from human RBCs also varies with increasing concentration of HU, as shown in Figure 2.9. Taking this and previous studies into account, human RBCs were incubated with 100  $\mu$ M HU in all subsequent studies.

### 2.3.2 HU-Induced ATP Release from Human RBCs on a Microfluidic Device

ATP Release, which is directly proportional to measured chemiluminescence intensity, from human RBCs incubated with HU is shown in Figure 2.10. Human RBCs were treated with or without HU and various inhibitors of ATP release. Samples were flowed using a syringe and syringe pump through a microfluidic device as shown in Figure 2.6. When 7% RBCs were incubated with 100  $\mu$ M HU for 30 minutes and were subsequently flowed through the device, ATP release increased

$2.06 \pm 0.37$  times relative to the 7% control sample, which is typically 100-200 nM when quantified. When samples were incubated with established inhibitors of RBC ATP release, such as diamide (100  $\mu$ M) or glybenclamide (100  $\mu$ M), the observed release was significantly lower,  $0.41 \pm 0.13$  and  $0.34 \pm 0.08$ , respectively. Diamide inhibits ATP release by decreasing the deformability of the RBC,<sup>132</sup> and glybenclamide inhibits ATP release by blocking CFTR.<sup>45</sup>

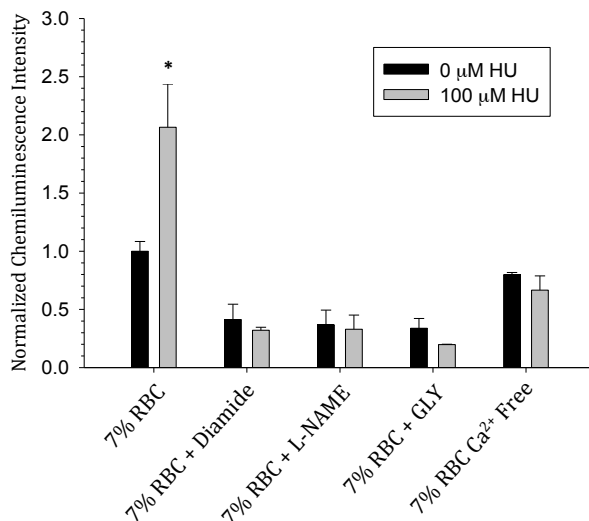


**Figure 2.10** ATP Release from human RBCs incubated with HU and with various inhibitors.<sup>5</sup> Data were collected by employing the device shown in Figure 2.6. When incubated with HU, 7% RBCs released significantly more ATP (2-fold more) than controls (\* $p < 0.001$ ). When 7% RBCs were incubated with various inhibitors, ATP release significantly decreased in all inhibitor trials with or without HU incubation ( $p < 0.05$ ) regardless of the presence of HU.  $N \geq 3$  donors. Error is S.E.M.

RBC ATP release was also inhibited by incubation of 7% RBCs with 100  $\mu$ M of the competitive NOS inhibitor L-NAME ( $0.37 \pm 0.13$ ), supporting previous data published with rabbit RBCs.<sup>78</sup> Preparation of RBC samples with Ca<sup>2+</sup>-free PSS also inhibited ATP release from human RBCs ( $0.80 \pm 0.02$ ). It is known that the RBC has a NOS that requires Ca<sup>2+</sup>/calmodulin for activation.<sup>133</sup> When the RBC is deprived of Ca<sup>2+</sup>, HU-induced ATP release is compromised. This further supports the hypothesis that RBC NO plays a role in the mechanism of HU-induced ATP release. It is notable that the effects of the various inhibitors on ATP release from HU-incubated RBCs were observed regardless of whether 100  $\mu$ M HU was present in the sample or not (black

versus gray bars).

### **2.3.3 ATP-Mediated NO release from bPAECs**

The effect of RBC-derived ATP on NO release, directly proportional to fluorescence intensity, from a cultured endothelium can be seen in Figure 2.11. When RBCs incubated with 100  $\mu$ M HU were flowed under a cultured endothelium, as detailed in the middle panel of Figure 2.4, bPAECs released on average  $1.34 \pm 0.10$  times more NO than controls (first set of bars). To confirm that RBC-derived ATP elicits an increase in NO released from a cultured endothelium and that the observed effect was not due to lysis, 7% RBCs were flowed under a cultured endothelium that had been incubated with the purinergic receptor inhibitor PPADS, which blocks ATP from binding to the P<sub>2</sub>Y receptor on the surface of the endothelial cells. As hypothesized, a decrease (10% - 20%) in NO release from the PPADS-incubated endothelium was observed when a 7% RBC sample was flowed underneath.

When the cultured bPAECs were incubated with NOS inhibitor L-NAME (third set of bars), a decrease in released NO was observed, as expected. However, when RBCs incubated with L-NAME (fourth set of bars) were flowed under a cultured endothelium, a decrease in released NO of approximately 20% from bPAECs was observed, suggesting dependence on RBC-derived NO. When both red cells and cultured bPAECs were incubated with L-NAME (fifth set of bars), no additional NO release was observed.

### **2.3.4 Measuring HU Uptake by RBCs**

When 7% RBCs were incubated with 100  $\mu$ M HU, approximately  $91.7 \pm 6.5$   $\mu$ M of the HU was taken up by the RBC compared to controls ( $0.86 \pm 2.3$   $\mu$ M) as is shown below in Figure 2.12. This initial data, with a sample set of only two donors, suggests that it would be feasible to use this GC-MS method to generate binding data and eventually a binding curve for HU and the RBC.

The determination of the binding number of HU to the RBC would aid in elucidating the molecular level interaction between the small molecule and its hypothesized target, the RBC. Fur-

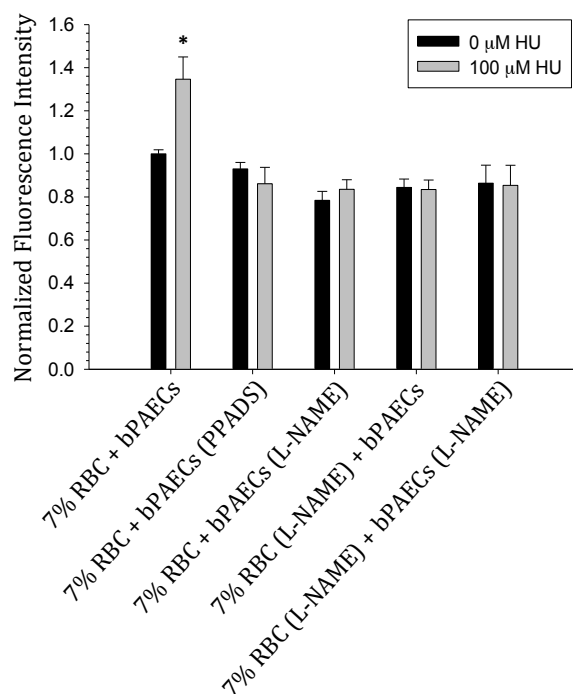


**Figure 2.11** NO Release from cultured bPAECs stimulated with 7% RBCs incubated with and without HU.<sup>5</sup> When 7% RBCs incubated with HU are flowed under a cultured endothelium, the NO released from the endothelium increases approximately by 30% compared to controls (first set of bars). When the  $P_2Y$  receptor of the endothelium is blocked using the antagonist PPADS, the NO release from the endothelium decreases significantly (second set of bars). When NOS in the endothelial cell is inhibited with competitive inhibitor L-NAME, NO release is also lowered (third set of bars), as is the case when RBCs are incubated with L-NAME (fourth set of bars) and when both RBCs and endothelial cells are incubated with the NOS inhibitor (fifth set of bars). The asterisk (\*) indicates that the NO release from bPAECs incubated with HU is statistically different than the release observed in controls and in all inhibitor samples.  $N \geq 3$  donors. Error is S.E.M. \* $p < 0.005$ .

ther study of the HU uptake with concentrations (0 - 200  $\mu$ M) is currently in progress in order to generate a binding curve. If this experiment does suggest that a binding event or uptake occurs, it would be necessary to also investigate if the uptake can be blocked by inhibitors of ATP release, such as diamide.

With the detection limit of the method appearing to be in the low micromolar range (approximately 36  $\mu$ M), further method development may be necessary depending firstly on if a classical binding relationship can be observed and secondly, at what concentration the saturation occurs. For example, the chromatogram prior to applying the SIM method is dominated by derivatized



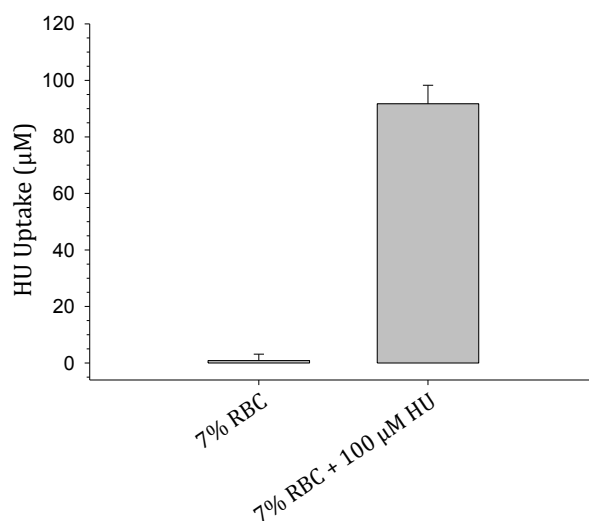


**Figure 2.12** HU uptake by RBCs. RBCs were incubated with 0 and 100  $\mu\text{M}$  HU in PSS for 1 hour after which the extraction method described was performed. Measurement of supernatant HU suggests that the RBCs incubated with HU for 1 hour uptake nearly all HU in the sample.  $N = 2$  donors. Error is S.E.M.

products from the derivatization step of the protocol, and relevant peaks from the analyte in particular are buried in the noise, making SIM necessary to confidently quantify. It is unlikely that adding an additional evaporation step to remove such contaminants after derivatization to clean up the chromatogram and would lower the detection limit. If the method doesn't prove to be robust enough to measure the uptake, alternative methods can be used, such as an electrochemical method using carbon electrodes that doesn't require HU derivatization<sup>134</sup> or an LC-MS method without derivatization could be developed.

## 2.4 Conclusions and Future Work

Previous work from the Spence group on HU's effects on rabbit RBCs has been validated and has been demonstrated to apply to human RBCs. It has been shown using an *in vitro* fluidic platform that HU increases flow-deformation induced ATP release from human RBCs, and that a potential fate of the RBC-derived ATP is diffusion to adjacent endothelial cells resulting in an increase in endothelial NO release. This provides evidence that HU treated RBCs are capable of inducing

smooth muscle dilation. Since the effects were observed after 30 minutes to 1 hour after incubation with reagents, this work provides a potential explanation of the immediate effects on blood flow and vascular tone that is observed in patients with sickle cell disease after beginning treatment with HU. Additionally, the data strengthens the evidence that RBCs incubated with HU function better as regulators of blood flow because the HU-incubated RBC becomes more sensitive to shear stress, i.e., more ATP release from the RBC with equivalent shear force applied.

In this case, one can imagine if an RBC treated with HU encounters shear force in the vasculature, it will release an increased amount of ATP to dilate the vessel relative to its control counterpart. As a result of the increased vessel dilation, the HU-incubated RBC can modulate (increase) blood flow, allowing it to travel more quickly back to the lung bed for reoxygenation. If the relationship between HU concentration and RBC ATP release holds true for HbS containing RBCs, this would suggest that HU treatment stifles RBC sickling by decreasing the time it takes for the RBC to return to the lung bed. This could account for the improvements in vascular tone and less hemolysis observed in patients clinically.

We hypothesize that HU incubation increases RBC-derived NO and that this NO makes the RBC more deformable and as a result more sensitive to applied shear stress, resulting in increased ATP release when subjected to flow deformation. The improvement in blood flow observed clinically in patients taking HU would stem from an increased ability of the RBC to dilate blood vessels, i.e., the RBC becomes more sensitive to deformation as a stimulus when exposed to HU and thus releases more ATP when exposed to some amount of shear stress. This could be further investigated by designing experiments to measure RBC ATP, an indirect measurement of deformability, when RBCs are subjected to systematic variations in applied shear stress by modulating the capillary diameter or flow rate in an experimental system like in Figure 2.7. If this is the case for RBCs from sickle cell anemia patients taking HU, it suggests that the drug can improve the RBC's ability to regulate blood flow and consequently oxygen supply. For example, when a sickle cell patient's RBCs deliver oxygen to tissues, the polymerization process begins and after a certain point, it becomes irreversible, and the cell is lost permanently. If the RBC had the ability to dilate

the vessel to get back to the lungs more quickly, it could stave off the irreversible polymerization and save itself.

However, HU may impart another protective property to the RBC. Electron paramagnetic resonance data from a previous study<sup>78</sup> confirmed the presence of nitrosylated hemoglobin in 7% samples incubated with spermine NONOate. It is possible that HU could decrease the chance that a cell would irreversibly polymerize by making the RBC a better modulator of blood flow, i.e., it would travel back to the lungs faster. However, it could also function to increase RBC NO which can bind to Hb, preventing polymerization of HbS in the case of a sickle cell patient. These hypotheses could explain why a patient on HU has less frequent crises. However, further experiments would require RBCs obtained from a patient with sickle cell anemia, and also the measurement of RBC NO, which was measured in collaboration with the Martin Group at Saint Louis University<sup>7</sup> and will be discussed in Chapter 3. RBC NO has been measured by the Spence group previously, except it was in the context of hypoxia.<sup>49</sup>

## CHAPTER 3

### 3D PRINTED TECHNOLOGIES TO ENABLE STUDY OF HYPOXIA-INDUCED RELEASE OF RBC SIGNALLING MOLECULES

#### 3.1 Hypoxia-Induced ATP Release: A Deformation-Induced Stimulus

Hypoxic ATP release from the RBC is hypothesized to be a subset of the physical deformation mechanism, as discussed in Chapter 1 (see Figure 1.1). Evidence in the literature observed in the late 1970s established that while Hb is present in the cytosol of RBCs, it is localized to the RBC membrane and can specifically and reversibly interact with the anion exchange channel protein, Band 3.<sup>135</sup> This finding is now credited to more recent Forster resonance energy transfer (FRET) studies performed on purified RBC membranes and on model lipid bilayers by Eisinger and Flores in the 1980s.<sup>136–139</sup>

Band 3 participates in the mechanism of ATP release from the RBC by balancing the membrane potential. Not much later, a more detailed study of the binding interaction using synthetic peptide sequences confirmed the binding observations.<sup>140,141</sup> The interaction between Band 3, a 93 kD transmembrane glycoprotein, and Hb is postulated to occur as a reversible binding event at Band 3's amino terminus that is electrostatic in nature and is enhanced by divalent cations.<sup>135,142</sup> Some had postulated that Hb was actually an integral component of the membrane, due to the inability to obtain hemoglobin-free RBC membranes (ghosts);<sup>143</sup> however, this has since been challenged with exchange studies using labeled Hb that indicate that all of the Hb in RBC membranes is exchangeable.<sup>144</sup> Hb affinity to the RBC membrane has been shown to vary based on its oxygenated state,<sup>145</sup> with deoxyhemoglobin's binding constant being 2 orders of magnitude larger than that of oxygenated hemoglobin. This significant difference in affinity has since been confirmed by studies of Hb binding experiments with synthetic Band 3 peptide mutants.<sup>43</sup> The amino terminus of Band 3 also interacts with RBC skeletal proteins ankyrin and Band 4.2 as well as cytoplasmic proteins including aldolases, glyceraldehyde 3-phosphate dehydrogenase and phosphofructokinase.

Specifically, when Hb undergoes the transition from tense to relaxed, resulting in the release of oxygen, it is thought that the change in conformation of the heme unit within Hb physically pulls at the membrane, activating the G-protein coupled receptor to induce the signal cascade (see Chapter 1) that results in ATP release from the RBC. Previous work from the Spence lab has shown the ATP release from RBCs exposed to deformation and hypoxia, alone and then together, is non-additive, further supporting that the two mechanisms are affecting the cellular ATP release through the same mechanism.<sup>34</sup> This was accomplished by measuring the ATP release from RBC samples subjected to shear stress or hypoxia. The release observed from each stimulus was compared to ATP release from RBC samples subjected to both stimuli, and no significant difference between the three values was observed.

One aspect of ATP release that has not been investigated is its dependence on the dissolved oxygen tension. It is the aim of this chapter to probe that relationship and expand our understanding of this dependence to RBC NO release. There are various methods and platforms to enable study of hypoxic red cell samples, each having their advantages and disadvantages, however, using the soft polymer microfluidic platform discussed in Chapter 2 was not desirable for a variety of reasons, namely the serious lack in reusability and rigidity of the devices. In addition, PDMS is fairly gas permeable, making the oxygen in the sample difficult to control, affecting measurement reproducibility. The next section introduces a platform that proved to be highly amenable to measurement of oxygen in a flowing sample via inclusion of an integrated Clark-type electrode.

## **3.2 3D Printed Devices for Applications in Chemistry**

Since their establishment as tools to enable bioengineering applications, 3D printed materials have become more popular in the chemical sciences. Several thorough reviews cover the various printing mechanisms and their applications.<sup>146–152</sup> The type of printing used to fabricate the devices presented in this chapter is termed “poly-jet”, whereby a layer of liquid photopolymer is deposited on a stage and is subsequently cured with UV light, as shown in Figure 3.1. The manufacturer’s reported resolution for the poly-jet technology is 100  $\mu\text{m}$  (XY) and 16  $\mu\text{m}$  (Z). The Spence lab

has printed 100  $\mu\text{m}$  wide channels, but without a way to clear the support material, the dimensions of the channel cannot be confirmed. Sonication and compressed air works well, but was not successful in clearing the material, and forced flow using a syringe pump resulted in high enough back-pressure that leaking occurred, thus prohibiting channel clearance.

The first reports of 3D printed materials for biochemical device development comes from a collaborative effort at the University of Chicago. Using fused deposition modeling as the printing technique, the authors were able to print a device out of thermoplastic to be used as a custom device for neurological perfusion studies.<sup>153</sup> More recently, the Cronin group at the University Glasgow, has generated 3D printed labware to facilitate continuous-flow organic reactions as well as a multi-channel fluidic device to demonstrate the platform's ability to enable a variety of reactions (organic, inorganic, and materials synthesis).<sup>154–158</sup>

The cost of 3D printing varies on the user's needs. For example, the Objet Connex 350 in the Department of Electrical and Computer Engineering at Michigan State University costs approximately \$250,000, not counting replacement material and other operating costs. Fabrication of the device shown in Figure 3.2 is approximately \$30. The cost of a typical stereolithography setup includes the cost of a spin coater, silicon wafers, photopolymer, other reagents, specialized hot plate, and a UV flood source with timing controls, which is arguably the most expensive piece of equipment in the assembly.

To fabricate a single master takes equivalent if not less time than the 3D printed devices in this chapter, as the Connex 350 in the engineering department is a user facility. Additionally, a master is arguably cheaper on average to fabricate than a 3D printed device considering all costs. While it is tempting to compare the fabrication efficiency between 3D printing and photolithography (from Chapter 2) and the cost of instrumentation/materials, it is more important to consider the scientific motivation for switching to a new experimental platform, considering that the Spence lab has been traditionally a microfluidics group since the early 2000's. With traditional microfluidics used in biological experiments, devices are single use, meaning that the user must fabricate replicate devices for replicate experiments. While it may be possible to clean microfluidic channels and

remove adhered protein using bleach or organic solvent for reuse, the ruggedness of the material cannot withstand multiple uses with leaking occurring after 6-8 hours of continuous use, even with new devices. The variability between the devices can affect the error in the measurement, and it is important to note that the success of a device tracks with the skill of the user, which is a limiting factor in obtaining desired data.

With 3D printed devices, replicate device fabrication is unnecessary after dimensions have been optimized, which can take a few rounds of printing to accomplish. However, a 3D printed device is indefinitely reusable. After a biological study, the device can be soaked in 10% bleach or autoclaved and reused, the former being the preferred method of sterilization as repeated autoclaving effects on photopolymer material stability have not been well-documented. The reusability, as well as the material ruggedness, make 3D printed devices a desirable alternative to traditional soft polymer materials for biological studies. However, one drawback to the material is that its rigidity is not as well controlled as in traditional soft polymer materials. This can be an issue for cell culture on the device, although recent results from our lab suggest that surface modifications to 3D printed channels provide a solution to this issue (Gross et al. *In Preparation*).

Another advantage to 3D printed materials is the ease of which devices can be integrated with preexisting commercial equipment and parts. While soft polymer devices have the capability of integration with plate readers,<sup>49</sup> their physical stability is a challenge for the inexperienced user, and device-to-device variation can affect measurements. 3D printed devices can be made to fit directly into 96-well plate holders in commercial plate readers or amenable to other commercial equipment such as fluidic handling systems. The rigidity and reusability of the materials are major benefits.

3D printed devices also have the capability to be integrated with commercial parts, such as finger-tight fittings and transwell membrane inserts, as shown in Figure 3.11. Traditional soft polymer integration with other materials is feasible and has been performed for some time,<sup>159–163</sup> but the skill and reproducibility of placement can affect reproducibility in biological measurements. Consider for example, integration of electrodes into traditional soft polymer devices. Typically

this is accomplished by placing wire electrodes in-line or into (perpendicular to) the channel, or by coating a liquid electrode material or paste below the channel.<sup>163,164</sup> While these techniques have been successful, the measurements can suffer from decreased precision because of variation in the electrode surface area exposed to the sample and a new device must be fabricated for replicate experiments.

One limitation to 3D printed materials, as compared to traditional polymer devices, is the control over channel dimensions, specifically with respect to channels with sizes in the x or y dimensions that are less than 100  $\mu\text{m}$ . As mentioned above, a device with a 100  $\mu\text{m}$  size channel has been printed in the Spence lab, but confirming the channel dimension is futile if it cannot be cleared out using reasonable means (sonication, sodium hydroxide vapor, bristled brushes, etc.). In this respect, if channels with dimensions less than 100  $\mu\text{m}$  are needed for a specific application, traditional stereolithography with soft lithography is recommended. However, there are reports of other printing methods successfully printing devices with sub-100  $\mu\text{m}$  dimensions, and it is anticipated that as the printing technology develops, with more affordable printers coming on the market, the accessibility to high resolution 3D printers will improve.

The 3D printed device presented in Figure 3.2 allows the electrode to be housed in a threaded insert. This makes the electrode placement in the channel more reproducible every time an experiment is performed, and the ease of removal and installation of the electrode cuts down experimental preparation time. If the electrode becomes compromised or performance is questioned, the electrode can be removed and repolished. Alternatively, if multiple electrodes are fabricated, electrodes that become compromised during an experiment by fouling or other processes can be replaced immediately, and the experiment can continue with minimal interruption. If the device was soft polymer based or consisted of a multi-material device (soft polymer with epoxy embedded electrodes), the experiment would be interrupted until a new device was fabricated, unless the user had the foresight to fabricate replicates of each component of the device. Another benefit to the fitting-housed electrodes is that each electrode is reusable depending on the application, and the reproducibility of the process (preparation and placement in channel) decreases the variability



between experiments.

The RBC ATP release and oxygen measurements reported in this chapter were all performed on the same 3D printed fluidic platform shown in Figure 3.2, demonstrating the ruggedness and reusability of the platform. Oxygen control was not integrated with the device, however this device could be amended to include an oxygen control chamber upstream of the detection electrode. Classical oxygen detection and oxygen standard preparation methods are reviewed below.

### **3.3 Classical Oxygen Detection Methods and Integration with Microfluidics**

There are a variety of ways to measure molecular oxygen directly in a sample including iodometric titration (Winkler method),<sup>165–167</sup> fluorescence quenching using ruthenium based fluorophores, and amperometric reduction on platinum or gold electrodes.<sup>1</sup> Preferred methods directed at measuring oxygen tension in a biological sample include luminescence and amperometric methods, as the Winkler titration is not as easy to use with biological samples because it requires addition of reagent to the sample. In addition, the timescale of the method is not amenable to the timescale of some biological measurements, e.g., measuring oxygen while a cell is releasing some metabolite.

Ruthenium-based fluorogenic probes and other fluorogenic probes like platinum (II) octaethylporphyrinketone<sup>168</sup> have proven useful as indicators of oxygen tension in biological samples. One application of the ruthenium bipyridine dyes is as an indicator of oxygen tension in a cell culture exposed to a controlled oxygen gradient.<sup>169</sup> The advantage to a luminescent-based sensor is its relative ease of fabrication and integration into fluidic channels compared to commercial Clark electrodes, which are too large to integrate with micron-sized channels. There are micro-machined Clark electrode fabrication protocols available, but these suffer from the issue of reusability.<sup>170–173</sup> A ruthenium dye can be spin-coated onto a slide and incorporated into the fluidic device or can be coated on the surface of the device itself.<sup>174–176</sup> The area of the ruthenium layer allows the user to gain temporal information of oxygen concentration as well as higher resolution spatial information, which is poor with the Clark electrode. There are Clark electrode arrays, which exhibit improved resolution relative to a single electrode.<sup>177</sup> Although there are reports in the literature of

using ruthenium-based dyes with mammalian cells without appreciable effect on cell viability, the dyes are reportedly toxic to cells. Another challenge with the ruthenium based dyes is that they are not amenable to use with RBC samples because of the optical interferences with hemoglobin. There are other dyes (platinum (II) octaethylporphyrinketone) that are amenable to use with red cell samples as the excitation wavelength is shifted to around 600 nm.<sup>178</sup> However, one common disadvantage between incorporation of the micro-machined Clark electrodes and ruthenium based dyes is that they are still incorporated with PDMS based materials, and if these devices are used in biological studies, they are not reusable. Even though both Clark electrodes and spin-coated dyes are reusable, they are limited in their utility by the single-use nature of PDMS with biological samples. There are clever ways around this issue, which include making the devices more modular in order to keep the oxygen sensor separated from the biological sample, allowing the sensor to be reused.<sup>1</sup>

The principles behind electrochemical oxygen detection, either dissolved in solution or in the gas phase, have changed significantly since the inception of the technique in the mid 1900s. A review by Severinghaus documents the development of electrochemical oxygen detection with more detail than in the following description.<sup>179</sup> Electrochemical reduction of oxygen was discovered in 1897 by Daneel and his now well-known advisor, Nernst. The first electrochemical detection technique for oxygen and other species in solution, termed polarography, was developed by Jaroslav Heyrovsky in Prague, supposedly by accident. The technique, for which Heyrovski would receive the Nobel Prize in 1959, required a mercury drop electrode and allowed the first measurements of oxygen in plasma from patients by Henry Beecher in 1942. The move to solid metal electrodes, namely platinum and gold, is credited to biophysicists Davies, Brink, and Bronk who were taking tissue oxygen measurements at the University of Pennsylvania in the mid-1940s. To prevent fouling of the electrodes when exposed to blood, Leland Clark secured various membrane materials (cellophane, silicone, polyethylene) to the electrode surface to protect the solid metal electrodes from the biofouling components in blood. Further development of the Clark electrode has not strayed much from Clark's original system. In microfluidic applications, efforts are

mostly focused on miniaturization of the electrode system to enable integration with micron-sized channels.<sup>170,173</sup> Clark electrodes typically consist of a gold or platinum working electrode and a platinum or silver-silver chloride reference electrode. The electrode is typically coated with a gas permeable material, as described above to prevent electrode fouling. The working electrode is negatively biased against the reference to reduce oxygen at the surface. This reaction generates hydroxide, which can affect electrode stability (see Figure 3.8, bolded reaction).

### 3.4 Controlling Oxygen Tension in a Flowing Sample

To control the oxygen tension in a biological sample for *in vitro* experiments, one can use purging methods or the reagent Oxyrase. Oxyrase is commonly used in biological studies to probe the effects of hypoxia; however, the biological relevance of these studies is questionable due to the nature of the reagent. Oxyrase is a proprietary enzymatic cocktail of oxygenases that can deoxygenate a solution in 30 minutes when used in the recommended 1:10 v/v ratio with a sample. The deoxygenation of the sample is uncontrolled, which makes the reagent undesirable to those trying to probe intermediate oxygen tensions as stimuli, e.g., any intermediate oxygen tensions in the physiologically relevant range between normoxia and anoxia (see Chapter 1). Even if deoxygenation was slowed by modifying the ratio of Oxyrase to sample, it is not clear whether the rate can be controlled to apply a desired oxygen tension for some interval of time. The uncontrollable nature of the Oxyrase system makes purging methods a more attractive option for the studies described in this chapter.

Purging methods can vary in their physical setup, with some methods employing hypoxic chambers that allow mixing of gases to control the oxygen tension in solution and other methods that directly purge samples with compressed gases. To generate samples using compressed gas, purging with compressed air and an inert gas like nitrogen or argon and mixing the purged stocks solutions to generate the desired oxygen tension is common, and this has been performed by other labs to prepare NO gas standards. Calibration for these types of systems requires calculation of dissolved oxygen in solution, and the calculations performed for the set of experiments in this

chapter are described in the next paragraph.

The atmosphere consists of 21% oxygen. This percent is representative of the partial pressure of oxygen (160 mmHg) relative to the total pressure of the atmosphere (760 mmHg or 1 atm). The concentration of dissolved oxygen in a solution purged with compressed air can be calculated using Henry's Law ( $P = k_H c$ ), where  $P$  is the partial pressure of the gas,  $k_H$  is Henry's constant for the gas, and  $c$  is concentration of the dissolved gas. For air-purged water, the concentration of oxygen in solution is approximately 0.27 mM, with the assumption that Henry's constant for molecular oxygen is 769.23 atm\*mol/L at 298 K.

If the Henry's law calculation is based on reported oxygen solubility ( $1.39 \times 10^{-3}$  mmol/mmHg), the same form of the equation is used, except solubility is substituted for  $k_H$ . However, the calculated dissolved oxygen concentration does not differ significantly (approximately 0.22 mM versus 0.27 mM). By mixing a solution of air-saturated buffer with a solution purged with an inert gas like argon in a syringe, various oxygen standards can be prepared. This method avoids the use of compressed oxygen, which is not required to make the relevant oxygen standards and for which special safety measures would be required. These values do not take into account the "salting out" effect, in which the dissolved oxygen content of a solution can decrease based on the concentration of salt in solution. However, considering that the solubility of oxygen between fresh water (0 g salt/ kg water) and sea water (35 g salt/ kg water) varies only 20% at room temperature, the effect was not anticipated to contribute significantly to error in the buffers used (approximately 9 g salt / kg of water).

Described below are the methods used to prepare oxygen standards and RBC samples in order to probe the dependence of ATP release on dissolved oxygen. The oxygen tension in the sample was measured using a Clark-type electrode housed in a figertight fitting, and ATP was measured using the classic luciferin-luciferase enzyme system introduced in Chapter 2. All of these measurements were performed on a 3D printed fluidic device printed in the Department of Electrical and Computer Engineering at Michigan State University. Also described in this chapter are measurements of RBC NO release, performed on a variety of platforms including a hybrid epoxy-PDMS

based system as well as 3D printed devices.

## 3.5 Methods

### 3.5.1 Fabrication of 3D Printed Device

All devices were printed with an Objet Connex 350 multi-material 3D printer using the proprietary acrylate-based polymer material VeroClear. Support material was removed from the device using compressed air, sonication, and other physical means such as clearing channels with capillaries or bristled brushes.

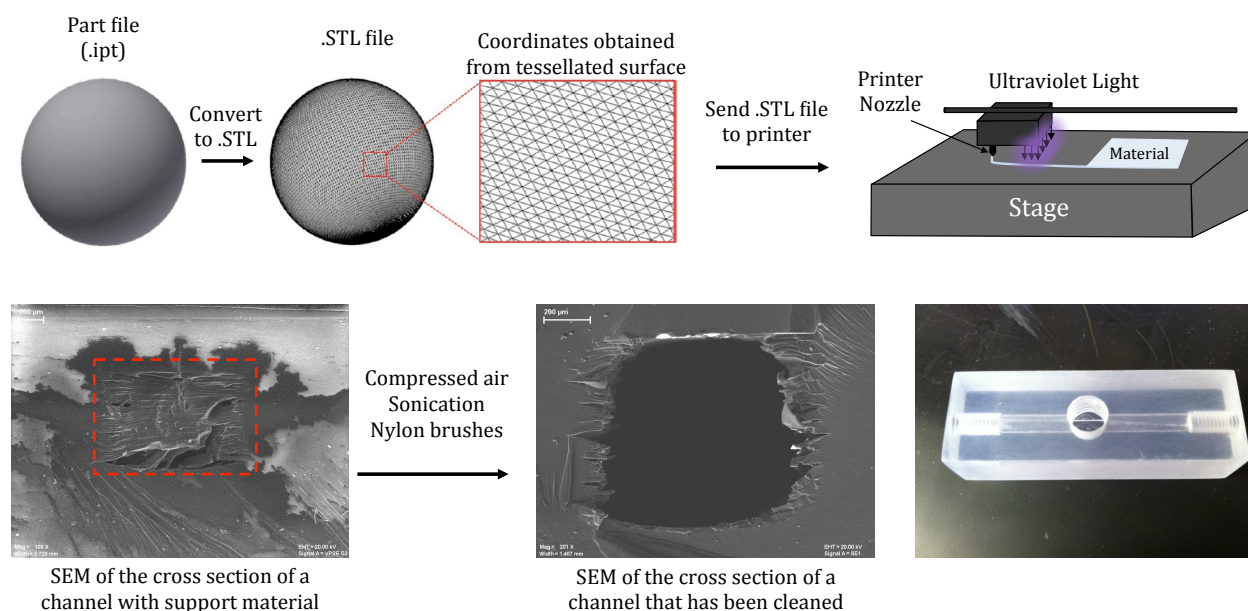


**Figure 3.1** 3D printing process from part file to device printing and cleaning.

The device design begins in CAD software, specifically Autodesk Inventor Student Edition. The part file is converted to an .STL file, where the tessellated surface of the device generates coordinates that are saved in the file as is shown in the top panel. The printer can read the coordinates from the .STL file in order to print the device in a layer-by-layer fashion. The printing head has a nozzle from which to dispense the proprietary, acrylate-based photopolymer and a UV light that follows the nozzle in order to initiate polymerization of the photopolymer. The printer dispenses

and subsequently cures the material in a layer-by-layer manner and builds up the material in the Z direction to make the desired shape dictated by the .STL file. After the device is printed, support material is present in any void space in the device and can be seen in the SEM images of a channel cross section (red outline). Support material is cleared by using compressed air, sonication, and brushes to physically remove material (SEM on right). One of the first printed devices designed for oxygen measurements is shown in the bottom left.

All devices were designed using Autodesk Inventor Professional 2014 Student Edition. Devices were saved as a part file and were converted to an .STL (stereolithography or standard tessellation language) file for submission to the printer, which is housed in Michigan State University's engineering department. The .STL file format stores the dimensions of the device as coordinates that are obtained from the tessellated surface of the device shown in Figure 3.1. Threaded ports for the electrode (6.8 mm in diameter) and for fluidic connection (4 mm in diameter), as shown in Figure 3.2, were designed in the Autodesk program and were printed so that the electrode and fittings could be directly integrated with no post-print modifications. Incorporated threading was 10-32. Threading can be incorporated into a part file by manually designing the threads in Autodesk, but there is also a plugin available (Thread Modeller) for download available online that will build the thread with the user's specifications and makes the process simpler. Ports for transwell insert incorporation (6.8 mm in diameter) were also printed on the device.

### **3.5.2 Fabrication of Electrodes and Surface Modifications**

#### **3.5.2.1 Au and Ag/AgCl Electrode for Oxygen Measurements**

Electrodes for oxygen detection were fabricated from Au and Ag wire (500  $\mu\text{m}$ , Sigma), each of which were secured to a copper wire with conductive epoxy. The connection was reinforced using J-B Kwik Weld. After curing, the two wires were insulated with heat shrink tubing and were embedded in a polyetheretherketone (PEEK) nut (3/16" o.d.) using a mixture of C-7 Epoxy resin and activator E (Armstrong). After the epoxy cured at room temperature for approximately 24

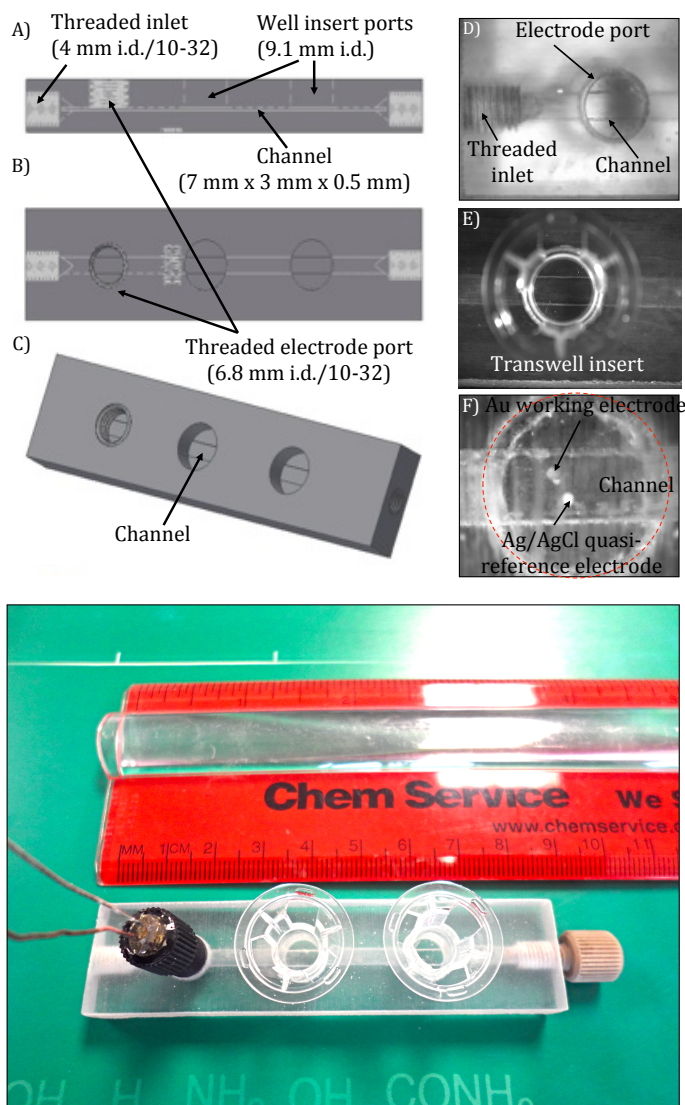


**Figure 3.2** Device to measure dissolved oxygen and ATP in a flowing sample.<sup>6</sup> The device has threaded ports for sample introduction and a channel (7 mm x 3 mm x 0.5 mm) through which samples were flowed. The device also has two wells to hold transwell membrane inserts for ATP detection and another threaded port to accommodate the oxygen electrode. All threading was fabricated during the printing process, i.e., threads were not tapped into the device post-print. A side profile of the device is shown in (A) a top view in (B) and a solid body profile in (C). The right panel of the figure shows the actual device with inlet, channel and threaded electrode port printed in VeroClear in (D), the transwell insert sitting in the detection wells in (E), and the arrangement of the electrodes in the channel when the electrode assembly is screwed into the device in (F).

hours, the assembly was baked in an oven at 70°C overnight to secure the placement of electrodes and to ensure adequate curing of the epoxy. Electrodes were wet polished first with rough grit (P500) and then with fine grit sand paper (P1000, P2000) until wires were exposed. Fine polishing

of the electrode surface was achieved by polishing with 0.05  $\mu\text{m}$  alumina powder (CH Instruments, Austin, TX).

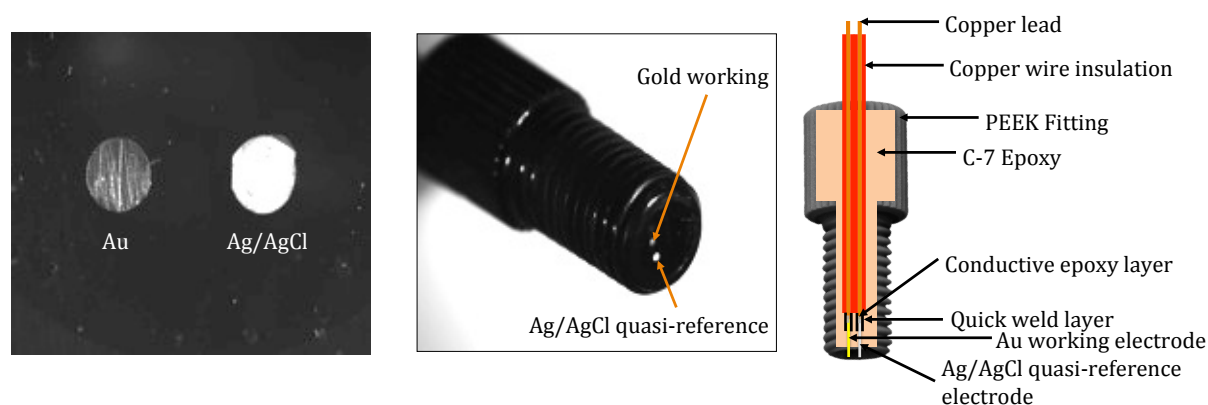


**Figure 3.3** Fabrication of PEEK embedded electrodes for Oxygen Detection. Microscopy images of Au and Ag/AgCl electrodes detailing surface and position in the PEEK fitting (left and middle). Electrode materials were secured to insulated copper wires using conductive epoxy as described and as shown above (right). The electrode-lead connection was secured with quick weld, and the electrodes were positioned inside a PEEK fitting and C-7 epoxy was poured into the fitting. The fabrication procedure for Pt electrodes shown in Figure 3.14 used for detection of NO was similar.

To prepare electrodes for measurement, the PEEK nut assembly was polished with 0.05  $\mu\text{m}$  alumina powder and was washed in DDW, sonicated and then dried at 70°C for approximately 10 minutes. After drying and cooling, AgCl was coated onto the silver electrode using 3M KCl, electrical leads, another silver wire, and a 9 V battery. After coating, the electrodes were lightly rinsed with DDW and dried. A Nafion coating (5%, Ion Power, New Castle, DE) was applied by dipping the PEEK nut into a solution of Nafion (2.5% v/v in isopropyl alcohol) and holding for approximately 10 seconds. After dip coating, electrodes were dried at room temperature for approximately half an hour prior to taking oxygen measurements. 2.5% Nafion was utilized for oxygen studies to ensure minimal small molecule diffusion through the layer. Even though Nafion is known to be a perm-selective membrane, only allowing positively charged small molecules through, it has been documented in the literature that anionic moieties can diffuse through the polyfluorinated polymer layer.<sup>180</sup> This observation was confirmed by voltammetric measurements using ferricyanide while varying the percent Nafion coating (not shown).



### **3.5.2.2 Pt/Pt-black Electrodes for Measurement of NO**

The electrode for NO measurements was fabricated similarly to the described oxygen electrode. However, in this case the electrodes consisted of a 250  $\mu\text{m}$  Pt working electrode to be coated with Pt-black and a 500  $\mu\text{m}$  Pt reference electrode. Connections to the electrode materials were reinforced by soldering or colloidal silver to copper wire, and the connections were insulated using heat shrink tubing. Electrodes were aligned and C-7 epoxy was poured into the PEEK fitting and was left to cure overnight. The fitting was sanded until electrodes were exposed with subsequent polishing with alumina powder. The Pt-black working electrode was prepared by electroplating the Pt-black onto the electrode surface. This was accomplished by scanning the potential of the 250  $\mu\text{m}$  Pt electrode between +0.60 V and +0.35 V (vs Ag/AgCl) at 20 mV/s in a solution of 3.5% chloroplatinic acid and 0.005% lead (II) acetate trihydrate (w/v).

### **3.5.3 Preparation of Reagents**

Hanks' Balanced Salt Solution (HBSS, 1.3 mM  $\text{CaCl}_2$ , 5.3 mM KCl, 0.4 mM  $\text{KH}_2\text{PO}_4$ , 0.5 mM  $\text{MgCl}_2$ , 0.4 mM  $\text{MgSO}_4$ , 138 mM NaCl, 4 mM  $\text{NaHCO}_3$ , 0.3 mM  $\text{Na}_2\text{HPO}_4$ , 5.6 mM glucose, Sigma) was used to prepare oxygen standards and 7% RBC samples and was used in the measurement of NO standards. Potassium ferricyanide (Sigma) standards were prepared from a 5 mM stock solution in 0.5 M sodium sulfate. Nafion (5%, Ion Power, New Castle, DE) was utilized in 2.5% for oxygen measurements and as 0.5% for NO measurements.

#### **3.5.3.1 Oxygen Standards**

Oxygen standards were prepared by mixing ratios of argon purged and air purged buffer solutions to yield the desired oxygen tension, and the calculated concentrations are displayed in the table below.

Purged solution oxygen tensions were confirmed with a commercial oxygen probe (Symphony SP70D, VWR). Ratios were obtained by using Henry's Law for calculations with the partial pres-

PPM O <sub>2</sub>	μM O <sub>2</sub>	mmHg O <sub>2</sub>	Air Purged Buffer (μL)	Argon Purged Buffer (μL)
0	0	0	0	500
2.19	68	40	125	375
4.37	137	79	250	250
6.56	205	118	375	125
8.74	273	158	500	0

**Table 3.1** Preparation of oxygen standards. Oxygen concentrations in various units are listed for convenience. The ratio of air-purged and argon-purged solutions for each sample is also listed.

sure of oxygen (0.20946 atm) and the appropriate Henry's constant (769.23 atm M<sup>-1</sup>) for oxygen. Buffers were allowed to purge with the appropriate gas for 30 minutes in round bottom flasks outfitted with suba-seal septa and a vent. After purging, the solution was removed from the gas lines and was kept air-tight. Samples were prepared in 500 μL syringes (Harvard) by using syringe adapters to draw up the appropriate volume of solution. It was necessary to not compromise the seal to the round bottom flask or to the syringe after removing the necessary solution. An electrochemical measurement of the two stock solutions was performed first before continuing to run standards in order to confirm that the two solutions were in fact deoxygenated and air-saturated. After solutions were prepared, the syringe adapter was removed, and the syringe was loaded onto a syringe pump. Samples were delivered at 6 μL/min through 200 μm i.d. capillary tubing to the 3D printed device.

### 3.5.4 Preparation of RBC Samples

7% RBC samples at various oxygen tensions were prepared as described above; however, the hematocrit of packed RBCs was taken into account in the calculation of buffer volumes, i.e., the volume of RBCs required (typically 50 μL) was subtracted from the calculated air purged volume. To prepare the samples, argon-purged and air-purged solutions were added to the syringe using a luer adapter with needle, followed by the addition of the appropriate volume of packed RBCs to yield a 7% (v/v) solution. The syringe adapter was removed, and the syringe was inverted to mix the sample.

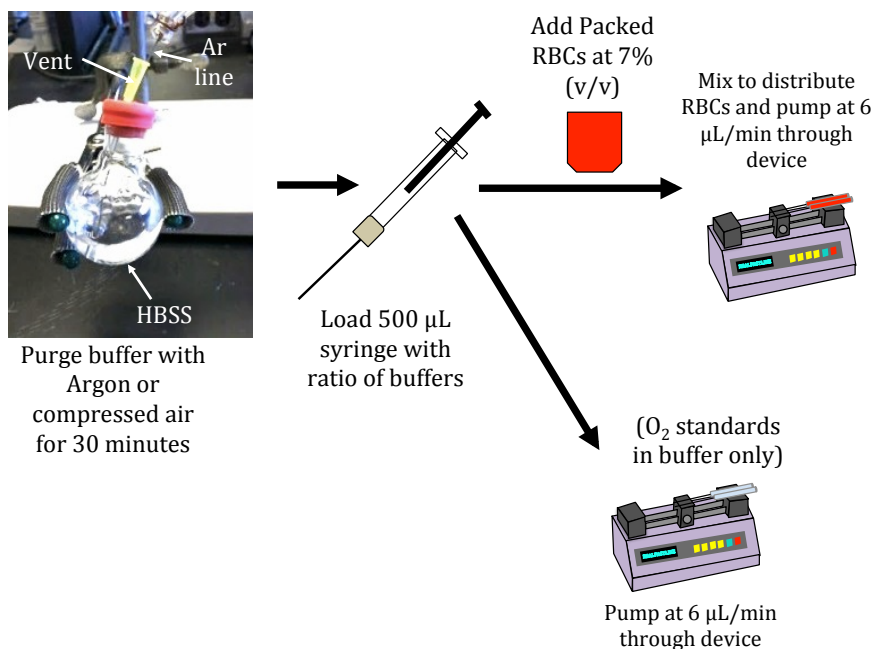


**Figure 3.4** Oxygen standard preparation. Volumes of air saturated and argon purged HBSS were drawn into a syringe to create the desired standard. Standards were pumped and chronoamperometric measurements were performed as described. RBC samples were made similarly by drawing up volumes of buffer and then a volume of RBCs to yield a 7% sample (v/v). The volume of RBCs was taken into account in the calculation of the standards, i.e., RBCs were taken to be air saturated and the required volume was accounted for in the air saturated volume of buffer. The sample was allowed to mix using inversion and rolling before pumping was started to ensure a homogenous solution of RBCs.

#### 3.5.4.1 NO Standards

A 1.9 mM NO stock solution was prepared by purging HBSS with Ar for 30 minutes and then purging for 30 minutes with NO gas (99.5%). Purification of the NO gas was accomplished by passing the gas from the cylinder through a KOH column to remove degradation products. Samples were prepared by mixing volumes of deoxygenated HBSS and NO purged HBSS in sealed, deoxygenated volumetric flasks.

### 3.5.5 Electrochemical Methods

#### 3.5.5.1 Voltammetric Measurements

A commercially available potentiostat (832b, CH Instruments, Austin, TX) was used in electrochemical measurements taken with the electrode shown in Figure 3.3. For voltammetric mea-

measurements, the scan rate used was 0.01 V/s unless otherwise specified. Calibration curves from voltammetric measurements were obtained by plotting the current at the identified maximum ( $i_p$ ) against the corresponding standard. An example oxygen cyclic voltammogram (CV) is shown below, and the regions of the curve are discussed.

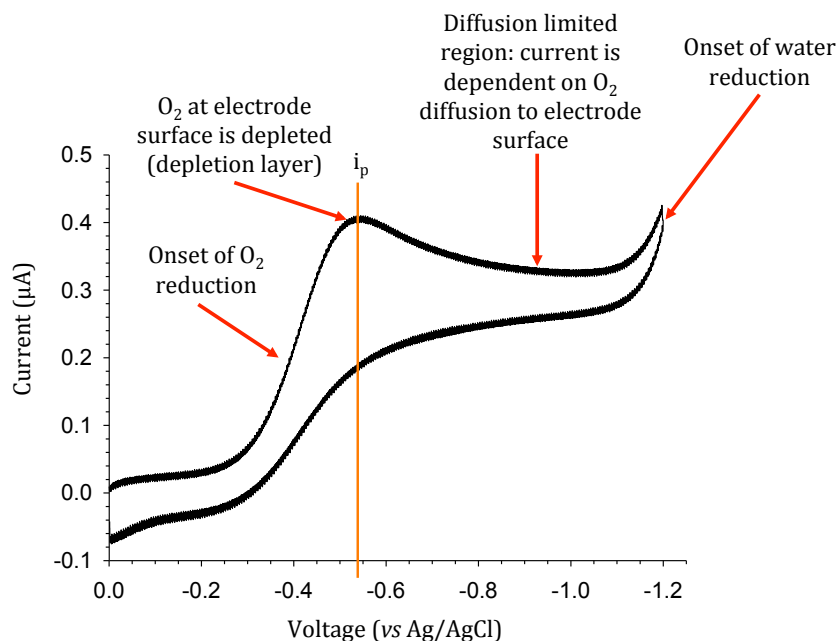


**Figure 3.5** A Representative cyclic voltammogram of an air purged solution. See Figure 3.8 for cyclic voltammograms from various oxygen standards.

In Figure 3.5, the scan begins at 0 V and proceeds to -1.1 V and then returns to 0 V. At approximately -0.3 V, the reduction of oxygen begins, and the current increases as a result. Oxygen at the electrode surface continues being reduced until the depletion layer is established (peak of the voltammogram). The corresponding current at the peak of the voltammogram is known as the peak current ( $i_p$ ), and in voltammetry, this value is plotted against concentration to generate calibration curves. After approximately -0.5 V, the observed current decreases, and the electrode is operating in the “diffusion-limited” regime. In the diffusion-limited regime, oxygen at the surface of the electrode has been depleted and now must diffuse to the electrode to be reduced, hence the term “diffusion-limited”. At voltages  $> -1$  V, the onset of water reduction can be observed. For pulsed amperometric methods (chronoamperometry), it is imperative to step to a voltage where the

analyte is reduced or oxidized (reduced for O<sub>2</sub>) and that the step is to a voltage where the reaction is diffusion-limited. For this example, the step could occur to -1 V. This is necessary because any other process that affects the current response either in a subtractive or additive manner can affect the calibration, e.g. onset of water reduction or stepping to a voltage before the depletion layer is established.

### **3.5.5.2 Chronoamperometric Measurements**

For chronoamperometric measurements of oxygen, the following parameters were used unless otherwise noted: initial V: 0 V; high V: 0 V; low V: -1 V; initial step polarity: negative; number of steps: 2; pulse width: 1 s; sample interval: 0.001 s; quiet time: 2 s; sensitivity (A/V):  $1 \times 10^{-5}$ . Calibration curves were obtained by plotting the value of the current at 0.3 seconds from the appropriate chronoamperogram against the corresponding oxygen standard concentration.

### **3.5.5.3 Flow Injection Analysis**

To facilitate injection of NO standards into the fluidic device shown in Figure 3.14, a 4-port rotary injection valve (VICI Rotor, Valco Instruments, Houston, TX) was interfaced to a syringe pump (Harvard 11 Plus, Harvard Apparatus, Holliston, MA) and a 500  $\mu$ L syringe (SGE Analytical Science, Austin, TX) to provide continuous flow of buffer through the device at 8  $\mu$ L/min. The syringe, rotor, and device were connected using 150  $\mu$ m i.d. capillary bore tubing with 350  $\mu$ m i.d. tube sleeves, finger tight PEEK fittings, and luer adapters (Upchurch Scientific, Oak Harbor, WA). The Pt-black/Pt electrode assembly shown in Figure 3.14 was screwed into the device's threaded port, and as pictured, the electrodes were aligned in the channel in a serial manner. Flow was directed so that the sample stream crossed the working electrode first. Injection volume for the VICI rotor was 200 nL, and amperometric detection was performed by biasing the Pt-black working electrode at +0.90 V vs. Pt using a commercial potentiostat (832b, CH Instruments, Austin, TX).

## 3.6 Results and Discussion

### 3.6.1 Validation of Oxygen Electrode Using Electrochemical Methods

When an electrode is fabricated, it is typical to characterize and confirm electrode performance using a well-known electrochemical couple, such as ferricyanide/ferrocyanide. The electrode performance was investigated using this couple, and from the results, it was confirmed that the electrode fabrication was successful. Validation using potassium ferricyanide was performed using the bare electrode fabricated in Figure 3.6, i.e., bare electrodes with no Nafion coating. After the performance of the electrode was confirmed using the example system, measurements of oxygen standards and RBC samples using the Nafion-coated electrode were performed.

### 3.6.2 Validation of Oxygen Electrode Using Potassium Ferricyanide

Potassium ferricyanide standards were prepared from a 5 mM stock solution in 0.5 M sodium sulfate. Using a prototype of the device in Figure 3.2, standards were pumped through the channel, and voltammograms were obtained using the parameters described in the Voltammetric Methods section. The prototype device contained a threaded electrode port, inlet, and outlet, and the channel dimensions were identical to the device in Figure 3.2.

From the voltammograms in Figure 3.6, it can be observed that the signal from the reduction peak (forward scan) grows larger in magnitude as the concentration of ferricyanide increases, as expected.  $I_p$  was identified for each standard using the CH Instruments peak picking software and was plotted against the corresponding concentration, as shown in the plot to the right. To confirm that the system was reversible as anticipated, the scan rate was varied and the two calibrations were compared. Because  $i_p$  varies proportionally with the square root of the scan rate ( $\nu$ ), the peak currents for the 100 ms curves should be approximately 3 times higher than the peak currents of the corresponding standard obtained using a 10 ms scan rate. The system is not completely reversible, as it is noted that the voltage at which  $i_p$  occurs does shift based on concentration.

Ferricyanide was also detected chronoamperometrically, as shown in Figure 3.7, while flowing

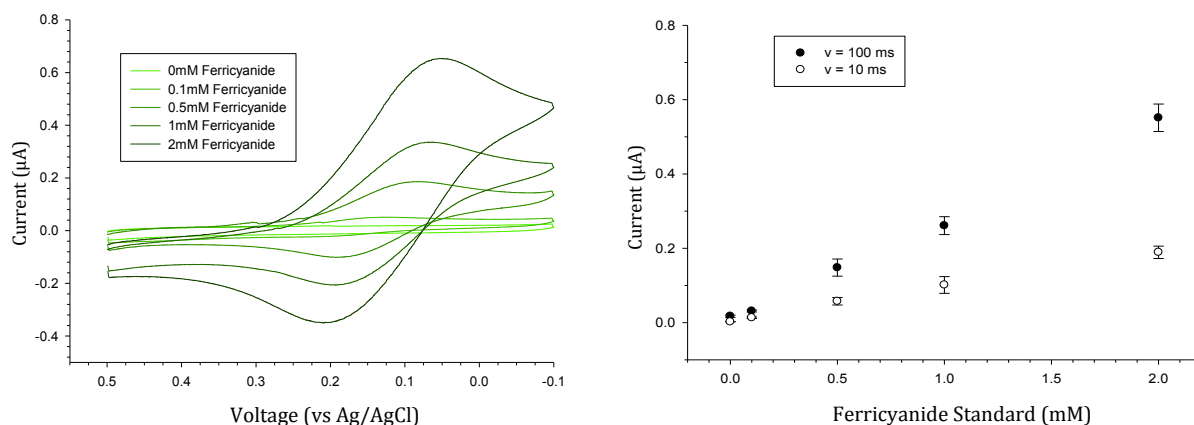


**Figure 3.6** (Left) Voltammetric detection of ferricyanide using bare Au and Ag/AgCl electrodes. The voltage was scanned at 0.1 V/s from 0.5 V to -0.1 V to obtain cyclic voltammograms of ferricyanide standards flowing through the prototype 3D printed device similar to the device in Figure 3.2. As the ferricyanide concentration increases, the intensity of the reduction peak of ferricyanide becomes larger. Plotting the peak current against the corresponding ferricyanide standard yields a calibration curve, indicating that the electrode system functions as anticipated. (Right) Calibration curves were obtained by plotting  $i_p$  of each cyclic voltammogram against the corresponding standard concentration.  $N = 3$  electrodes. Error = STD.

standards across the same bare electrode at 6  $\mu\text{L}/\text{min}$  in the prototype device. When the current at 0.3 seconds was plotted against the corresponding concentration, a linear relationship was observed. This suggests that amperometric detection with this set of electrodes is feasible.

### 3.6.3 Validation Using Oxygen Standards with and without RBCs

Oxygen standards were prepared as described above and as shown in Figure 3.4. Standards were prepared in the physiologically relevant concentrations ranging from air saturated samples to anoxic samples. Cyclic voltammograms of flowing standards were obtained and the current was plotted in Figure 3.8. The magnitude of the peak current increases with increasing concentration of oxygen, up to the air saturated sample (8.74 ppm). However, voltammetry was not used for calibration because of variability in the peak shapes in the relevant voltage ranges, which is likely due to the variable method of oxygen reduction at the electrode surface. The oxygen reaction highlighted in Figure 3.8 can form hydrogen peroxide as an intermediate, and the reaction may not always go to completion. Because of the variability in peak shape and height of the voltammograms, mea-

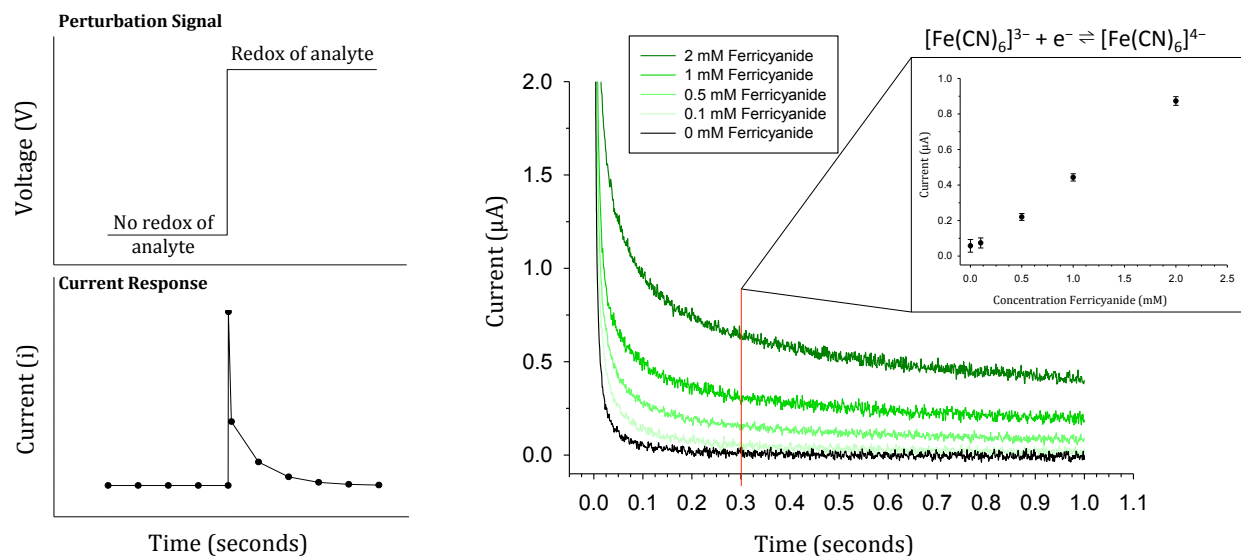


**Figure 3.7** (Left) Example of chronoamperometric perturbation signal and corresponding current response. The voltage of the working electrode is stepped from a voltage where no or minimal redox of the analyte occurs to a voltage where redox of the analyte occurs and is diffusion limited (see Figure 3.5). The corresponding current response (bottom left) begins at the same time the voltage is stepped and the response takes the form of an exponential decay. The bare Au and Ag/AgCl electrode from Figure 3.3 was used to chronoamperometrically detect ferricyanide standards flowing through a 3D printed device. (Right) Current responses to the pulsed chronoamperometric reduction of ferricyanide to ferrocyanide ( $E^\circ = 0.361 \text{ V}$ ) are shown in the above plot. The voltage was stepped from  $+0.2 \text{ V}$  to  $-0.3 \text{ V}$ , and the current was measured using a commercial potentiostat. Plotting the current value at 0.3 seconds from each chronoamperogram against its corresponding concentration yields a linear calibration curve.  $N = 3$  electrodes. Error = STD.

asuring the current in the diffusion-limited regime using a pulsed technique (chronoamperometry) was used to calibrate the oxygen standards. In addition, the chronoamperometric pulsed technique allows the experimentalist to collect data faster, without any observable negative impact on data quality.

From the chronoamperograms of oxygen standards, the current at various time points in each decay curve (0.05, 0.1, 0.3 seconds) was plotted against the corresponding concentrations, and the resulting linear relationship is shown in Figure 3.9. Note that the curve plotted from the current signal at 0.05 seconds is more sensitive (larger slope) but that the corresponding background current is larger than the background of the curves from the two other time points. This is due to the increased presence of charging current at earlier times in the decay profile. The calibration from 0.3 seconds was chosen because of the low background, sufficient sensitivity to measure prepared



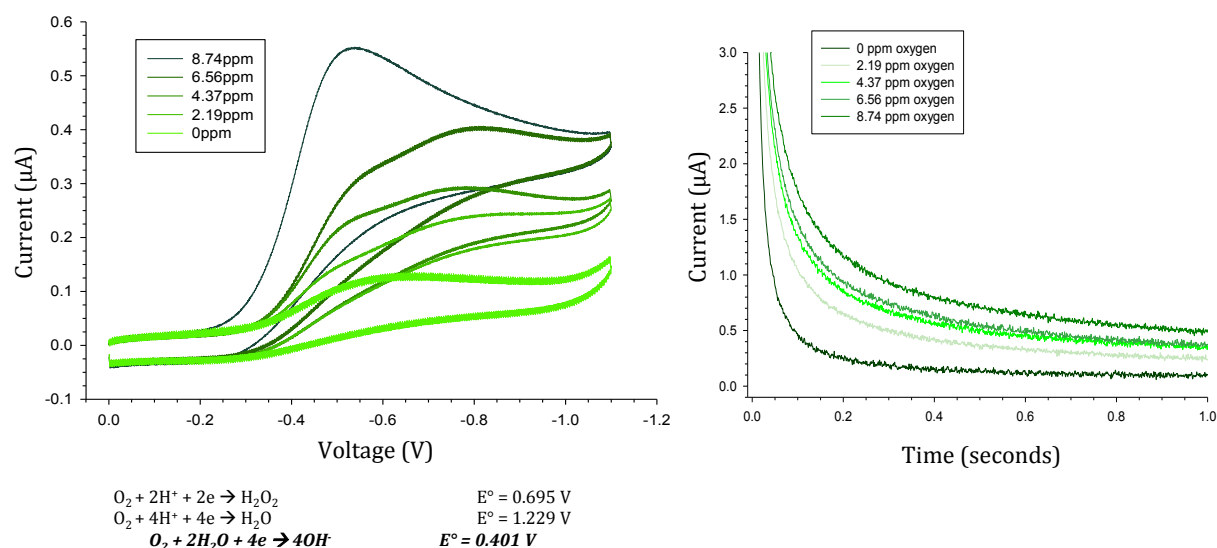


**Figure 3.8** Cyclic voltammograms of flowing oxygen standards. Oxygen standards were prepared as described and as shown in Figure 3.4 and were flowed through a prototype of the device shown in Figure 3.2. The electrode, coated with 2.5% Nafion, described in Figure 3.3 was used in the measurement. The voltage was scanned at 0.1 V/s from 0 V to -1.1 V. The resulting voltammograms from various concentrations of ferricyanide are plotted above. The reduction of oxygen occurs at around -0.4 V. Other reactions for reduction of oxygen at the electrode surface are typically performed under acidic conditions, and as the pH of buffers used in these experiments is 7.4, the bolded reaction above is likely occurring at the working electrode surface. Since the peak currents are difficult to identify, likely due to the variability in the actual oxygen reduction mechanism at the electrode surface, voltammetry was not used to calibrate the electrode for experiments with RBCs.

oxygen standards, and the low magnitude of current applied to cells relative to other time points.

### 3.6.4 Measuring Oxygen Tension in Hypoxic RBC Samples

The oxygen tension in RBC samples was determined by using the calibration curve generated from buffer standards. RBC samples were prepared as shown in Figure 3.10, and the current values at 0.3 s in the amperometric decay profiles from each sample were within the range of buffer calibration data as expected, allowing determination of the oxygen content in each sample. It is important to note that while there is relative control over the oxygen tension in the RBC samples, the control is not absolute. For example, when the “air-saturated” RBC sample is made, the calculated oxygen tension of 8.74 ppm does not agree with the measured tension of about 7 ppm. This discrepancy is likely due to the packed RBCs not being air saturated, since they are not purged with compressed

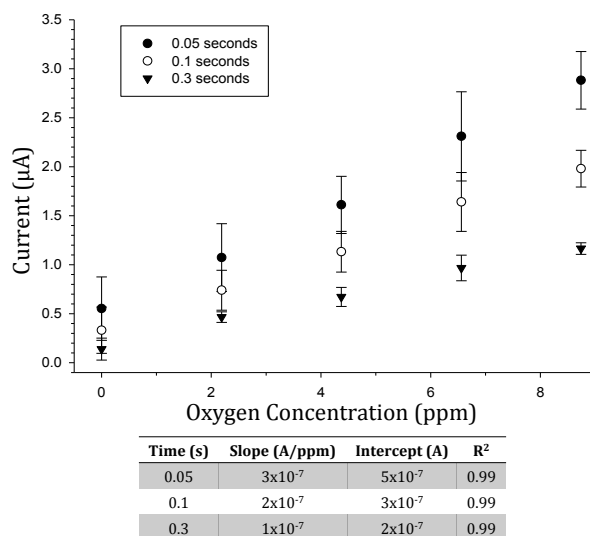


**Figure 3.9** Calibration curves generated by the chronoamperometric detection of flowing oxygen standards. Samples were prepared as described in Figure 3.4 and were flowed through the device in Figure 3.2 at 6  $\mu\text{L}/\text{min}$ . The potential was stepped from 0 V to -1 V using the Nafion coated electrode show in Figure 3.3, and the current value at various times were plotted against the concentration of oxygen in the sample. From the linear fits obtained from each curve, it can be shown that using calibration values earlier in the chronoamperometric current decay result in a more sensitive measurement (comparing the slopes in the table). However, this compromises the low background that is observed when using current values at 0.3 seconds. N = 3 electrodes. Error = STD.

air as is done with the buffer. This results in currents that are lower than the signals from the standards as the desired oxygen tension is effectively diluted. This trend however, reverses at some point between the 2.19 ppm standard and the 0 ppm standard, where the oxygen present in the red cell sample (dissolved oxygen *and* oxygen bound to Hb) contributes to the signal.

Nonetheless, the RBC samples can be systematically deoxygenated by decreasing the oxygen in the sample using methods described in Figure 3.10. The absolute amount of the oxygen in the sample is not the primary concern (dissolved  $\text{O}_2$  and  $\text{O}_2$  carried by Hb), as the oxygen tension can be measured and quantified. The current values in Figure 3.9 differ from those of the buffer standards because of the equilibrium between dissolved  $\text{O}_2$  and  $\text{O}_2$  bound to Hb, which is dictated by the established sigmoidal relationship between the two.

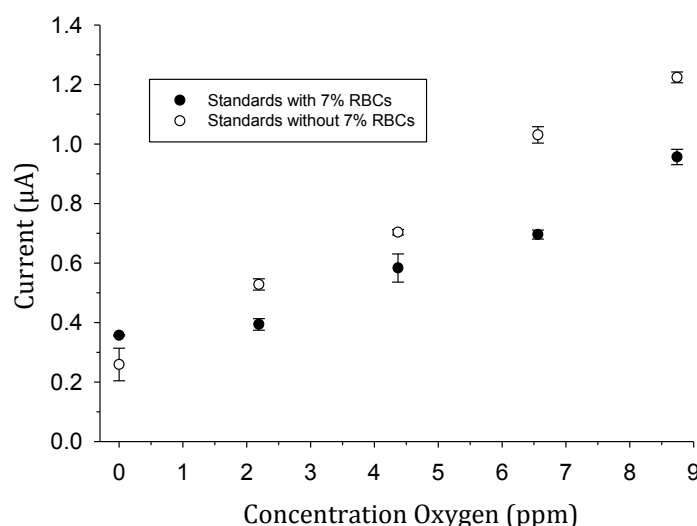


**Figure 3.10** Calibration curves for oxygenated standards with or without RBCs. The sensitivity of the curve decreases and the background increases when RBCs are incorporated into the flowing sample: buffer only ( $y = 1.13 \times 10^{-7} + 1.26 \times 10^{-7}$ ;  $R^2 = 0.98$ ) and for buffer + RBCs ( $y = 8.15 \times 10^{-8} + 2.50 \times 10^{-7}$ ;  $R^2 = 0.93$ ).  $N = 1$  electrode with triplicate measurement. Error = STD.

### 3.6.5 Measuring ATP Release from Hypoxic RBC Samples in a 3D Printed Device

ATP release from flowing hypoxic RBCs was measured using the luciferin-luciferase assay in a similar manner to the protocol described in Chapter 2. RBC samples were pumped at 6  $\mu\text{L}/\text{min}$  for 30 minutes. The pump was stopped, and because the device was not plate reader compatible, the sample was transferred from the well insert to an Eppendorf tube and kept on ice. Once samples were collected, they were transferred to a 96-well plate, LL was added to wells, and the chemiluminescence was measured using a commercial plate reader. As shown in Figure 3.11, the ATP release from a hypoxic sample ( $4.76 \pm 0.53$  ppm  $\text{O}_2$ ) of RBCs flowing through a 3D printed device released on average  $2.38 \pm 0.28$  times more ATP compared to a normoxic control ( $8.22 \pm 0.60$  ppm  $\text{O}_2$ ).

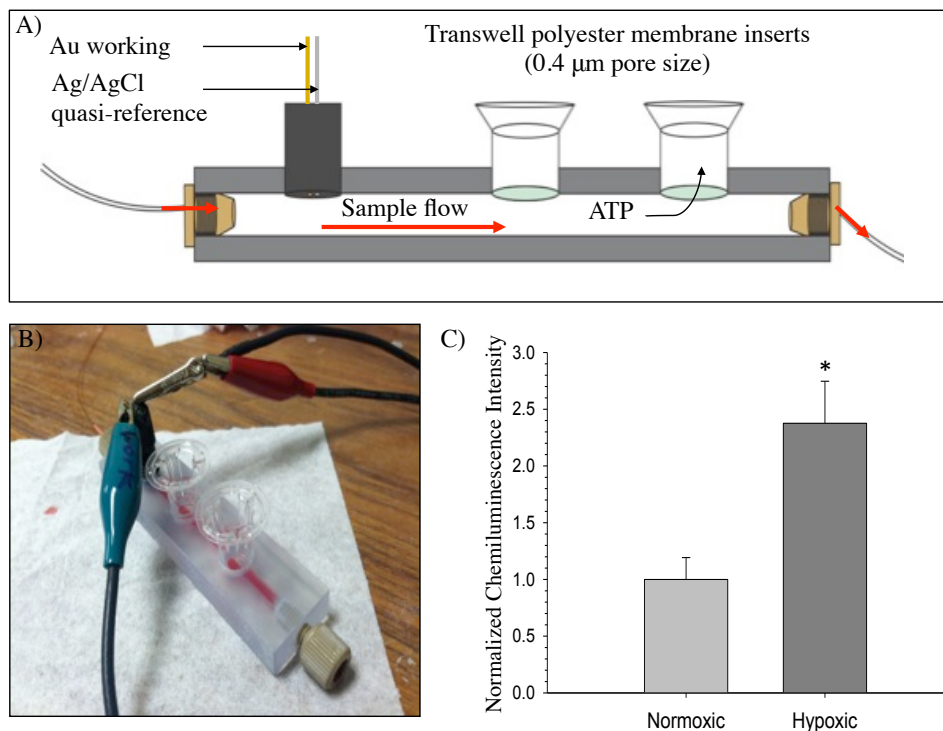


**Figure 3.11** Measuring hypoxic RBC samples on a 3D printed device. (A) Cross section of the device shown in Figure 3.2 details the path of the flowing sample and the fate of ATP released from RBCs. The sample can be pumped through the device, and ATP released from RBCs can diffuse across the porous, polyester membrane of the transwell inserts to be detected offline using luciferin-luciferase. The electrodes described in Figure 3.3 can be screwed into the threaded port of the device to measure the oxygen tension of the flowing sample. B) Image of the device in action. The RBCs can be seen in red flowing through the device while the set of electrodes is connected to the potentiostat from the leads with alligator clips. C) When a hypoxic sample of RBCs ( $4.76 \pm 0.53$  ppm O<sub>2</sub>) is flowed through the device, the RBCs release approximately  $2.38 \pm 0.28$  times more ATP compared to a normoxic control ( $5.66 \pm 0.6$  ppm O<sub>2</sub>). N = 3 donors. Error = S.E.M. \*p < 0.05.

### 3.6.6 Correlating RBC ATP Release with Oxygen Tension

Using the sample preparation method described in 3.4, RBC ATP release was observed to increase with decreasing oxygen tension (see Figure 3.12). The bi-directional error bars on each data point were assigned based on the S.E.M. of the oxygen measurement and S.E.M. of the ATP release measurement. This is due to the variability among human donor ATP release that can increase sample variance and also the differences in P<sub>50</sub> between donors, which has been documented in the literature.<sup>181–185</sup> The increase in ATP release is not due to lysis, as the increase can be inhibited by incubating RBCs with 100 μM of the cell stiffening agent diamide prior to making the samples

as shown in Figure 3.4. This implicates cell deformability in the mechanism of hypoxic ATP release.

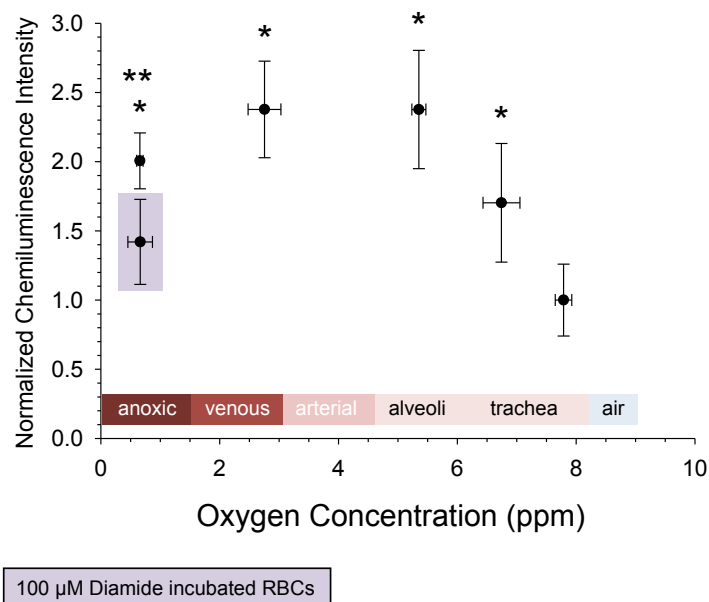


**Figure 3.12** RBC ATP Release in Response to Decreasing Oxygen Tension. The RBC ATP release, which is directly proportional to chemiluminescence intensity, increases as oxygen tension is lowered systematically. It is important to note that the release appears to saturate at  $O_2$  tensions below about 5 ppm  $O_2$ . Relative to the normoxic control ( $7.79 \pm 0.14$  ppm  $O_2$ ), RBCs release on average  $1.70 \pm 0.43$  ( $6.74 \pm 0.31$  ppm  $O_2$ ),  $2.38 \pm 0.43$  ( $5.35 \pm 0.12$  ppm  $O_2$ ),  $2.38 \pm 0.35$  ( $2.75 \pm 0.28$  ppm  $O_2$ ),  $2.01 \pm 0.20$  ( $0.66 \pm 0.05$  ppm  $O_2$ ) fold more ATP when exposed to the corresponding oxygen tension. When 7% RBCs are incubated with 100  $\mu$ M diamide prior to reconstitution in anoxic buffer at 7%, the ATP release is significantly lower compared to other hypoxic samples,  $1.42 \pm 0.31$  ( $0.66 \pm 0.21$  ppm  $O_2$ ) (\*\* $p < 0.005$ ).  $N \geq 3$  donors and error = S.E.M. \* $p < 0.05$ .

The nonlinearity of the response, specifically its sigmoidal shape, suggests that ATP release from the RBC is related to Hb saturation. Several pieces of evidence exist in the literature that suggest this could be plausible, specifically Band 3's hypothesized role in RBC ATP release, as well as the evidence for the transmembrane protein's direct binding to deoxygenated Hb. Using experimental data and some assumptions, the relationship between Hb saturation, directly related to the number of deoxygenated heme, and ATP release can be estimated using the original equation proposed by Severinghaus<sup>36</sup> and plotted against each other, as seen in Figure 3.13. The error in the fit equation used to convert between the two parameters is at maximum 0.5%<sup>36</sup> and was added onto the reported S.E.M. for each point.

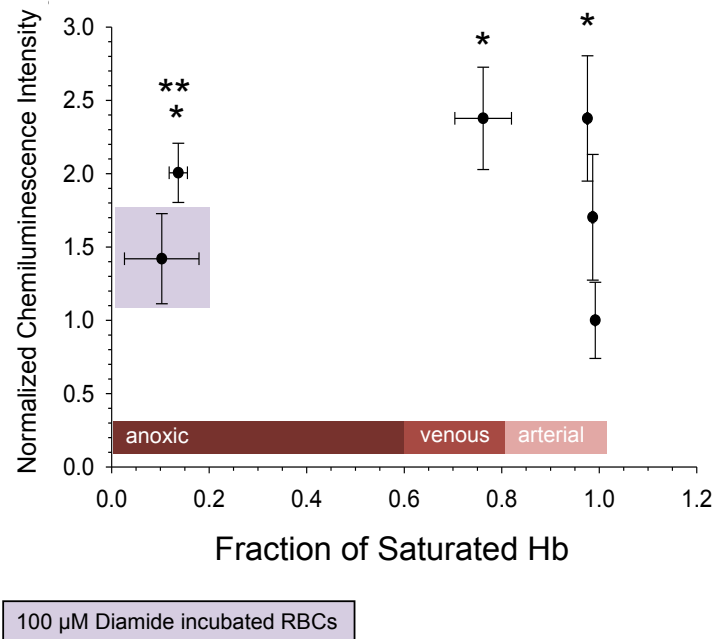


**Figure 3.13** RBC ATP Release in Response to Decreasing Oxygen Tension Plotted as a Function of Hb Saturation. The RBC ATP release, which is directly proportional to chemiluminescence intensity, increases as oxygen tension is lowered systematically. Hb saturations were calculated using the equation developed by Severinghaus, presented in Chapter 1. All Hb saturations are significantly different from the 8.74 ppm control sample (\* $p < 0.001$ ), except for the most hypoxic RBC sample and its corresponding RBC sample that was incubated with 100  $\mu\text{M}$  diamide (purple box).  $N \geq 3$  donors and error = S.E.M

Figure 3.13 indicates that ATP release is correlated with the conformation of heme in the RBC, providing evidence to support the hypothesis that heme is directly involved in the mechanism of hypoxic ATP release. The Hb saturation values were calculated from measured  $\text{PO}_2$  values from the equation in Chapter 1. The rapid increase in ATP release within the first 10% of desaturation of Hb can be explained by considering *in vivo* oxygen tensions. In the lungs, where Hb binds  $\text{O}_2$  for distribution to peripheral tissue, the oxygen tension ( $\text{PO}_2$ ) is approximately 100 mmHg, which corresponds to a Hb saturation value ( $\text{SO}_2$ ) of approximately 97%. Arterial blood and mixed venous blood contain 100 mmHg ( $\text{SO}_2 = 97\%$ ) and 40 mmHg oxygen ( $\text{SO}_2 = 80\%$ ), respectively. This means that a ( $\text{PO}_2$ ) of 0 mmHg would be super physical.<sup>1-4</sup> The data in Figure 3.13 suggest that a maximum ATP release occurs at some Hb saturation between 80%, which corresponds to

approximately 40 mmHg, and 100%, i.e., the ATP release mechanism is highly sensitive to changes in  $O_2$  tension that are known to occur in the bloodstream. This makes sense because if the RBC ATP release mechanism were insensitive to changes in  $PO_2$  in the physiologically relevant ranges, one would anticipate this would be problematic. If the mechanism were sensitive in a different region of oxygen tensions, this might point to an evolutionary difference, e.g., animals that contain myoglobin would be expected to have a different ATP release profile, provided they release ATP. On the other hand, it might be interesting to examine the ATP release profiles of patient populations that are established to exhibit altered ATP release (type II diabetics). It is known that these patients exhibit problems with blood flow, and it would be expected that their release profile would differ, especially in cases where RBC deformability is compromised, e.g., type II diabetics and stored RBCs.

It is important to keep in mind that the data in Figure 3.12 and Figure 3.13 show the result of varying oxygen tension in a 7% RBC sample. A healthy human has a hematocrit between 45-50%, which depends on sex, and the circulating hematocrit *in vivo* varies depending on the point in circulation<sup>11,13,186</sup> and can reach single digit values in the microcirculation.<sup>18</sup>

### **3.7 Measuring NO Release Released From Hypoxic RBCs**

It was hypothesized that RBC-derived NO would also increase with systematic decreases in oxygen tension, and the following section presents several tools to measure released NO in a flowing sample of hypoxic RBCs. The first is a 3D printed device having 0.5 mm x 0.5 mm channels and a threaded port for an electrode. The electrode consisted of a Pt-black black working and Pt reference and was fabricated in the same manner as the electrode in Figure 3.3. The second device was fabricated from hybrid materials (PDMS and epoxy). A glassy carbon electrode, platinized to enhance NO detection, was embedded in an epoxy base. Also embedded in the epoxy base were multiple gold wires which could be fabricated into gold pillars using deposition techniques.<sup>7</sup> The gold pillars functioned as a barrier between two PDMS channels through which hypoxic RBCs were pumped. The released NO could diffuse across the gold pillar barrier to the detection elec-

trodes downstream.

### 3.7.1 NO Detection Using a Pt-black Electrode Integrated with a 3D Printed Microfluidic Device

In collaboration with the Martin Lab at Saint Louis University, platinized electrodes were used to demonstrate measurement of NO, a radical molecule with a half life of 1-2 seconds.<sup>67,68</sup> Bare platinum has been utilized for the same purpose; however, with a platinized electrode (termed Pt-black) the sensitivity of the system to NO has been demonstrated to significantly increase by 8-13 fold.<sup>6,7,187,188</sup> Using a 3D printed device with 0.5 mm x 0.5 mm channels (shown below in Figure 3.14) and a flow injection system described in the methods section, we were able to demonstrate measurement of NO standards prepared as described in the methods section.

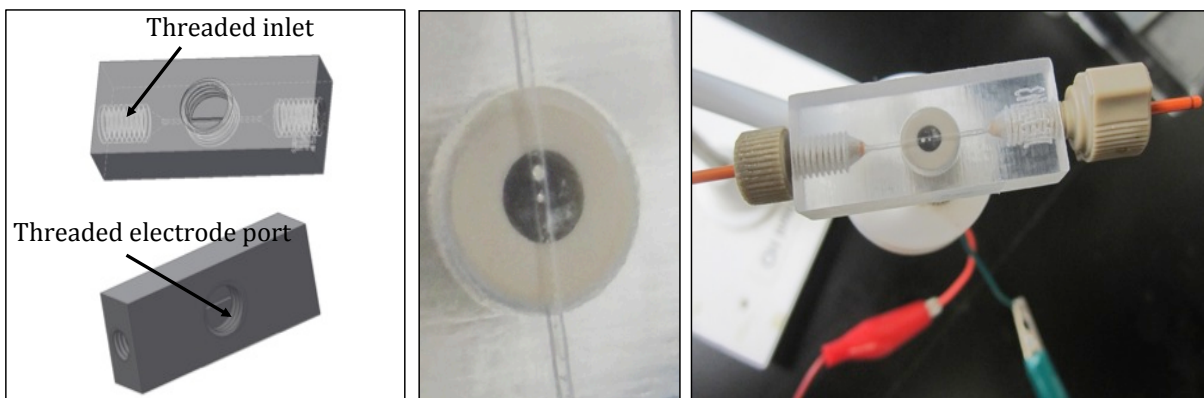


**Figure 3.14** 3D printed device used in characterization of Pt electrodes used for NO detection.<sup>6</sup> The part file of the device details the threaded inlet/outlet and the threaded port for the electrode (left). The alignment of the electrode when tightened into the threaded port is shown in the middle panel, with the Pt working and reference electrodes serially aligned in the square shaped channel (500  $\mu\text{m}$  x 500  $\mu\text{m}$ ). The electrode-device assembly is shown in the right panel with the connection to potentiostat leads and integration of capillary tubing.

From Figure 3.15, the average peak height from replicate injections of 190  $\mu\text{M}$  NO observed on Pt-black electrodes was  $3.61 \pm 0.02$  nA ( $N = 3$ ) compared to  $0.54 \pm 0.06$  nA ( $N = 3$ ) on a bare Pt electrode, which is nearly a 7-fold increase. The variation in peak areas was 4.2% (RSD,  $N = 12$ ) with an average peak height of  $2.63 \pm 0.11$  nA ( $N = 12$ ). The limit of detection was 1  $\mu\text{M}$  and



a linear relationship ( $R^2 = 0.99$ ) was observed for NO concentrations ranging from 7.6  $\mu\text{M}$  to 190  $\mu\text{M}$ .

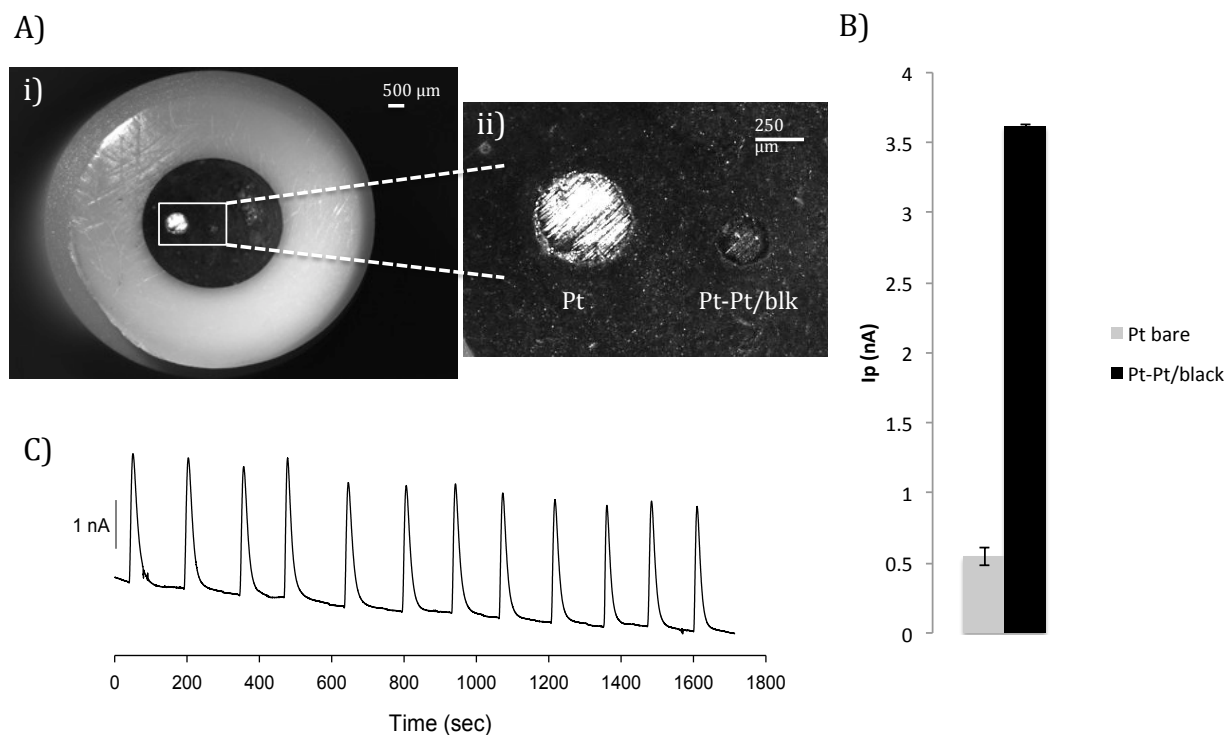


**Figure 3.15** Detection of NO using a Pt-black electrode integrated with a 3D printed device.<sup>6</sup> Using the electrode shown above in (A) and the device shown in Figure 3.14, injections of 200 nL plugs of NO standard (190  $\mu\text{M}$ ) were made, and NO was detected either using bare Pt or Pt-black coated working electrode vs. a Pt quasi-reference electrode. Average peak height (B) for NO detected with Pt-black was  $3.61 \pm 0.02$  nA relative to peak heights obtained with bare Pt ( $0.54 \pm 0.06$  nA). Repeated injections of 200 nL plugs of NO standard (190  $\mu\text{M}$ ) were made over the Pt-black electrode to show the reproducibility of the system, shown in (C).  $N = 3$ . Error = STD.

### 3.7.2 NO Measurements Using Pt-black Modified Glassy Carbon Electrodes Integrated with a Planar Soft Polymer Microfluidic Device

Hypoxia-induced RBC NO was measured on a planar, polymer microfluidic device using a Pt-black modified glassy carbon working electrode and Ag/AgCl reference coated with 0.05% Nafion. The device consisted of two channels, separated by a gold pillar array. The pillar barrier allowed cells to be pumped through one channel without crossing over into the adjacent channel. NO released from the RBC samples could diffuse across the array into the detection channel, which

had a higher flow rate relative to the sample channel, allowing the RBC NO to be transported to the Pt-black/glassy carbon electrode for detection. A schematic of this setup is shown below in Figure 3.16.

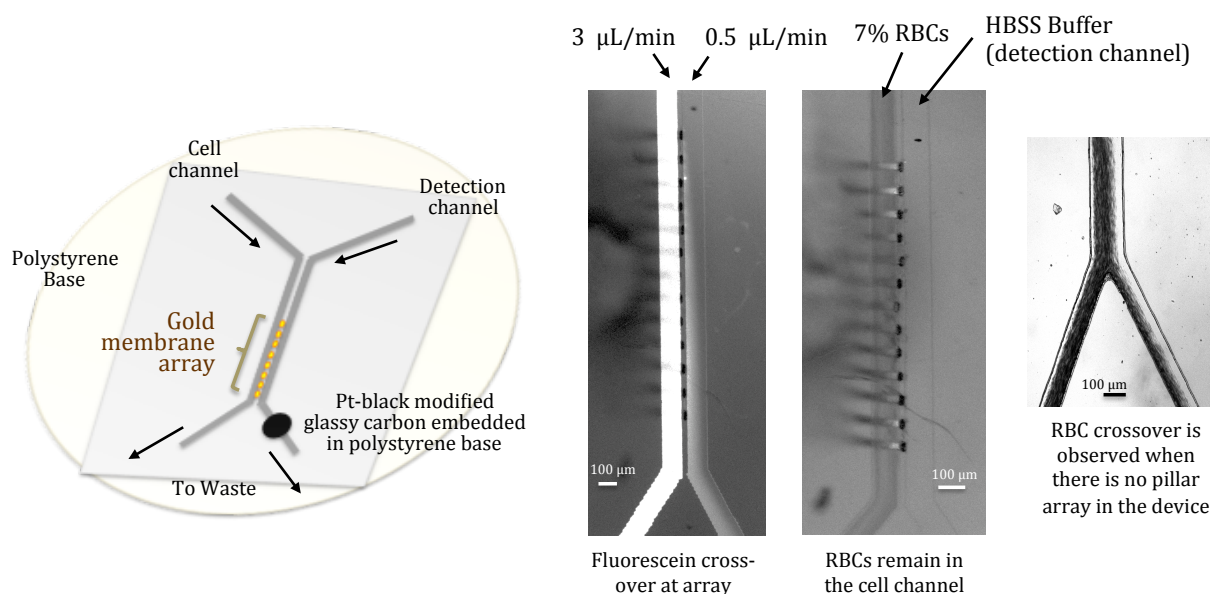


**Figure 3.16** Pt-black modified glassy carbon detection system for measuring hypoxia-induced RBC NO.<sup>7</sup> The double layer device consists of a glassy carbon electrode embedded into a polystyrene base. The gold pillar array is fabricated using deposition methods directly onto gold wires embedded into the polystyrene base. The polymer layer consists of two microfluidic channels 400  $\mu\text{m}$  in width separated by a 50  $\mu\text{m}$  space to accommodate the gold pillars.

NO standards and RBC samples were prepared as described. Briefly, Oxyrase was added to HBSS and purified RBCs were added to yield a 7% solution of RBCs with 10% v/v oxyrase. RBC samples were incubated with 100  $\mu$ M L-NAME prior to oxyrase addition to inhibit RBC NOS. Samples were allowed to incubate for at least 30 minutes. Samples were loaded into a 500  $\mu$ L syringe, and using the flow injection system, 200 nL of sample were injected, followed by detection of the released NO in the adjacent flowing stream of buffer. This allowed electrochemical NO detection without RBCs in the sample. The ability to detect small molecules, such as NO, in the detection channel was confirmed by using fluorescein to visualize diffusion across the pillar array. From the image in Figure 3.16, it was demonstrated that fluorescein can diffuse across the gold pillar array into the adjacent channel, therefore, it was accepted that NO would also be able to cross the pillar barrier for subsequent detection.

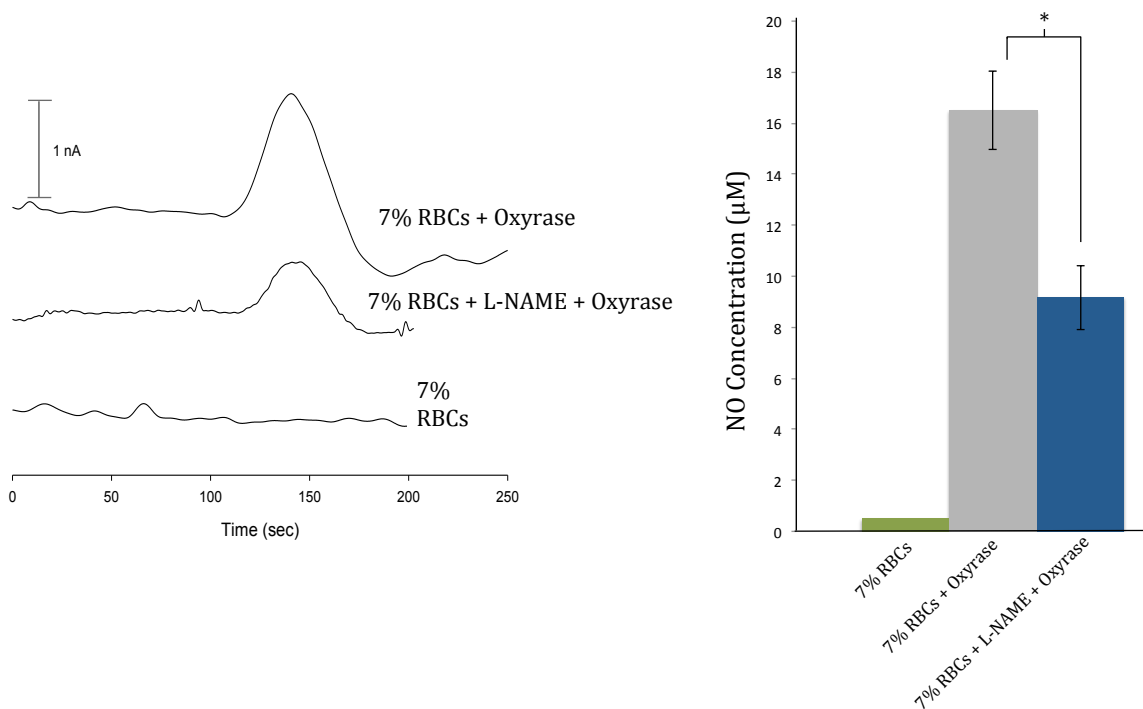


**Figure 3.17** NO release from hypoxic RBCs.<sup>7</sup> (Left) Amperogram overlay of signals from normoxic 7% RBCs, RBCs with inhibited NO release using L-NAME, and hypoxic RBCs. Peak areas were calculated using the peak picking software in CH Instruments. Quantity of NO detected was calculated using the peak areas from standards. (Right) NO release from 3 RBC donors (N = 3, Error = S.E.M, \*  $p < 0.05$ ).

The amount of NO detected from 7% RBCs incubated with oxyrase was  $16.5 \pm 1.5 \mu\text{M}$  NO compared to the normoxic sample. When the RBCs were incubated with L-NAME for 30 minutes and then made hypoxic by adding oxyrase, the RBCs released on average  $9.2 \pm 1.3 \mu\text{M}$  NO. The amount of detected NO electrochemically is higher than previous fluorescence studies conducted by our group,<sup>34,49</sup> in which hypoxic RBCs released approximately  $7 \mu\text{M}$  NO. This difference (approximately 2-fold) is likely due to the differences in calibration and detection methods (fluorescent probe with NONOates versus NO gas calibration). The NO gas calibrations used in the measurements above are more straightforward to use in terms of calibration, as one can use solubility coefficients to calculate stock NO solutions. Calibration with NONOates is difficult as the kinetics of donor release of NO should be confirmed prior to use in experiments. One way to resolve this issue between the two methods would be to electrochemically detect NO produced by NO donors for comparison to purged NO stock solution signals.

### **3.8 Conclusions and Future Work**

#### **3.8.1 Mechanism of Hypoxic ATP Release**

The above data, specifically Figure 3.13 and Figure 3.12, suggest that ATP release from RBCs is proportional to the percent of desaturated Hb, i.e. ATP release increases and saturates with decreasing Hb saturation. Hypoxia-induced ATP release can be inhibited by incubating the RBCs with  $100 \mu\text{M}$  diamide prior to subjecting them to a hypoxic environment. Diamide, a well-known oxidant, can oxidize proteins such as spectrin on the RBC membrane, rendering the cell less deformable.<sup>132</sup> One study to strengthen the case presented above for Hb-mediated ATP release would require incubation of RBCs with the AE1 (Band 3) inhibitor 4,4'-diisothiocyanatostilbene-2,2'-disulfonic acid (DIDS) prior to measuring ATP release. DIDS is known to disrupt the binding that occurs between Hb and the N-terminus of the cytoplasmic domain of Band 3 (cdb3) by binding to external sites (Lys539 and Lys542).<sup>189–191</sup>

### 3.8.2 Mechanism of Hypoxic Vasodilation

It was observed that a 7% solution of hypoxic RBCs releases approximately 2-fold more ATP relative to a normoxic control, which supports the hypothesis that the RBC can be a mediator in vessel dilation *in vivo* via activation of the P<sub>2</sub>Y receptors on the endothelial cell surface to induce NO release. As demonstrated in Chapter 2 using microfluidic devices, stimulated RBCs release an increased amount of ATP relative to controls, and that ATP can diffuse to an adjacent, cultured endothelial layer to induce a change in NO release, implicating the RBC as a mediator of vessel dilation.<sup>5</sup> Future experiments with the device from Figure 3.2 should probe the interaction of hypoxic RBCs with endothelial cells to measure NO release. This can be accomplished by culturing bPAECs in the transwell inserts, as has been demonstrated in conjunction with a 3D printed device,<sup>192</sup> to confirm ATP-mediated NO release from bPAECs, as was demonstrated in Chapter 2.<sup>5</sup>

### 3.8.3 Correlating RBC NO Release with Oxygen Tension for Stored Blood Applications

Preliminary results from RBC NO release suggest that a similar trend as observed with hypoxic ATP release may exist. The RBC NO release, measured using 10  $\mu$ M of the extracellular probe DAF-FM, increases by a factor of 6-7 when the oxygen tension is decreased from normoxic (1.3  $\mu$ M NO released) to hypoxic conditions (7-9  $\mu$ M NO released). RBCs were collected into modified storage solutions and subsequently the RBCs were isolated based on previous protocols developed by the Spence lab.<sup>193</sup> RBCs were stored in AS1 which contains approximately 60 mM glucose. Another set of RBCs was stored in a modified storage solution (AS1N) containing 5 mM of glucose.

However, it is not clear if the NO levels saturate as was observed with hypoxic RBC ATP release. After 4 weeks of storage in approved (Additive solution 1 (AS1), high glucose) and modified storage solutions (AS1N, low glucose or normal glucose levels), the hypoxia-induced NO release from the RBCs does not appear to have significantly changed, but again, this experiment must be repeated to conclude anything concretely. One issue with the protocol for these experiments is that

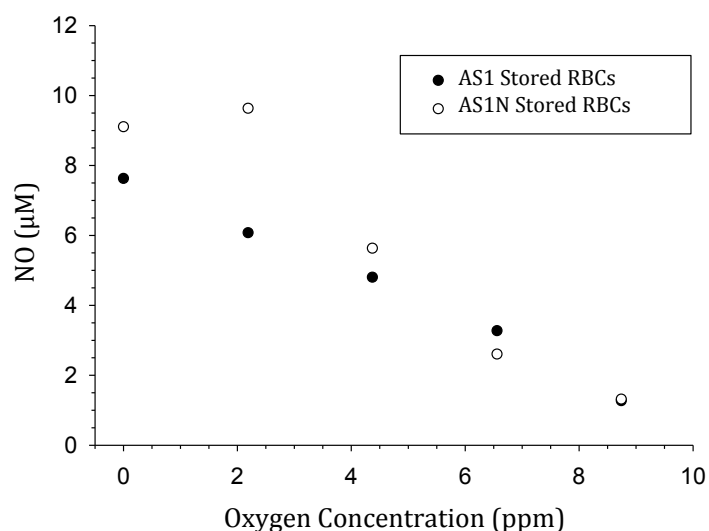


**Figure 3.18** NO Release from Stored RBCs Measured Using the Fluorescent Probe DAF-FM. These cells were fed once a week for up to four weeks. The data above is from an RBC sample stored for 4 weeks. Lysis was under 1% and glucose levels were maintained at around 5.5mM in the AS1N samples with feeding (data not shown).

of lysis. Even though the % lysis was below 1% for storage conditions, RBCs were not washed prior to measurement in early studies. Free hemoglobin resulting from lysis can oxidize NO to nitrate/nitrite, and thus quantities of NO released from stored RBCs could have been observed to be lower than with other results obtained from fresh RBCs.<sup>7</sup>

### 3.8.4 High Throughput Potential

A high throughput version of the oxygen device is shown in Figure 3.19. Alternate views of the device in Figure 3.2 and Figure 3.11 are also shown. The device contains 12 channels with two detection wells per channel which are compatible with commercial plate reader instrumentation for detection. Each channel has a threaded port for an electrode, however, this high throughput device is challenging to use as one would need many electrodes, each of which would require separate calibration. One way to make this device more user-friendly would be to separate the electrode from the device itself, i.e., make the system more modular in nature by flowing the sample first through an O<sub>2</sub> detection chip and then splitting the sample to deliver it to the ATP/NO detection

chip.



**Figure 3.19** Scaling up the original  $\text{O}_2$  and RBC ATP measurement device. The device shown in Figure 3.2 was printed as an array of channels as shown in panels C and D, each with detection wells for NO and ATP and threaded ports for oxygen detection. Alternative views of the original device are displayed in panels A and B.

## CHAPTER 4

### ***IN VITRO* DYNAMIC DOSING OF *ESCHERICHIA COLI* WITH LEVOFLOXACIN USING A 3D PRINTED MICROFLUIDIC DEVICE CAPABLE OF GENERATING PHARMACOKINETIC CURVES**

#### **4.1 Antibiotic Resistance**

Antibiotic resistance, which is a bacteria's resistance to one or more antibiotics, develops when a bacterial genome mutates to render the microbe resistant to a drug that has been used to treat the bacterial infection. A broader term, antimicrobial resistance (AMR), is used to refer to drug resistant viruses, fungi, and parasites. The Center for Disease Control (CDC), World Health Organization (WHO), and even The White House have all recently published detailed reports on the status of AMR in the US<sup>8</sup> and around the world,<sup>194</sup> as well as detailed strategies to fight AMR.<sup>195</sup> However, the awareness of the scientific community to the threat of not only antibiotic resistance but also AMR has existed for decades. However, no new classes of antibiotics have been developed in the last 30 years according to the WHO, and tracking the emergence of AMR relative to antibiotic class discoveries reveals that within 1 year of the discovery of each new antibiotic class, resistant strains were observed, as shown in Figure 4.1.<sup>8</sup>

Considering the numerous publications describing the mounting threat of antibiotic resistance, the response from the academic community has been significant, and there have been those studying AMR from distinct perspectives, particularly in the context of development and transmission mechanisms of resistance. This organismal approach of studying AMR is complemented by synthetic and computational chemists, who pursue development of alternative drugs based on computational models supported by molecular and structural biology evidence. Many drug candidates can be synthesized based on computational studies; however, efficacy testing and dosing regimen development are usually performed using cultured cell types with *in vitro* systems such as the hollow fiber chamber reactor (HFCR), an important tool in industrial and academic labs interested in





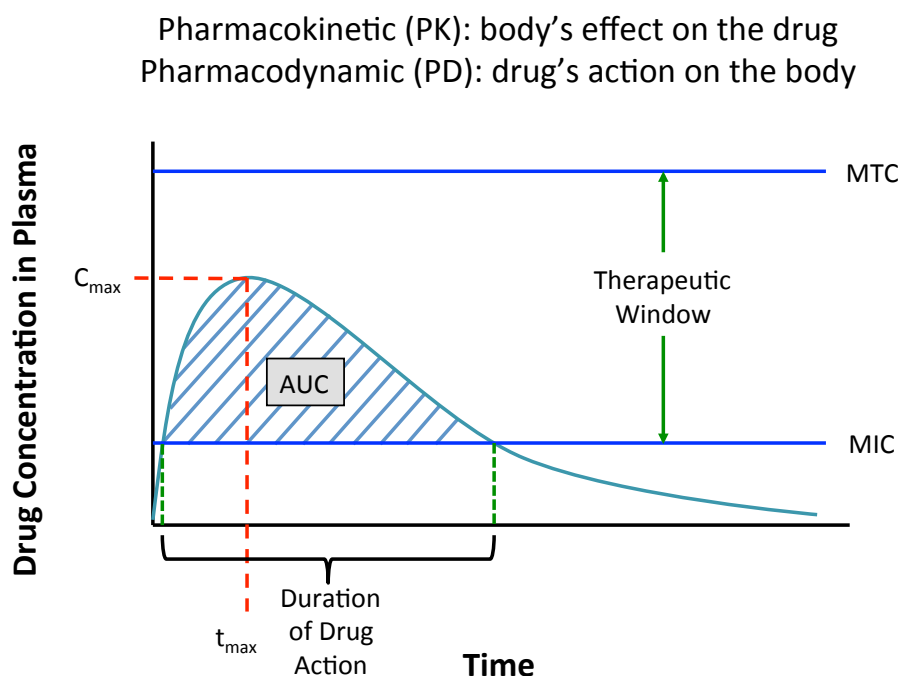
**Figure 4.1** Antibiotic Resistance Timeline Based on Literature Reports.<sup>8</sup> The left had side of the timeline lists the first observations of antimicrobial resistance in various microbial species, and the date of drug introduction for widespread use is shown to the right of the timeline. Notice that with some particular antibiotic agents – specifically with penicillin, methicillin, ceftazidime, levofloxacin, linezolid, and ceftaroline – resistance is observed within two years of the drug’s introduction to general use. In the case of penicillin, the drug was in limited use prior to its widespread availability in 1943. Note that resistance to levofloxacin was observed the same year it was introduced. Pan-drug resistance (PDR) and extreme drug resistance (XDR) are terms currently appearing in medical and clinical literature that refer to a microbes resistance to all antimicrobial agents and resistance to the majority (susceptible to two or fewer) of antimicrobial agents , respectively.<sup>9</sup> Figure adapted from the CDC.

drug discovery, to mimic *in vivo* studies typically performed on mice. These *in vitro* tools are used to prescreen drug candidates to lower the overall cost of bringing a drug to market.

## 4.2 *In Vitro* Models of Dynamic Dosing

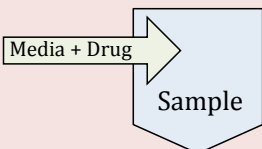
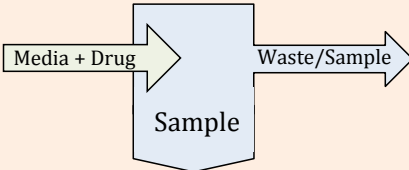
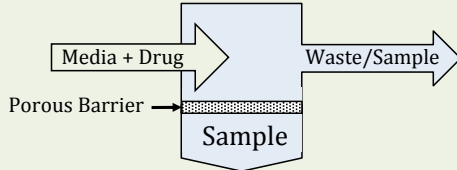
*In vitro* dosing studies are used to correlate drug efficacy to dosing regimens. The dosing regimens can be performed *in vivo* in mouse models or in an *in vitro* system. The use of the *in vitro* systems can function to pre-screen drugs before they are approved for expensive *in vivo* studies. Considering that the estimated cost to bring a drug to market is millions of dollars, with some estimates projecting between 500-800 million dollars,<sup>196,197</sup> pre-screening of viable candidates is

an integral component of the drug discovery process. The goal of the drug pre-screening process is to conduct toxicology and efficacy studies using a platform that enables mimicry of *in vivo* dosing profiles. The information of interest to the drug companies is the pharmacokinetic (PK) parameters such as maximum concentration ( $C_{max}$ ) and area under the curve (AUC) because these particular parameters correlate directly with *in vitro* efficacy.<sup>198</sup> A plot of a typical dosing experiment is shown below in Figure 4.2, detailing the  $C_{max}$  and AUC. There are many *in vitro* systems one can use to generate a PK curve, and these *in vitro* systems differ in their abilities to reproduce *in vivo* data.



**Figure 4.2** Example of a pharmacokinetic curve. *In vivo* dosing studies in mice are conducted to define parameters such as  $C_{max}$  (the maximum concentration that a drug reaches in the plasma), AUC (thought of as total dose), and bioavailability (the ratio of concentration observed to concentration administered). *In vitro* systems like those discussed below are capable of generating these parameters on an *In vitro* platform using cultured cells. The goal of a dosing regimen is to keep the  $C_{max}$  or AUC within the confines of the therapeutic window, or where the drug exhibits its maximum PD effect. MIC = minimum inhibitory concentration and MTC = maximum tolerable concentration.

Three main types of *in vitro* dosing systems (models) used in dosing studies include static, dilution-based dynamic, and diffusion-based dynamic,<sup>199</sup> and are shown in Figure 4.3. Static based systems expose a sample (bacteria or cell type) to a static concentration of drug with respect

Model	Schematic
<b>Static</b> <ul style="list-style-type: none"> <li>• Fixed concentration of drug</li> <li>• Used to determine MIC</li> <li>• Static environment</li> <li>• One compartment</li> </ul>	
<b>Dilution-Based Dynamic</b> <ul style="list-style-type: none"> <li>• Variable concentration profiles</li> <li>• Incorporates flow</li> <li>• Loss of sample</li> <li>• One compartment</li> </ul>	
<b>Diffusion-Based Dynamic</b> <ul style="list-style-type: none"> <li>• Variable concentration profiles</li> <li>• Incorporates flow</li> <li>• Sample separated from media/drug</li> <li>• Two compartment</li> </ul>	

**Figure 4.3** In vitro models of dosing models.

to time. While static systems have been historically utilized to determine minimum inhibitory concentrations (MICs), the system does have drawbacks. Specifically, the sample is in a static environment, so waste product build up and eventual lack of nutrients can affect the sample viability negatively in addition to the low oxygen exchange. Without the proper controls, it is difficult to determine whether the sample's viability decreases due to drug exposure or whether the environment is significantly affecting cell viability. Dilution-based dynamic systems eliminate the limitation of waste buildup and nutrient depletion by incorporating a flow component.<sup>200</sup> They also allow the user to modulate the drug concentration in the sample by adding concentrated drug into the flowing media. The limitation with this particular system is that the flow is usually directed over or through the sample, which can result in sample loss.

The most common system for dynamically dosing cell samples is the diffusion-based dynamic model. In these types of systems, of which the most common apparatus is the hollow fiber chamber reactor (HFCR) shown in Figure 4.4, there is a flow component to eliminate the issues with

replenishing nutrients and waste removal as in the dilution-based models, and the concentration profile can be varied with respect to time.

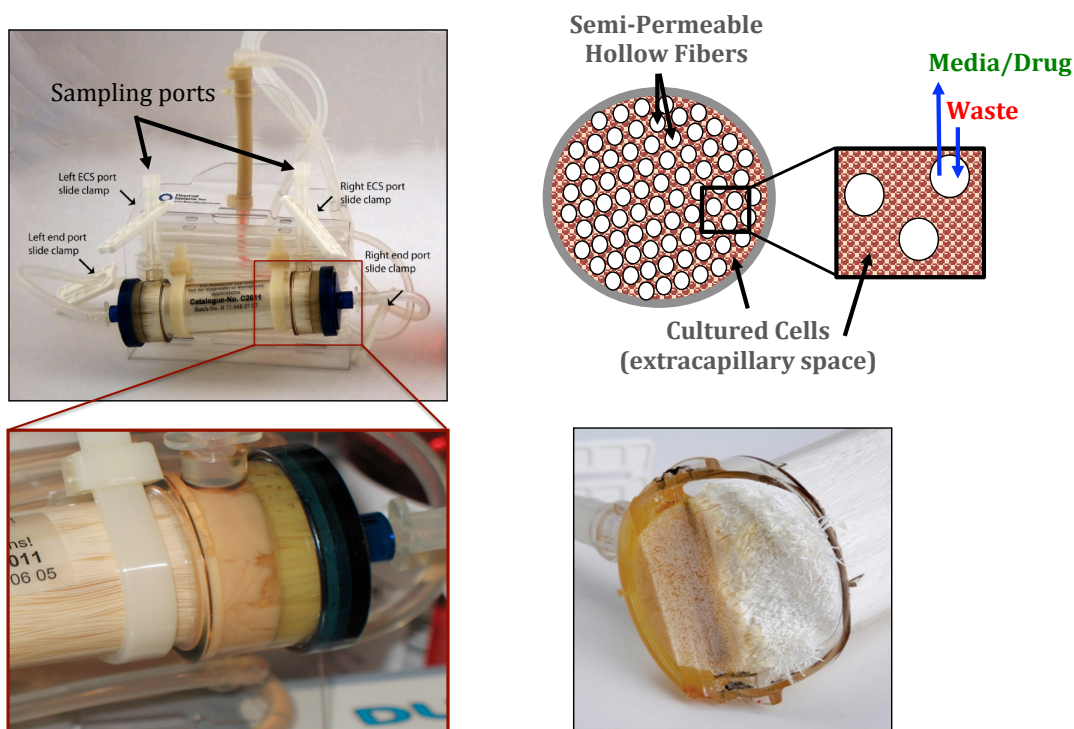


**Figure 4.4** The HFCR.<sup>10</sup> The HFCR is integrated with a circulation pump with multiple reservoirs for circulating fresh media and removing waste. There are various versions of the HFCR from Fiber Cell Systems, one of which is shown above holding a medium sized cartridge (top left). Other photos of the system are shown, including a closer view of the cartridge and a real cross section of the hollow fiber. A schematic of the cross section is at the top right of the figure. The cartridge contains many 200  $\mu\text{m}$  i.d. semi-permeable fibers that allow small molecules to diffuse across the wall of the fiber. This allows diffusion of drug and fresh media into the extracapillary space to reach cultured cells and diffusion of waste products into the capillaries to be pushed to waste. Photos reproduced with permission from Fiber Cell Systems.

However, in the HFCR, the sample is physically separated from the flow by porous, semi-permeable (size-exclusion) fibers about 200  $\mu\text{m}$  in diameter, which allow small molecules to diffuse across the membrane while keeping the cells isolated from the flow. Drug-containing media can be perfused through a cartridge and through the hollow fibers inside the cartridge as shown in Figure 4.4. This allows drug and nutrients to diffuse into the extra-capillary space to the sample, and at the same time waste products diffuse into the capillaries and are flushed out to waste. Aliquots are sampled from the extra-capillary space in the cartridge via access ports; however,

recovery of the cells or bacteria after dosing is difficult, limiting the system's ability to generate pharmacodynamic (PD) data to gauge the efficacy of the drug on the target. HFCR cartridges typically cost \$500 per cartridge and are single use. In some experimental schemes, cartridges are aligned serially making it possible to obtain more trials per experiment, but the technology is still relatively low throughput. One other significant disadvantage to this system is the large volumes of media and subsequently mass of drug that is required during experiments. This can significantly impact a drug company's synthetic division operations if large quantities are required.

To address some of these issues with current *in vitro* systems, the 3D printed device in Figure 4.5 was fabricated and was empirically characterized.<sup>201</sup> The details of this characterization using fluorescein and levofloxacin can be found in the referenced thesis. The device is modeled after the HFCR and incorporates flow along with control over concentration profiles. The volumes of media used are less than those used in the HFCR, and the sample can be accessed after dosing is complete. This is possible through the incorporation of commercial transwell membrane inserts into the device. The device is also compatible with a commercial plate reader, which was used for the optimization studies.<sup>201</sup>

This chapter will not go into detail of the device characterization that has been previously described, but it will describe the device's application to dynamically dosing bacteria, specifically *E. coli*. In this chapter, I demonstrate the device's capability to perform dynamic dosing studies while obtaining PD information from a sample of bacteria, with objective to address a goal outlined by The White House, which is to "accelerate basic and applied research and development for new antibiotics...".<sup>195</sup>

## 4.3 Methods

### 4.3.1 Fabrication of Devices

The 3D printed device was fabricated in the same manner as the 3D printed devices discussed in Chapter 3 and is shown in Figure 4.5. Briefly, an .STL file was created from a part file in Autodesk

Inventor Student Edition and was sent to the engineering department for printing. This particular device has 6 channels with dimensions 80 mm x 2 mm x 0.5 mm. Each channel contains a well to accommodate a commercial transwell insert.

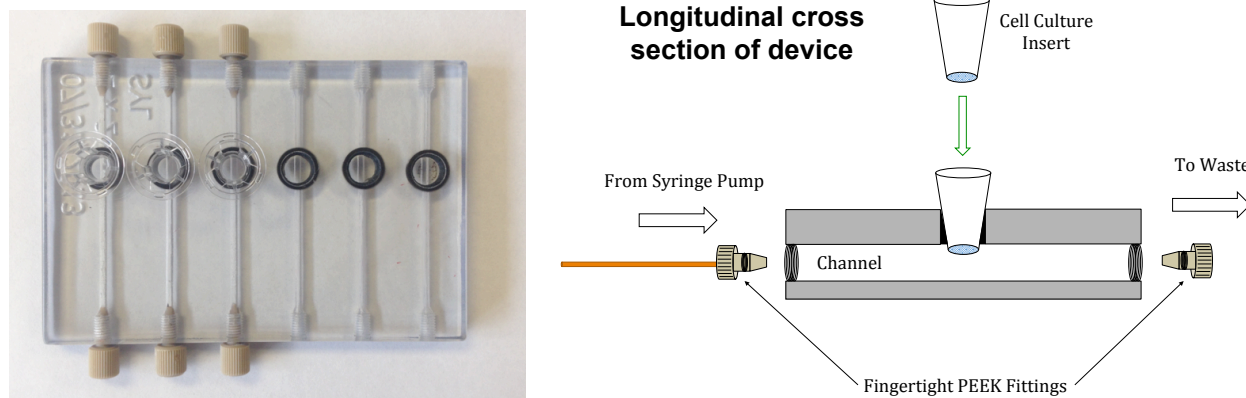


**Figure 4.5** 3D Printed Device for Dosing Bacteria. A picture of the device is shown on the left, and a cross section of the device is shown on the right. Each of the six channels is 2 mm in width and 0.5 mm in height. The device has threaded ports (right handed 10-32) to accommodate commercial fittings and capillary tubing that allow connection to syringe pumps. Capillaries can be fitted into each inlet/outlet using the finger tight fittings. Photo repurposed with permission from Sarah Y. Lockwood.

Solutions (119  $\mu\text{M}$  levofloxacin and BSA free PSS) were flowed through the device at 10  $\mu\text{L}/\text{min}$  using syringe pumps (Harvard) and 5 mL gastight luer lock syringes (Hamilton, Reno, NV), outfitted with PEEK luer locks (IDEX Health and Science, Oak Harbor, WA) to interface the syringe to fused silica capillary tubing (i.d. 536  $\mu\text{m}$ : o.d. 669.7  $\mu\text{m}$ , Polymicro Technologies, Phoenix, AZ). The 0.4  $\mu\text{m}$  well inserts were commercially obtained from Corning, but the 0.2  $\mu\text{m}$  well inserts were fabricated in house, as commercial vendors do not sell transwell membranes with 0.2  $\mu\text{m}$  i.d. pore sizes. The inserts for 0.2  $\mu\text{m}$  studies were fabricated reusing old commercial well inserts. First, the old membrane and adhesive material was removed using forceps. Next, strips of 0.2  $\mu\text{m}$  pore size membrane (Sterlitech, Kent, WA) were cut from a membrane sheet. The strips were affixed to the base of the old well inserts using about 30  $\mu\text{L}$  of acetone, which was pipetted onto the ridge of the previously used insert. Acetone proved to be a good solvent for this, as it allowed enough time to affix the membrane without completely evaporating. An attempt to use dichloromethane was made, but the reagent evaporated too quickly to be useful. While this

fabrication process was tedious, and the fabrication success rate scaled with experience, it is a worthwhile procedure for those who want or need to change pore sizes, as the smallest pore size available for the commercial inserts is 0.4  $\mu\text{m}$ .

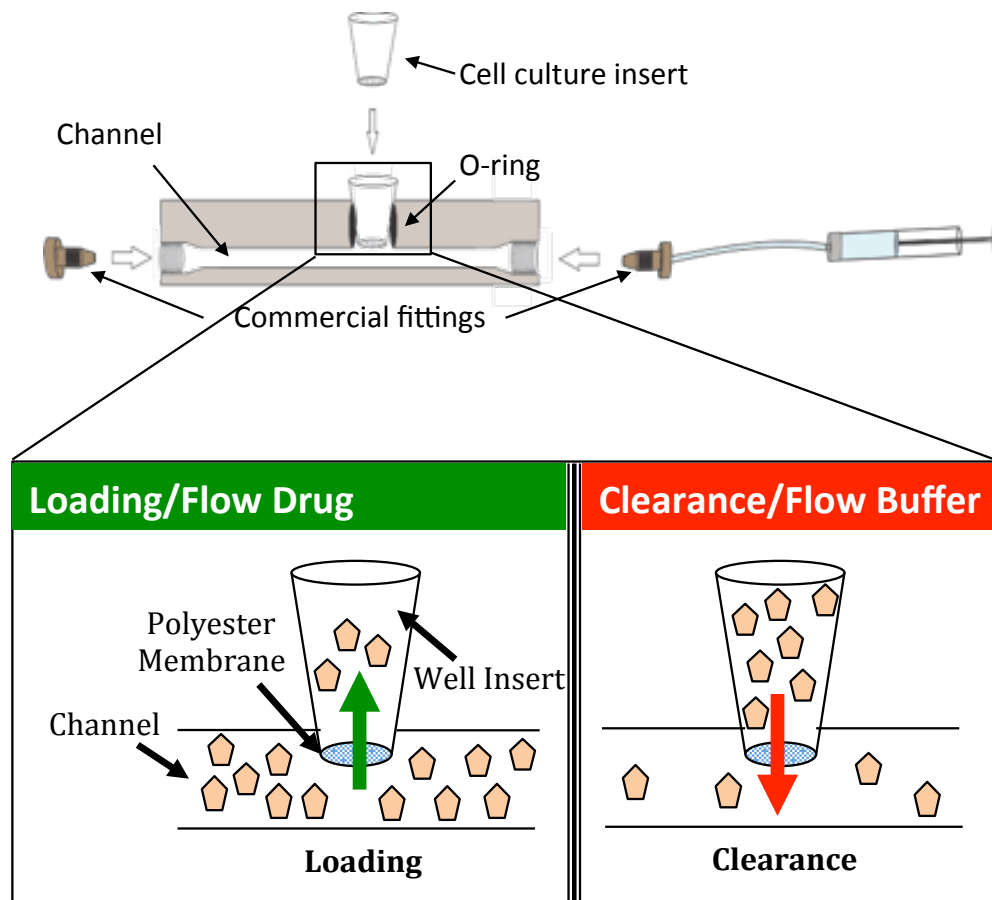


**Figure 4.6** Basis of PK loading and depletion profiles. The neutral colored pentagons represent a drug molecule. When concentrated drug, e.g., levofloxacin, is flowed through the channels of the device shown in Figure 4.5, a concentration gradient develops across the membrane of the well insert. The drug will diffuse with the gradient, across the membrane, and into the well until the gradient is minimized. For the case on the right, drug has been loaded into the well insert of the device for some time, and then pure buffer is flowed through the channels, reversing the gradient. This time, the drug will diffuse out of the well insert to diffuse with the concentration gradient. This is the relationship, described by Fick's laws of diffusion, governs the generation of PK profiles shown in Figure 4.9 and Figure 4.10.

### 4.3.2 Preparation of Reagents

The buffer used for dosing experiments was BSA free PSS. PSS was prepared as described in Chapter 2, except without BSA. Stock solution of levofloxacin was prepared as 6 mM in 1:1

methanol:water. An internal standard stock solution of 3 mM ciprofloxacin (Sigma) in 2% acetic acid/water (v/v) was prepared. Standards of levofloxacin (Sigma) (0-10  $\mu$ M) were prepared by diluting 119  $\mu$ M stock with buffer. To prepare the standards for LC-MS analysis, standards were diluted 21-fold using a 750 nM ciprofloxacin working solution in acetonitrile (internal standard), and 80  $\mu$ L of each standard was loaded into a PCR plate, which was subsequently sealed with Rapid EPS seal (BioChromato, Fujisawa, Japan). Samples collected during the course of dosing experiments were diluted 8-fold in BSA free PSS and were subsequently diluted 21-fold with 750 nM ciprofloxacin in acetonitrile, so that the detected concentration would fall in the range of the calibration curve.

#### **4.3.3 Monitoring Levofloxacin Concentration Using Liquid Chromatography Mass Spectrometry**

Liquid chromatography with mass spectrometry (LC-MS/MS) using multiple reaction monitoring (MRM) was used to measure the levofloxacin concentration with respect to time during dosing experiments, as described elsewhere (Lockwood, S.Y. et al. *In Preparation*). Briefly, a Waters Quatro Micro triple quadrupole mass spectrometer housed in the MSU Mass Spectrometry and Metabolomics Core Research Technology Support Facility was used in conjunction with a Supelco Ascentis precolumn and Supelco Ascentis Express C18 column (Supelco, Bellefonte, PA) with a length of 3 cm, internal diameter of 2.1 mm, particle size of 2.1  $\mu$ m. An autosampler was used to inject 10  $\mu$ L of sample onto the column. Solvents used were methanol (A), acetonitrile (B), and 1% formic acid + water (C).

MRM, like selective ion monitoring (SIM) or single reaction monitoring (SRM), can lower the background associated with a signal. However, MRM is a two-part mass selection (MS/MS), and operates by first selecting a precursor ion to monitor for subsequent product ion formation. SIM or SRM identifies analytes based on a single fragmentation, with one or more identification peaks. Instrument parameters and the gradient program are detailed in the tables below. The detection parameters for ciprofloxacin and levofloxacin are included in the table below.



Time	%A	%B	%C	Flow Rate(mL/min)
0.25	95	0	5	0.495
1.00	2	0	98	0.495
1.25	2	0	98	0.495
1.75	30	15	55	0.495
1.90	30	15	55	0.495
2.00	95	0	5	0.495

**Table 4.1** Solvent program for detection of ciprofloxacin and levofloxacin using (A) methanol, (B) acetonitrile, and (C) 1% formic acid + water.

Parameter	Ciprofloxacin	Levofloxacin
Ionization Mode	ESI +	ESI +
Molecular Weight (g/mol)	331.35	361.37
Precursor Ion (m/z)	332.20	362.10
Product Ion (m/z)	231.00	261.10
Retention Time (min)	1.51	1.48
Dwell (sec)	0.030	0.030
Cone Voltage(V)	25	30
Collision Energy (eV)	45	30
Collision Gas Pressure (Torr)	$1.96 \times 10^{-3}$	$1.96 \times 10^{-3}$

**Table 4.2** Mass spectrometry parameters for detection of ciprofloxacin and levofloxacin.

#### 4.3.4 Bacteria Growth and Purification

An inoculation loop was used to scrape a portion of a frozen stock of chemically competent *Escherichia coli* (BL21DE3, Novagen, Gibbstown, NJ). The loop was then streaked across sterile lysogeny broth (LB, Lennox, EMD Chemicals) agar containing 50 µg/mL kanamycin phosphate (Sigma). The plate was incubated at 37°C overnight to promote colony growth. The next day, a sterile inoculation loop was used to pick one colony and inoculate approximately 50 mL of sterile, liquid LB containing 50 µg/mL kanamycin phosphate. The culture was grown at 37°C with shaking at 180 rpm for 3 hours. After 3 hours, the culture was transferred to a 50 mL polypropylene centrifuge tube (Greiner Bio-One). The sample was centrifuged for 15 minutes at 3000  $\times$  g to obtain a pellet. The supernatant was removed by aspiration, and two milliliters of BSA free PSS were added to resuspend the pellet. The sample was washed 2x more at 3000  $\times$  g for 15 minutes,

and supernatant was aspirated off each time. The resulting pellet was resuspended in 10 mL BSA free PSS, and the optical density was adjusted to  $0.06_{OD670nm}$  using a commercial plate reader (SpectraMax, Molecular Devices) and a 96-well clear polycarbonate plate (Greiner).

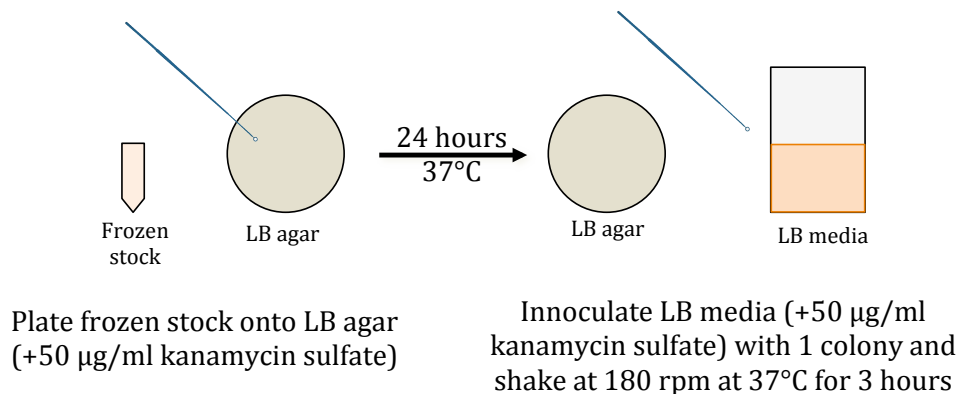


**Figure 4.7** *E. coli* growth and purification protocol. Colonies were grown overnight by streaking frozen stock (cryostored in 50% glycerol/water) onto an agar plate with kanamycin phosphate. The next day, one colony was picked from the agar using an inoculation loop, and approximately 50 mL of LB was inoculated with the colony. This was allowed to grow for 3 hours with shaking, and the cells were subsequently purified.

#### 4.3.5 Dosing Methods

The time at which  $C_{max}$  occurs and its magnitude have been investigated previously by the Spence lab.<sup>201</sup> The work focused on the development of the device shown in Figure 4.5 and the characterization of the loading rates driven by diffusional gradients of multiple small molecules. Based on the diffusional properties of fluorescein (MW), which has a similar molar mass in comparison to levofloxacin (332.31 g/mol), Lockwood developed an empirical model to predict the concentration of levofloxacin required in the channel that would result in a desired  $C_{max}$  after 1 hour of flow. Based on this empirical model, 119  $\mu\text{M}$  levofloxacin was pumped through the channels of the device to achieve a desired 25  $\mu\text{M}$   $C_{max}$  for membranes having 0.4  $\mu\text{m}$  pore diameters. This particular value for  $C_{max}$  (25  $\mu\text{M}$ ) was targeted because it is approximately the  $C_{max}$  observed *in vivo* in humans.<sup>202</sup> The  $C_{max}$  for experiments with 0.2  $\mu\text{m}$  pore diameters was approximately 70  $\mu\text{M}$ , and it is thought that this difference can be accounted for by considering the pore density

and areas of the two pore sizes (see Results and Discussion). If a higher  $C_{max}$  is desired using the same pore size, a higher concentration of levofloxacin must be pumped beneath the well insert membranes to increase initial loading. In addition, loading of levofloxacin into the 3D printed device material was taken into account in this empirical model,<sup>201</sup> and the concentrations reported are the concentrations samples directly from the well insert.

Purified *E. coli*, 75  $\mu$ L of approximately  $10^7$  cells/mL, were loaded into the Transwell inserts (either 0.4 or 0.2  $\mu$ m pore size), and flow of the 119  $\mu$ M levofloxacin stock was started. As the stock solution passed under the transwell insert, a timer was started (time = 0 hours). Aliquots of 5  $\mu$ L were removed from the well insert every 30 minutes to monitor drug concentration in the well and were diluted as described in the methods section. At the 1 hour mark, a sample was taken, and the syringes loaded with levofloxacin stock were disconnected from the device. Syringes loaded with BSA free PSS (no levofloxacin) were secured to the syringe pump, and the syringes were connected back to the device. Flow was started again, and the 1 hour mark was noted when the new flow profile (BSA free PSS with no antibiotic) passed below the well inserts. This ensured that the timing of  $C_{max}$  would be at 1 hour during the course of the buffer changeover and results in the profiles seen in Figure 4.10. The profile seen in Figure 4.9 was generated by a different user, and the timing of  $C_{max}$  can vary depending on the timing control and other user differences at the 1 hour mark. For the static experiments, 1 mL of  $10^7$  cells/mL was spun down at  $3000 \times g$  and the supernatant was aspirated off without removing the pellet. Cells were resuspended in 1 mL of 25  $\mu$ M or 70  $\mu$ M levofloxacin and were allowed to incubate at room temperature for 5 hours.

#### 4.3.6 Standard Plating Methods

After dosing experiments were complete, the remaining sample was collected from the well. Ten-fold dilutions of each sample were prepared for plating, up to  $10^{-6}$  fold. Samples were plated using the spread plate method on LB + kanamycin (50  $\mu$ g/mL) agar plates made in house. Plates were allowed to incubate at 37°C for approximately 24 hours, after which the colony forming units (CFUs) were counted and number of cells in the original sample were calculated. Plating was also

performed for the starting sample to obtain a count for the initial number of cells. Plating data is represented as Log(CFU/mL).

## 4.4 Results and Discussion

### 4.4.1 Confirmation of *E. coli* Viability in Device

Prior to dosing the purified bacteria samples with dynamic levofloxacin profiles, a control was performed to ensure the sample would survive in the well insert when subjected to flow for 24 hours. To perform this experiment, 75  $\mu$ L of purified *E. coli* was loaded into the device's well insert, and flow was started at 1  $\mu$ L/min using 5 mL capacity syringes (Hamilton) and syringe pumps (Harvard). Flow was stopped after 24 hours, and the sample was removed from the well inserts. Viability of the sample was measured using standard plating methods. The viability of bacteria exposed to flow on the 3D printed device (Flow bar in Figure 4.8) and the samples exposed to static conditions in well inserts in a buffer-filled well plate (Non-flow bar in Figure 4.8) were not significantly different from the initial concentration of bacteria (Live Control bar), all of which are on the order of approximately  $10^7$  cells/mL.

This suggests that the viability of the cells is not significantly impacted by the device materials. Whether it would be more desirable for cell growth in the transwell inserts to be completely uninhibited or not is a debatable experimental condition. Criticism of the current system include that the bacteria are not kept at optimal temperature and that the bacteria are not in the optimal buffer to promote growth. The former concern is legitimate and is easily addressed by incorporation of an oven into experimental dosing protocols. The latter concern is biologically irrelevant. While the conditions that bacteria thrive in may vary based on pH and in salt concentration *in vivo*, they are not likely to be incubating in optimal growth media (lysogeny broth) in the human body.

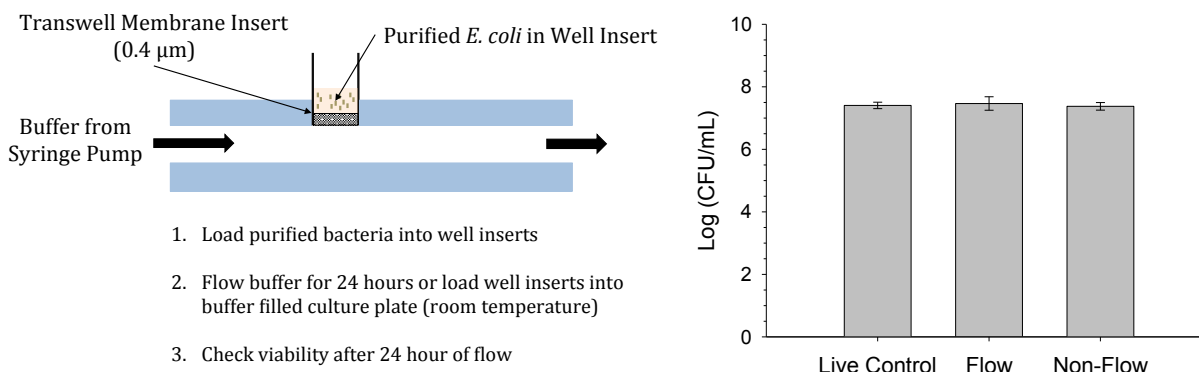


**Figure 4.8** Flow and Non-flow studies to confirm bacteria viability in the 3D printed device. Bacteria were loaded into commercial transwell inserts on the 3D printed device and were subjected to flow of buffer for 24 hours. A non-flow comparison was performed by placing loaded inserts into culture plates loaded with buffer. Viability was probed using standard plating methods described above. From the plot above, the viability of the samples exposed to static conditions in a plate (Non-Flow,  $\text{Log}(\text{CFU/mL}) = 7.4 \pm 0.1$ ) and flow conditions (Flow,  $\text{Log}(\text{CFU/mL}) = 7.5 \pm 0.2$ ) in the 3D printed device were not significantly different relative to the purified sample of *E. coli* (Live Control,  $\text{Log}(\text{CFU/mL}) = 7.4 \pm 0.1$ ). This confirmed that the device conditions were not adversely affecting the viability of the cells, at least over the course of 24 hours.  $N = 3$  trials. Error = standard deviation.

#### 4.4.2 Dosing *E. coli* with Dynamic Profiles of Levofloxacin

When 75 μL of purified *E. coli* were exposed to the dose profile shown in Figure 4.9 ( $C_{\text{max}} = 25.0 \pm 5.7$  μM levofloxacin), the number of viable bacteria in the well insert decreased significantly by nearly 4 orders of magnitude ( $\text{Log}(\text{CFU/mL}) = 4.7 \pm 1.0$ ) relative to the live control sample ( $\text{Log}(\text{CFU/mL}) = 7.9 \pm 0.11$ ). To compare the samples to a statically dosed sample, cells were exposed to 25 μM levofloxacin for 5 hours. At the end of 5 hours, samples were diluted and plated, and from Figure 4.9, the viability of the sample also decreased significantly and more so than the dynamically dosed sample ( $\text{Log}(\text{CFU/mL}) = 1.9 \pm 1.1$ ).

This can be rationalized by imagining the dose profile of a statically dosed sample versus the profile in the middle panel of Figure 4.9. The dosing profile of the static sample might be a line with negative or no slope, which would depend on if bacteria metabolize levofloxacin. Levofloxacin is a DNA synthesis inhibitor, specifically a DNA gyrase and topoisomerase IV inhibitor,<sup>203</sup> which are two enzymes specific to the bacterial genome. Unless the bacteria can metabolize or break down the drug, the concentration should stay relatively constant throughout the course of the 5 hour ex-

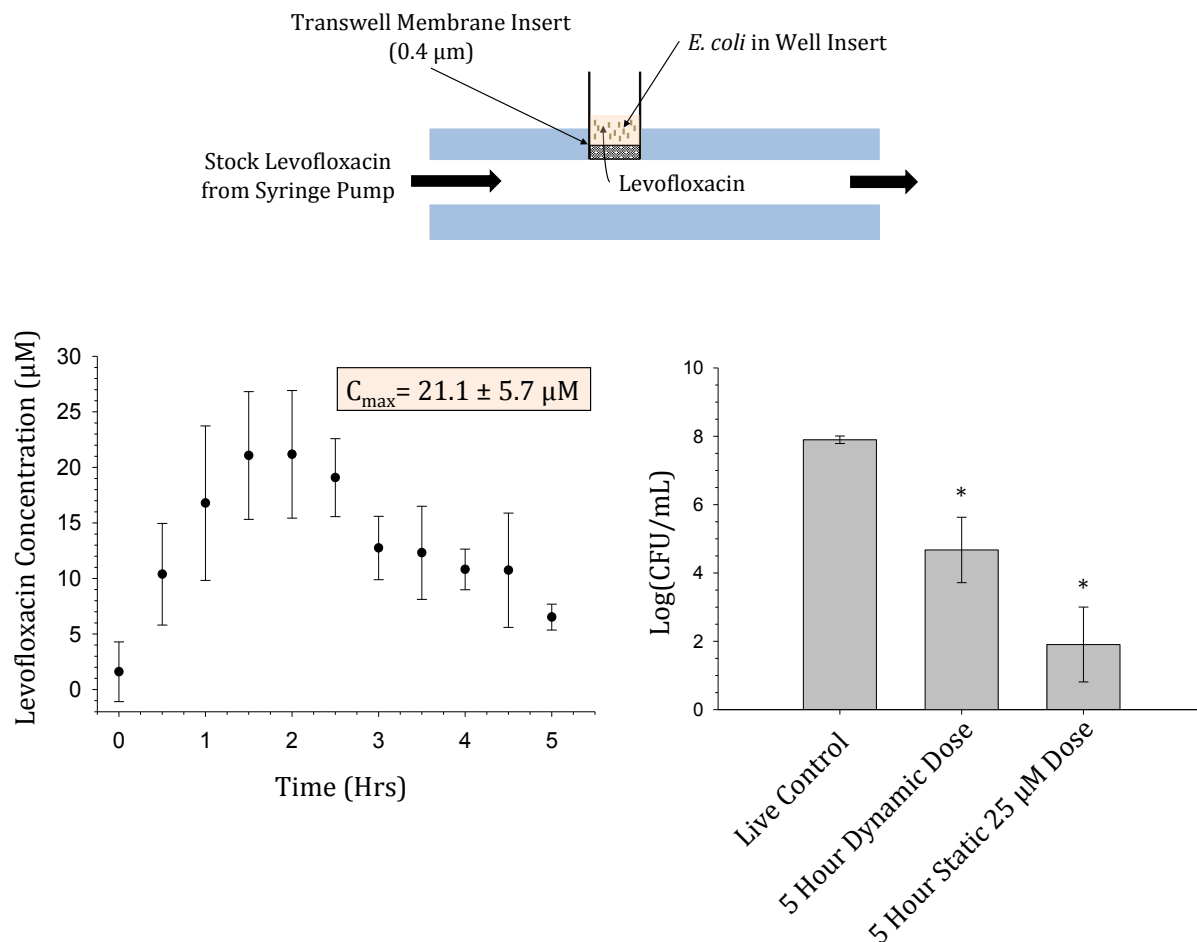


**Figure 4.9** Dosing *E. coli* using a profile with a  $C_{\text{max}}$  of 25  $\mu\text{M}$ . The dose curve shown in the middle panel was measured from the well insert, and the bacterial viability was measured after dosing. The concentration of levofloxacin in the insert rises to a  $C_{\text{max}}$  of  $21.0 \pm 5.7$  in 1.5 hours. The viability of the *E. coli* after dosing, with respect to the live control ( $\log(\text{CFU/mL}) = 7.4 \pm 0.1$ ), was  $\text{Log}(\text{CFU/mL}) = 4.7 \pm 1.0$ . A static dose of 25  $\mu\text{M}$  for 5 hours killed more bacteria on average ( $\log(\text{CFU/mL}) = 1.0 \pm 1.1$ ) compared to the dosed sample.  $N = 3$ . Error = standard deviation.  $*p < 0.05$ .

periment, which when compared to the dose profile shown, is not necessarily a good representative of an *in vivo* dosing profile. A calculation of the AUC for the dynamic curve yields an AUC of  $75 \pm 10 \mu\text{M} \cdot \text{Hr}$ , which is smaller than a theoretical AUC for 25  $\mu\text{M}$  applied over 5 hours ( $125 \mu\text{M} \cdot \text{Hr}$ ). A single trial of bacteria statically dosed 25  $\mu\text{M}$  levofloxacin yielded a viability statistically equivalent with the dynamically dosed sample (not shown). Considering that the AUC for this particular sample would be predicted to be 25  $\mu\text{M} \cdot \text{Hr}$ , it would be expected that the viability would be higher than or even statistically equivalent to the dynamically dosed sample. Given that

AUC/MIC correlates well with *in vitro* efficacy, it is not surprising that the statically dosed sample would be less viable at the end of the experimental time point.

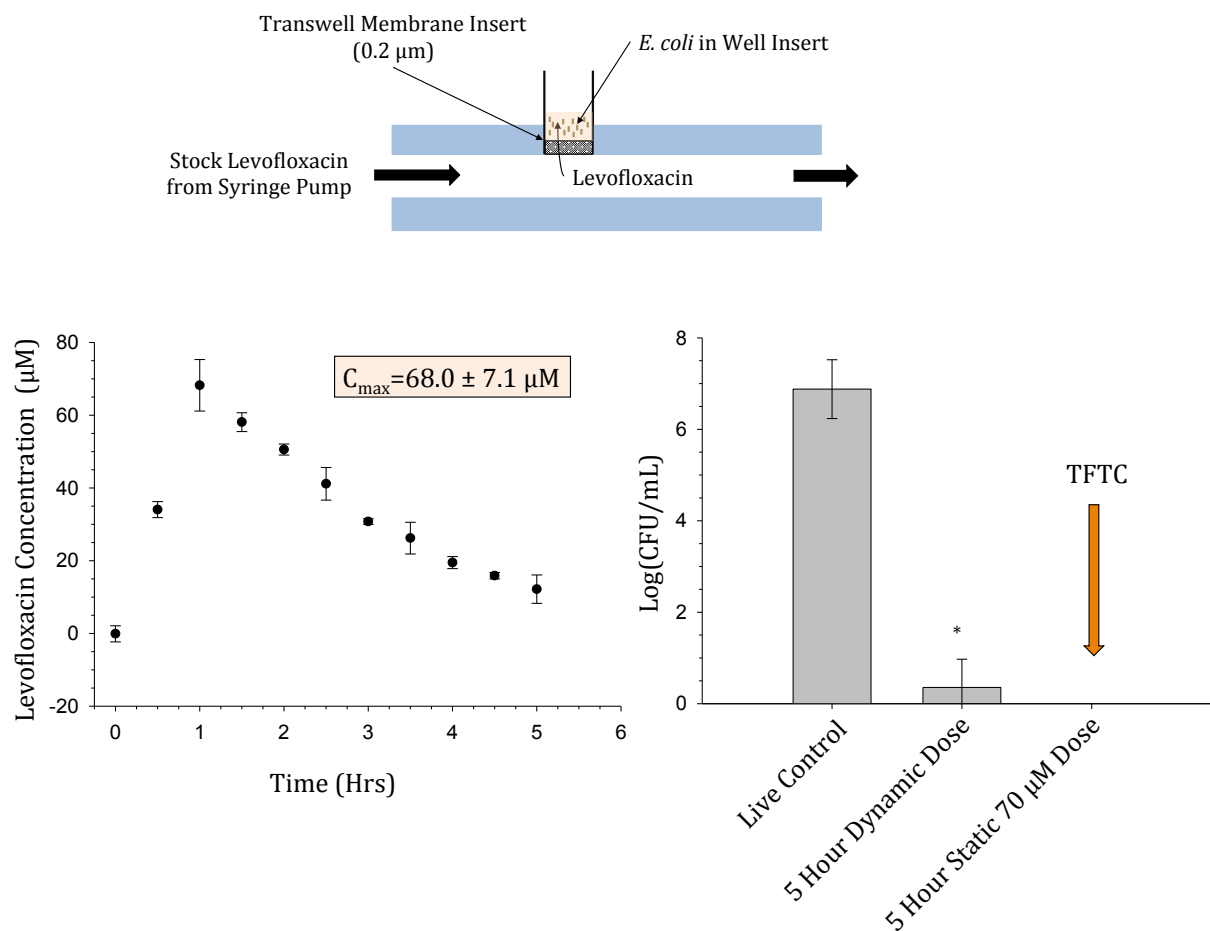


**Figure 4.10** Dosing *E. coli* using a profile with a  $C_{max}$  of nearly 70  $\mu\text{M}$ . The dose curve shown in the middle panel was measured from the well insert, and the bacterial viability was measured after dosing. The concentration of levofloxacin in the insert rises to a  $C_{max}$  of  $68.0 \pm 7.1 \mu\text{M}$  in 1 hour. The viability of the *E. coli* after dosing, with respect to the live control ( $\log(\text{CFU/mL}) = 6.9 \pm 0.6$ ), was  $\text{Log}(\text{CFU/mL}) = 0.4 \pm 0.6$ . A static dose of 70  $\mu\text{M}$  for 5 hours killed all the bacteria in the sample (no colonies to count or TFTC) compared to the dosed sample.  $N = 3$ . Error = standard deviation. \* $p < 0.05$ .

In Figure 4.10, similar effects were observed for a dosing profile with a higher  $C_{max}$  ( $68.0 \pm 7.1 \mu\text{M}$  levofloxacin) and AUC relative to the MIC for levofloxacin, which is 1-4  $\mu\text{g/mL}$  (3-6  $\mu\text{M}$ ). This particular dose curve killed more bacteria on average ( $\text{Log}(\text{CFU/mL}) = 0.4 \pm 0.6$ ) relative to controls ( $\text{Log}(\text{CFU/mL}) = 6.9 \pm 0.6$ ) than the profile in Figure 4.9 as expected, as did the statically dosed sample ( $\text{Log}(\text{CFU/mL}) = \text{Too Few to Count (TFTC)}$ ). The calculated AUC from the data in

the dose curve yield an AUC of  $175 \pm 7 \mu\text{M}\cdot\text{Hr}$ . A static dose profile of  $70 \mu\text{M}$  applied over 5 hours would theoretically yield an AUC of  $350 \mu\text{M}\cdot\text{Hr}$ . From the viability data in Figure 4.10, it would be expected to see a higher kill rate with a static dose than with the dynamic dose profile based on the calculated AUCs.

#### **4.4.3 Application to AMR**

Considering these data follow the trend for drug efficacy based on AUC and  $C_{max}$ , this particular system is recommended for PK/PD studies. In addition, it is possible to use this device to study the evolution of AMR in a controlled manner. For example, a researcher could subject a wild type strain or clinically isolated strain to physiologically relevant drug concentrations using a controlled dose curve after which the sample could be collected and analyzed using flow cytometry and/or genomic methods to probe for the development of resistance. This would be most useful to the researcher who does not have access to animal models of infection or human donors from hospitals but desires a more biologically relevant system with which to probe mechanisms of resistance in a systematic fashion. Because of the ease of access to cells cultured in the well insert, it would be possible to build this system in terms of its complexity, e.g., culture an endothelium or other cell type to monitor bacterial behavior and evolution in a more complex *in vivo* mimic.

### **4.5 Conclusions and Future Work**

#### **4.5.1 Extension of the Existing Empirical Model**

The initial characterization of the device was performed using fluorescein, and levofloxacin was a prime candidate for further characterization because of its similar molecular weight. It is possible to determine the concentration of drug required underneath the membrane based not just on empirically determined loading rates, but on molecular weight. This relationship can be determined by measuring loading rates for a set of molecules spanning a large range of molecular weights, preferably fluorescent molecules so that the experiments can be done using the commercial plate



reader. Using the loading rate vs. molecular weight plot and regression analysis, the concentration required in the device's channels to obtain a specific  $C_{max}$  in the well inserts at a specific time can be determined, solely based on the molecular weight of the drug.

#### **4.5.2 Extending the Half Life for Levofloxacin to Better Mimic In Vivo Dose Profiles**

One other challenge associated with using this *in vitro* system to mimic *in vivo* dosing profiles is that the half-life ( $t_{1/2}$ ) for drugs can vary. The half-life for levofloxacin *in vivo* in humans is between 6-8 hours. Currently, the half-life observed in our studies is  $1.55 \pm 0.06$  hours ( $N = 12$  trials, Error = standard deviation). In order to extend the half-life to 6-8 hours, gradient solutions of drug can be flowed through the channels after  $C_{max}$  is reached. In this manner, the concentration gradient across the polyester membranes can be controlled in order to manipulate the depletion kinetics. This could be accomplished by 3D printing T-junctions and by controlling the flow rate on programmable syringe pumps. This way, the user can load the cell of interest into the insert, start the program, and periodically monitor drug concentration and cell viability without needing to manipulate the flow of buffer manually.

#### **4.5.3 Multi-day Dosing of *E. Coli* or other Bacterial Strains**

The studies above took place over 5 hours, and from Figure 4.8, it is noted that the viability of the bacteria is not affected by the device over 24 hours. In order to extend the device's ability to enable multi-day dosing studies, the viability of bacteria in the device under conditions with no drug must be investigated. It is also noteworthy that the data from Figure 4.8 do not indicate that the bacteria are growing in the insert, which is likely because they are in BSA free PSS, which contains physiologically relevant concentrations of salt and glucose, i.e., this is not lysogeny broth and it is unrealistic to expect the bacteria to grow uninhibited in BSA free PSS. This may be one limitation to the data interpretation for this chapter. It would be desirable for the bacteria to exhibit uninhibited growth over the course of 24 hours, but this is something that should be resolved in future studies.

## CHAPTER 5

### CONCLUSIONS

#### 5.1 Future of HU and Hypoxia Studies: Applications in Sick Cell Disease and RBC ATP Release

The experiments from Chapter 2 have shown that deformation-induced RBC-derived ATP increases after incubation with HU. One fate of ATP released from HU-incubated RBCs was demonstrated to be that of inducing endothelial NO production, suggesting that when incubated with HU, the human RBC is a more sensitive participant in blood flow, capable of inducing vasodilation *in vivo*. This data provides an explanation of the immediate benefits in vascular tone observed clinically in patients taking HU. Future studies would include determining the molecular level interaction between HU and the RBC. This would require elucidation of the binding or uptake mechanism of HU on or in to the RBC. The GC-MS protocol outlined in Chapter 2 presents an opportunity to obtain a binding curve.

One overarching goal of the HU project was to develop a circulation mimic to probe HU's effects on deoxygenated RBCs obtained from donors with sickle cell anemia. The on-chip deoxygenation region can be developed rapidly with 3D printing technologies by printing deoxygenation regions into the device itself, or alternatively, the commercial Transwell inserts can be utilized in conjunction with Oxyrase to create oxygen sinks to deoxygenate a flowing stream of RBCs. This concept was investigated unsuccessfully with a hybrid PDMS-epoxy device using embedded electrode and flow injection analysis, but the platform itself was not reusable or rugged enough to accommodate the modular nature required of such a system. It is anticipated that 3D printing can provide the rugged, reusable platform to fabricate such a modular device.

This circulation mimic can then be used to make hypoxia measurements, which would facilitate investigation of HU and hypoxia's effects on RBCs. Preliminary data suggest that the two stimuli may be the same in that their relative contributions to RBC ATP release are non-additive. How-

ever, these studies were performed under purged conditions without monitoring oxygen tension in the sample, so it is difficult to comment on whether the hypoxic stimulus was in the physiologically relevant range, which is critical when attempting to derive the measurement's physiological significance.

The technology developed in Chapter 3 reveals an interesting relationship between hypoxia induced RBC ATP release and measured dissolved oxygen. The RBC ATP release increases and saturates within the first 20% of hemoglobin desaturation, suggesting that the ATP release is dependent on the conformation of heme in a non-linear fashion. Because *in vivo* oxygen tensions in the blood stream do not typically drop below 40 mmHg, there would be no need for the RBC to release more ATP in response to lower tensions of oxygen, i.e., the RBC would not need to be sensitive to oxygen tensions that are not physiologically relevant. The development of integrated electrodes for the 3D printed device for oxygen measurements provided a way to confirm the oxygen tension in a flowing stream, and the integration of NO electrodes is an exciting possibility that has the potential to facilitate experiments to further our understanding of the role of RBC-derived NO in the mechanism of ATP release.

A major application of this technology is for the investigation of stored RBCs. It is known that during storage RBCs lose their ability to release ATP in response to both hypoxia and deformation.<sup>193,204</sup> Probing RBC response to systematically lowered oxygen tensions could prove useful in elucidating the molecular level changes that occur in the RBC storage lesion.

## **5.2 Blood and Bacteria: An *In Vitro* Model for Sepsis and Infections on Chip**

Currently, there is no model of sepsis on a microfluidic platform to allow systematic study of one or more whole blood components in response to sepsis-inspired stimuli. There are many microfluidic technologies that have been developed and integrated with detection schemes to measure low quantities of bacteria,<sup>205–209</sup> but currently there is no device that mimics a blood stream stimulated by components of sepsis, e.g., the bacterial endotoxin lipopolysaccharide (LPS) or toxic releasates (exotoxins). Current *in vitro* experiments rely on blood collection from septic patients admitted to

intensive care units (ICUs), and typically their blood components are studied in the context of the immune response. *In vivo* studies are typically performed on mouse models using a cecal ligation procedure, which seems to be the most widely used procedure though others exist.<sup>210</sup> However, there are differences between the progression of the infection in mouse models and in humans that provide a challenge in translating results from mouse models<sup>211,212</sup> into successful treatment options for patients.

### 5.2.1 RBC Response to Sepsis

The circulation in sepsis patients and in mice with sepsis is significantly altered compared to controls. The capillary density in the microcirculation is notably decreased, and blood flow is “maldistributed”,<sup>213</sup> which suggests a more global problem with the vasculature. Also observed are increases in adhesion interactions between white blood cells, platelets, and endothelial cells.<sup>214,215</sup>

Interestingly, it has been observed that RBCs<sup>214,216–219</sup> and neutrophils<sup>215,220</sup> isolated from sepsis patients have decreased deformability, and it has been noted that intracellular RBC ATP is also decreased. This would suggest that under flow conditions, septic RBCs would release less ATP relative to controls. One speculative reason for such a decrease in deformability could be attributed to intracellular changes (increased 2,3-BPG) that result in an increase in intracellular viscosity. Membrane deformability may be a useful diagnostic of infection in humans and in dogs treated for trauma,<sup>221,222</sup> and it would be worthwhile to recapitulate this system on a microfluidic device in order to tease out specific targetable interactions in a model septic bloodstream. Before moving to a device, the deformability studies and ATP release would need to be replicated and measured, respectively. Stimuli for sepsis initiation of the RBCs would also need to be investigated or gleaned from the literature, e.g. it is known that bacteria release LPS encapsulated toxic proteins from their membranes.

The devices used in Chapters 3 and 4 would provide a platform with which to recapitulate the septic bloodstream. Bacteria can be cultured in the well inserts, and their migration or release of toxins into a circulating stream of RBCs could be quantified and effects measured. The device’s

flexible design provides room for incorporation of other cell types or threaded ports to monitor analytes like dissolved oxygen or RBC NO. Experiments would involve established cell lines and potentially wild type bacteria, so the system would not be a true mimic of *in vivo* conditions, but it could reveal critical interactions between components in whole blood, which would further our understanding of the progression of sepsis.

### 5.2.2 Future of 3D Printed Device for Dynamic Dosing of Bacteria

Considering that no new types of antibiotics have been developed in the last 30 years, we are truly in the post-antibiotic age.<sup>194</sup> It is obvious from the extensive literature on this subject that this problem has been gaining momentum since the inception of antibiotics themselves. From Figure 4.1, it can be seen that antibiotic resistance to penicillin was reported before the drug was even introduced to the general population, and resistance to levofloxacin was observed the same year it was introduced for widespread use.

The charge to “combat antibiotic resistance” is being met. Reportedly, the White House has proposed to double the spending efforts of combating antibiotic resistance to \$1.6 billion in the 2016 fiscal year. This challenge is being met by scientists in many fields, and at the heart of the effort are those whose aim is to further our molecular level understanding of the various microbes we seek to eliminate. Advancement in our basic understanding of microbial function will enable those developing *in vitro* mimics to better recapitulate the *in vivo* condition to facilitate more complex studies.

One example of a tool developed to mimic *in vivo* dosing was presented in Chapter 4. The potential for this particular device to aid in the elucidation of mechanisms that microbes employ to develop antibiotic resistance is high. The study of biofilm response to dosing profiles is another application where the 3D printed device could be useful. Initial flow cytometry data of the dosed samples from Chapter 4 indicate that viable but not culturable (VBNC) cell types are generated after the applied dose profile as indicated in Figure 5.1.

After applying the dose curve with a  $C_{max}$  of  $68.0 \pm 7.1 \mu\text{M}$  to 75  $\mu\text{L}$  of purified *E. coli*,

the viability of the sample was investigated using flow cytometry. Nuclear stains SYTO 9 (2  $\mu$ M, Invitrogen) and propidium iodide (PI, 30  $\mu$ M, Sigma) were added to 1/10 diluted samples and were allowed to incubate at room temperature shielded from light for 15 minutes. After incubation, the samples were run on the flow cytometer (BD Accuri C6).

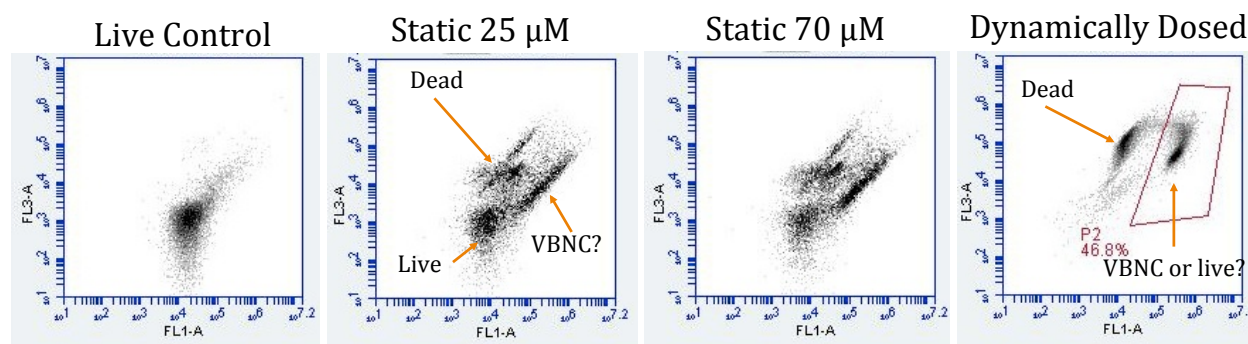


**Figure 5.1** Dot plots of *E. coli* samples from dosing experiments. The x-axis represents the fluorescence signal from SYTO 9, a nuclear stain that is membrane permeable, which allows labeling of all bacteria. The y-axis represents the fluorescence signal from PI, which is only permeable to cells with compromised membranes. From the live control, it is clear there is a single distribution of cells, which some potentially dead or dying portion. The statically dosed samples look similar, and it is clear from their dot plots that at least 3 separate distributions of cells exist: live, dead, and viable but not culturable. For the dynamically dosed sample, it appears that VBNC and dead bacteria are present in the sample. This could explain why nearly a full kill is observed on the dynamically dosed sample in Chapter 4.

There are other challenges to solving the problem of antibiotic resistance than that of simply identifying new drug targets on microbes. One foreseeable issue is the mounting evidence that the non-lethal microbes that reside in our guts may actually play a critical role in our overall health. The drugs developed to combat resistance will have to somehow take the human gut's microbiome into consideration. Another risk is that the suite of new drugs developed to combat microbial resistance will promote further resistance in microbial populations. Given the trend since the introduction of penicillin, this is a reality to seriously consider. The prevalence of antibiotic resistance worldwide is a testament to the evolutionary powers of the various microbes living not only among but within us.



"Piled Higher and Deeper" by Jorge Cham  
www.phdcomics.com

Figure 5.2 "Piled Higher and Deeper" by Jorge Chan. www.phdcomics.com

## REFERENCES



## REFERENCES

- [1] M. D. Brennan, M. L. Rexius-Hall, L. J. Elgass and D. T. Eddington, *Lab on a Chip*, 2014, **14**, 4305–4318.
- [2] S.-P. Hung, J. H. Ho, Y.-R. V. Shih, T. Lo and O. K. Lee, *Journal of Orthopaedic Research*, 2012, **30**, 260–266.
- [3] A. Mohyeldin, T. Garzon-Muvdi and A. Quinones-Hinojosa, *Cell Stem Cell*, 2010, **7**, 150–161.
- [4] A. Carreau, B. E. Hafny-Rahbi, A. Matejuk, C. Grillon and C. Kieda, *Journal of Cellular and Molecular Medicine*, 2011, **15**, 1239–1253.
- [5] S. Y. Lockwood, J. L. Erkal and D. M. Spence, *Nitric Oxide*, 2014, **38**, 1–7.
- [6] J. L. Erkal, A. Selimovic, B. C. Gross, S. Y. Lockwood, E. L. Walton, S. McNamara, R. S. Martin and D. M. Spence, *Lab on a Chip*, 2014, **14**, 2023–2032.
- [7] A. Selimovic, J. L. Erkal, D. M. Spence and R. S. Martin, *The Analyst*, 2014, **139**, 5686–5694.
- [8] Centers for Disease Control, *Antibiotic Resistance Threats in the United States*, 2013.
- [9] A. P. Magiorakos, A. Srinivasan, R. B. Carey, Y. Carmeli, M. E. Falagas, C. G. Giske, S. Harbarth, J. F. Hindler, G. Kahlmeter, B. Olsson-Liljequist, D. L. Paterson, L. B. Rice, J. Stelling, M. J. Struelens, A. Vatopoulos, J. T. Weber and D. L. Monnet, *Clinical Microbiology and Infection*, 2012, **18**, 268–281.
- [10] J. J. S. Cadwell, *Advances in Pharmacoepidemiology and Drug Safety*, 2012, **1**, 2167–1052.
- [11] A. R. Pries, T. W. Secomb, T. Gessner, M. B. Sperandio, J. F. Gross and P. Gaehtgens, *Circulation Research*, 1994, **75**, 904–915.
- [12] A. R. Pries, T. W. Secomb, P. Gaehtgens and J. F. Gross, *Circulation Research*, 1990, **67**, 826–834.
- [13] B. Klitzman and B. R. Duling, *American Journal of Physiology - Heart and Circulatory Physiology*, 1979, **237**, H481–H490.
- [14] D. H. Damon and B. R. Duling, *Microvascular Research*, 1984, **27**, 81–95.
- [15] D. Shemin and D. Rittenberg, *The Journal of Biological Chemistry*, 1946, **166**, 627–36.
- [16] R. S. Sprague, A. H. Stephenson and M. L. Ellsworth, *Trends in Endocrinology and Metabolism*, 2007, **18**, 350–355.
- [17] V. Bennett and D. M. Gilligan, *Annual Review of Cell Biology*, 1993, **9**, 27–66.

- [18] J. P. Landers, *Handbook of capillary and microchip electrophoresis and associated microtechniques*, CRC Press, 2007.
- [19] L. Bogar, A. Matrai, M. Tekeres, P. T. Flute and J. A. Dormandy, *Pediatric Research*, 1985, **19**, 1132–1132.
- [20] R. S. Sprague, J. J. Olearczyk, D. M. Spence, A. H. Stephenson, R. W. Sprung and A. J. Lonigro, *American Journal of Physiology. Heart and Circulatory Physiology*, 2003, **285**, H693–700.
- [21] J. Edwards, R. Sprung, R. Sprague and D. Spence, *The Analyst*, 2001, **126**, 1257–60.
- [22] M. Levine, D. L. Oxender and W. D. Stein, *Biochimica et Biophysica Acta - Biophysics including Photosynthesis*, 1965, **109**, 151–163.
- [23] J. Klepper and T. Voit, *European Journal of Pediatrics*, 2002, **161**, 295–304.
- [24] C. Cereser, J. Guichard, J. Draï, E. Bannier, I. Garcia, S. Boget, P. Parvaz and A. Revol, *Journal of Chromatography B: Biomedical Sciences and Applications*, 2001, **752**, 123–132.
- [25] M. Sridharan, S. P. Adderley, E. A. Bowles, T. M. Egan, A. H. Stephenson, M. L. Ellsworth and R. S. Sprague, *American Journal of Physiology - Heart and Circulatory Physiology*, 2010, **299**, H1146–H1152.
- [26] H. H. Dietrich, M. L. Ellsworth, R. S. Sprague and J. Dacey, R. G., *American Journal of Physiology - Heart and Circulatory physiology*, 2000, **278**, H1294–8.
- [27] M. L. Ellsworth, T. Forrester, C. G. Ellis and H. H. Dietrich, *The American Journal of Physiology*, 1995, **269**, H2155–H2161.
- [28] R. S. Sprague, M. L. Ellsworth, A. H. Stephenson and A. J. Lonigro, *The American Journal of Physiology*, 1996, **271**, H2717–H2722.
- [29] W. A. Eaton, E. R. Henry, J. Hofrichter and A. Mozzarelli, *Nature Structural and Molecular Biology*, 1999, **6**, 351–358.
- [30] F. B. Jensen, *Acta Physiologica Scandinavica*, 2004, **182**, 215–227.
- [31] M. K. Safo, M. H. Ahmed, M. S. Ghatge and T. Boyiri, *Biochimica et Biophysica Acta - Proteins and Proteomics*, 2011, **1814**, 797–809.
- [32] W. A. Eaton, E. R. Henry, J. Hofrichter, S. Bettati, C. Viappiani and A. Mozzarelli, *IUBMB Life*, 2007, **59**, 586–599.
- [33] M. F. Perutz, *Nature*, 1970, **228**, 726–734.
- [34] A. Faris and D. M. Spence, *The Analyst*, 2008, **133**, 678–82.
- [35] Y. Yuan, M. F. Tam, V. Simplaceanu and C. Ho, *Chemical Reviews*, 2015, **115**, 1702–1724.
- [36] J. W. Severinghaus, *Journal of Applied Physiology*, 1979, **46**, 599–602.

- [37] W. S. Sly and P. Y. Hu, *Annual Review of Biochemistry*, 1995, **64**, 375–401.
- [38] A. Ohlsson, W. A. Cumming, A. Paul and W. S. Sly, *Pediatrics*, 1986, **77**, 371–381.
- [39] D. E. Roth, P. J. Venta, R. E. Tashian and W. S. Sly, *Proceedings of the National Academy of Sciences of the United States of America*, 1992, **89**, 1804–1808.
- [40] G. Kifor, M. Toon, A. Janoshazi and A. K. Solomon, *The Journal of Membrane Biology*, 1993, **134**, 169–179.
- [41] J. W. Vince and R. A. F. Reithmeier, *Journal of Biological Chemistry*, 1998, **273**, 28430–28437.
- [42] S. C. Frost and R. McKenna, *Carbonic Anhydrase: Mechanism, Regulation, Links to Disease, and Industrial Applications*, Springer Science and Business Media, 2013, vol. 75.
- [43] H. Chu, A. Breite, P. Ciraolo, R. S. Franco and P. S. Low, *Blood*, 2008, **111**, 932–938.
- [44] J. J. Olearczyk, A. H. Stephenson, A. J. Lonigro and R. S. Sprague, *Medical Science Monitor*, 2001, **7**, 669–674.
- [45] R. S. Sprague, M. L. Ellsworth, A. H. Stephenson, M. E. Kleinhenz and A. J. Lonigro, *The American Journal of Physiology*, 1998, **275**, H1726–32.
- [46] R. S. Sprague, A. H. Stephenson, R. A. Dimmitt, N. L. Weintraub, C. A. Branch, L. McMurdo, A. J. Lonigro and N. A. Weintraub, *American Journal of Physiology-Heart and Circulatory Physiology*, 1995, **269**, H1941–H1948.
- [47] R. Sprung, R. Sprague and D. Spence, *Analytical Chemistry*, 2002, **74**, 2274–8.
- [48] L. J. Ignarro, R. E. Byrns, G. M. Buga and K. S. Wood, *Circulation Research*, 1987, **61**, 866–879.
- [49] S. T. Halpin and D. M. Spence, *Analytical Chemistry*, 2010, **82**, 7492–7497.
- [50] A. J. Gow, B. P. Luchsinger, J. R. Pawloski, D. J. Singel and J. S. Stamler, *Proceedings of the National Academy of Sciences*, 1999, **96**, 9027–9032.
- [51] L. Jia, C. Bonaventura, J. Bonaventura and J. S. Stamler, *Nature*, 1996, **380**, 221–226.
- [52] D. L. Diesen, D. T. Hess and J. S. Stamler, *Circulation Research*, 2008, **103**, 545–553.
- [53] J. R. Pawloski, D. T. Hess and J. S. Stamler, *Nature*, 2001, **409**, 622–626.
- [54] J. S. Stamler, L. Jia, J. P. Eu, T. J. McMahon, I. T. Demchenko, J. Bonaventura, K. Gernert and C. A. Piantadosi, *Science*, 1997, **276**, 2034–2037.
- [55] T. J. McMahon, A. E. Stone, J. Bonaventura, D. J. Singel and J. S. Stamler, *Journal of Biological Chemistry*, 2000, **275**, 16738–16745.
- [56] N. S. Bryan, T. Rassaf, J. Rodriguez and M. Feelisch, *Nitric Oxide*, 2004, **10**, 221–228.

- [57] T. Rassaf, N. S. Bryan, R. E. Maloney, V. Specian, M. Kelm, B. Kalyanaraman, J. Rodriguez and M. Feelisch, *Nature Medicine*, 2003, **9**, 481–482.
- [58] M. T. Gladwin, J. R. Lancaster, B. A. Freeman and A. N. Schechter, *Nature Medicine*, 2003, **9**, 496–500.
- [59] A. J. Hobbs, M. T. Gladwin, R. P. Patel, D. L. H. Williams and A. R. Butler, *Trends in Pharmacological Sciences*, 2002, **23**, 406–411.
- [60] T. J. McMahon, R. E. Moon, B. P. Lusching, M. S. Carraway, A. E. Stone, B. W. Stolp, A. J. Gow, J. R. Pawloski, P. Watke and D. J. Singel, *Nature Medicine*, 2002, **8**, 711–717.
- [61] T. S. Isbell, C.-W. Sun, L.-C. Wu, X. Teng, D. A. Vitturi, B. G. Branch, C. G. Kevil, N. Peng, J. M. Wyss and N. Ambalavanan, *Nature Medicine*, 2008, **14**, 773–777.
- [62] M. T. Gladwin, J. H. Shelhamer, A. N. Schechter, M. E. Pease-Fye, M. A. Waclawiw, J. A. Panza, F. P. Ognibene and R. O. Cannon, *Proceedings of the National Academy of Sciences*, 2000, **97**, 11482–11487.
- [63] M. P. Doyle, R. A. Pickering, T. M. DeWeert, J. W. Hoekstra and D. Pater, *Journal of Biological Chemistry*, 1981, **256**, 12393–12398.
- [64] T. Lauer, M. Preik, T. Rassaf, B. E. Strauer, A. Deussen, M. Feelisch and M. Kelm, *Proceedings of the National Academy of Sciences*, 2001, **98**, 12814–12819.
- [65] K. Cosby, K. S. Partovi, J. H. Crawford, R. P. Patel, C. D. Reiter, S. Martyr, B. K. Yang, M. A. Waclawiw, G. Zalos, X. Xu, K. T. Huang, H. Shields, D. B. Kim-Shapiro, A. N. Schechter and R. O. Cannon, *Nature Medicine*, 2003, **9**, 1498–505.
- [66] M. Kelm and J. Schrader, *Circulation Research*, 1990, **66**, 1561–1575.
- [67] T. S. Hakim, K. Sugimori, E. M. Camporesi and G. Anderson, *Physiological Measurement*, 1996, **17**, 267.
- [68] M. Kelm, M. Feelisch, A. Deuen, J. Schrader and B. E. Strauer, *Journal of Cardiovascular Pharmacology*, 1991, **17**, S95.
- [69] G. R. Bergfeld and T. Forrester, *Cardiovascular Research*, 1992, **26**, 40–7.
- [70] A. Miseta, P. Bogner, E. Berenyi, M. Kellermayer, C. Galambos, D. N. Wheatley and I. L. Cameron, *Biochimica et Biophysica Acta (BBA)-Molecular Cell Research*, 1993, **1175**, 133–139.
- [71] R. G. Bogle, S. B. Coade, S. Moncada, J. D. Pearson and G. E. Mann, *Biochemical and Biophysical Research Communications*, 1991, **180**, 926–932.
- [72] D. J. Allsup and M. R. Boarder, *Molecular Pharmacology*, 1990, **38**, 84–91.
- [73] S. F. Liu, D. G. McCormack, T. W. Evans and P. J. Barnes, *Journal of Pharmacology and Experimental Therapeutics*, 1989, **251**, 1204–1210.

- [74] H. H. Dalziel and D. P. Westfall, *Pharmacological Reviews*, 1994, **46**, 449–466.
- [75] R. O. Dull, J. M. Tarbell and P. F. Davies, *Journal of Vascular Research*, 1992, **29**, 410–419.
- [76] D. A. Houston, G. Burnstock and P. M. Vanhoutte, *Journal of Pharmacology and Experimental Therapeutics*, 1987, **241**, 501–506.
- [77] C. Kennedy, D. Delbro and G. Burnstock, *European Journal of Pharmacology*, 1985, **107**, 161–168.
- [78] M. Raththagala, W. Karunarathne, M. Kryziniak, J. McCracken and D. M. Spence, *European Journal of Pharmacology*, 2010, **645**, 32–38.
- [79] J. A. Meyer, J. M. Froelich, G. E. Reid, W. K. A. Karunarathne and D. M. Spence, *Diabetologia*, 2008, **51**, 175–182.
- [80] R. S. Sprague, A. H. Stephenson, M. L. Ellsworth, C. Keller and A. J. Lonigro, *Experimental Biology and Medicine*, 2001, **226**, 434–439.
- [81] S. Letourneau, L. Hernandez, A. N. Faris and D. M. Spence, *Analytical and Bioanalytical Chemistry*, 2010, **397**, 3369–3375.
- [82] A. K. Mack and G. J. Kato, *The International Journal of Biochemistry and Cell Biology*, 2006, **38**, 1237–1243.
- [83] D. C. Rees, T. N. Williams and M. T. Gladwin, *The Lancet*, 2010, **376**, 2018–2031.
- [84] L. Pauling, H. A. Itano, S. J. Singer and I. C. Wells, *Science*, 1949, **110**, 543–548.
- [85] F. A. Ferrone, M. Ivanova and R. Jasuja, *Biophysical Journal*, 2002, **82**, 399–406.
- [86] F. A. Ferrone and M. A. Rotter, *Journal of Molecular Recognition*, 2004, **17**, 497–504.
- [87] J. B. Herrick, *The Yale Journal of Biology and Medicine*, 2000, **74**, 179–184.
- [88] G. R. Serjeant, *British Journal of Haematology*, 2010, **151**, 425–429.
- [89] R. S. Franco, J. Lohmann, E. B. Silberstein, G. Mayfield-Pratt, M. Palascak, T. A. Nemeth, C. H. Joiner, M. Weiner and D. L. Rucknagel, *Journal of Clinical Investigation*, 1998, **101**, 2730.
- [90] P. R. McCurdy, L. Mahmood and A. S. Sherman, *Blood*, 1975, **45**, 273–279.
- [91] A. J. J. Wood and M. H. Steinberg, *New England Journal of Medicine*, 1999, **340**, 1021–1030.
- [92] O. S. Platt, *New England Journal of Medicine*, 2008, **358**, 1362–1369.
- [93] S. Charache, M. L. Terrin, R. D. Moore, G. J. Dover, F. B. Barton, S. V. Eckert, R. P. McMahon and D. R. Bonds, *The New England Journal of Medicine*, 1995, **332**, 1317–22.

- [94] S. Lanzkron, J. J. Strouse, R. Wilson, M. C. Beach, C. Haywood, H. Park, C. Witkop, E. B. Bass and J. B. Segal, *Annals of Internal Medicine*, 2008, **148**, 939–955.
- [95] M. H. Steinberg, F. Barton, O. Castro and et al., *JAMA*, 2003, **289**, 1645–1651.
- [96] R. E. Ware, *Blood*, 2010, **115**, 5300–5311.
- [97] I. H. Krakoff, N. C. Brown and P. Reichard, *Cancer Research*, 1968, **28**, 1559–1565.
- [98] C. W. Young and S. Hodas, *Science*, 1964, **146**, 1172–1174.
- [99] W. N. Fishbein and P. P. Carbone, *Science*, 1963, **142**, 1069–1070.
- [100] B. Stearns, K. A. Losee and J. Bernstein, *Journal of Medicinal Chemistry*, 1963, **6**, 201–201.
- [101] A. S. Boyd and K. H. Neldner, *Journal of the American Academy of Dermatology*, 1991, **25**, 518–524.
- [102] S. Charache, G. J. Dover, R. D. Moore, S. Eckert, S. K. Ballas, M. Koshy, P. F. Milner, E. P. Orringer, J. Phillips, G. and O. S. Platt, *Blood*, 1992, **79**, 2555–2565.
- [103] A. Ferster, P. Tahriri, C. Vermynen, G. Sturbois, F. Corazza, P. Fondu, C. Devalck, M. F. Dresse, W. Feremans, K. Hunninck, M. Toppet, P. Philippet, C. Van Geet and E. Sariban, *Blood*, 2001, **97**, 3628–3632.
- [104] J. S. Hankins, R. E. Ware, Z. R. Rogers, L. W. Wynn, P. A. Lane, J. P. Scott and W. C. Wang, *Blood*, 2005, **106**, 2269–2275.
- [105] S. A. Zimmerman, W. H. Schultz, J. S. Davis, C. V. Pickens, N. A. Mortier, T. A. Howard and R. E. Ware, *Blood*, 2003, **103**, 2039–2045.
- [106] T. R. Kinney, R. W. Helms, E. E. O’Branski, K. Ohene-Frempong, W. Wang, C. Daeschner, E. Vichinsky, R. Redding-Lallinger, B. Gee, O. S. Platt and R. E. Ware, *Blood*, 1999, **94**, 1550–1554.
- [107] M. A. el Hazmi, A. S. Warsy, A. al Momen and M. Harakati, *Acta Haematologica*, 1992, **88**, 170–4.
- [108] K. R. Bridges, G. D. Barabino, C. Brugnara, M. R. Cho, G. W. Christoph, G. Dover, B. M. Ewenstein, D. E. Golan, C. R. G. Guttmann, J. Hofrichter, R. V. Mulkern, B. Zhang and W. A. Eaton, *Blood*, 1996, **88**, 4701–4710.
- [109] W. A. Eaton and J. Hofrichter, *Science*, 1995, **268**, 1142–1143.
- [110] F. H. M. D. Epstein and H. F. M. D. Bunn, *The New England Journal of Medicine*, 1997, **337**, 762–769.
- [111] C. T. Noguchi, G. P. Rodgers, G. Serjeant and A. N. Schechter, *New England Journal of Medicine*, 1988, **318**, 96–99.

- [112] M. Rotter, A. Aprelev, K. Adachi and F. A. Ferrone, *Journal of Molecular Biology*, 2005, **347**, 1015–1023.
- [113] Z. Huang, J. G. Louderback, S. B. King, S. K. Ballas and D. B. Kim-Shapiro, *American Journal of Hematology*, 2001, **67**, 151–6.
- [114] S. K. Ballas, G. J. Dover and S. Charache, *American Journal of Hematology*, 1989, **32**, 104–111.
- [115] A. R. Wheeler, W. R. Thronset, R. J. Whelan, A. M. Leach, R. N. Zare, Y. H. Liao, K. Farrell, I. D. Manger and A. Daridon, *Analytical Chemistry*, 2003, **75**, 3581–3586.
- [116] M. A. McClain, C. T. Culbertson, S. C. Jacobson and J. M. Ramsey, *Analytical Chemistry*, 2001, **73**, 5334–5338.
- [117] P. J. Lee, P. J. Hung, R. Shaw, L. Jan and L. P. Lee, *Applied Physics Letters*, 2005, **86**, –.
- [118] S. Chung, R. Sudo, P. J. Mack, C.-R. Wan, V. Vickerman and R. D. Kamm, *Lab on a Chip*, 2009, **9**, 269–275.
- [119] J.-W. Choi, R. Wicker, S.-H. Lee, K.-H. Choi, C.-S. Ha and I. Chung, *Journal of Materials Processing Technology*, 2009, **209**, 5494–5503.
- [120] B. G. Chung, L. A. Flanagan, S. W. Rhee, P. H. Schwartz, A. P. Lee, E. S. Monuki and N. L. Jeon, *Lab on a Chip*, 2005, **5**, 401–406.
- [121] I. Meyvantsson and D. J. Beebe, *Annual Review of Analytical Chemistry*, 2008, **1**, 423–449.
- [122] A. S. Popel and P. C. Johnson, *Annual Review of Fluid Mechanics*, 2005, **37**, 43–69.
- [123] T. G. Papaioannou and C. Stefanadis, *Hellenic Journal of Cardiology*, 2005, **46**, 9–15.
- [124] D. T. Covas, I. de Lucena Angulo, P. V. B. Palma and M. A. Zago, *Haematologica*, 2004, **89**, 273–280.
- [125] A. A. Daak, K. Ghebremeskel, M. I. Elbashir, A. Bakhita, Z. Hassan and M. A. Crawford, *Journal of Lipids*, 2011, **2011**, 1–8.
- [126] M. Nahavandi, F. Tavakkoli, R. M. Millis, M. Q.-Wyche, M. J. Habib and N. Tavakoli, *Hematology*, 2006, **11**, 291–294.
- [127] A. Scozzafava and C. T. Supuran, *Bioorganic and Medicinal Chemistry*, 2003, **11**, 2241–2246.
- [128] D. C. Duffy, J. C. McDonald, O. J. A. Schueller and G. M. Whitesides, *Analytical Chemistry*, 1998, **70**, 4974–4984.
- [129] J. C. McDonald, D. C. Duffy, J. R. Anderson, D. T. Chiu, H. Wu, O. J. A. Schueller and G. M. Whitesides, *Electrophoresis*, 2000, **21**, 27–40.

- [130] H. James, M. Nahavandi, M. Q. Wyche and R. E. Taylor, *Journal of Chromatography B*, 2006, **831**, 42–47.
- [131] D. K. Scott, K. Neville and U. Garg, in *Determination of Hydroxyurea in Serum or Plasma Using Gas Chromatography-Mass Spectrometry (GC-MS)*, ed. U. Garg and C. A. Hammett-Stabler, Humana Press, 2010, vol. 603, book section 26, pp. 279–287.
- [132] P. S. Becker, C. M. Cohen and S. E. Lux, *Journal of Biological Chemistry*, 1986, **261**, 4620–4628.
- [133] P. Kleinbongard, R. Schulz, T. Rassaf, T. Lauer, A. Dejam, T. Jax, I. Kumara, P. Gharini, S. Kabanova, B. Ozuyaman, H. G. Schnurch, A. Godecke, A. A. Weber, M. Robenek, H. Robenek, W. Bloch, P. Rosen and M. Kelm, *Blood*, 2006, **107**, 2943–51.
- [134] K. M. Naik, M. M. Alagur and S. T. Nandibewoor, *Analytical Methods*, 2013, **5**, 6947–6953.
- [135] N. Shaklai, J. Yguerabide and H. M. Ranney, *Biochemistry*, 1977, **16**, 5585–5592.
- [136] R. K. Kaul and H. Kohler, *Klinische Wochenschrift*, 1983, **61**, 831–837.
- [137] J. Eisinger, J. Flores and J. M. Salhany, *Proceedings of the National Academy of Sciences*, 1982, **79**, 408–412.
- [138] J. Eisinger, J. Flores and R. M. Bookchin, *Journal of Biological Chemistry*, 1984, **259**, 7169–7177.
- [139] J. Eisinger and J. Flores, *Biophysical Journal*, 1982, **37**, 6–7.
- [140] G. Chetrite and R. Cassoly, *Journal of Molecular Biology*, 1985, **185**, 639–644.
- [141] J. A. Walder, R. Chatterjee, T. L. Steck, P. S. Low, G. F. Musso, E. T. Kaiser, P. H. Rogers and A. Arnone, *Journal of Biological Chemistry*, 1984, **259**, 10238–10246.
- [142] G. Duchon and H. B. Collier, *The Journal of Membrane Biology*, 1971, **6**, 138–157.
- [143] H. M. Anderson and J. C. Turner, *Journal of Clinical Investigation*, 1960, **39**, 1.
- [144] J. F. Hoffman, *The Journal of General Physiology*, 1958, **42**, 9–28.
- [145] N. Shaklai and H. Abrahamsi, *Biochemical and Biophysical Research Communications*, 1980, **95**, 1105–1112.
- [146] B. C. Gross, J. L. Erkal, S. Y. Lockwood, C. Chen and D. M. Spence, *Analytical Chemistry*, 2014, **86**, 3240–3253.
- [147] L. Hieu, N. Zlatov, J. Vander Sloten, E. Bohez, L. Khanh, P. Binh, P. Oris and Y. Toshev, *Assembly Automation*, 2005, **25**, 284–292.
- [148] C. Kermer, M. Rasse, G. Lagogiannis, G. Undt, A. Wagner and W. Millesi, *Journal of Cranio-Maxillofacial Surgery*, 1998, **26**, 360–362.



- [149] P. Webb, *Journal of Medical Engineering and Technology*, 2000, **24**, 149–153.
- [150] F. P. Melchels, J. Feijen and D. W. Grijpma, *Biomaterials*, 2010, **31**, 6121–6130.
- [151] N. A. Waterman and P. Dickens, *World Class Design to Manufacture*, 1994, **1**, 27–36.
- [152] D. T. Pham and R. S. Gault, *International Journal of Machine Tools and Manufacture*, 1998, **38**, 1257–1287.
- [153] P. Tek, T. C. Chiganos, J. S. Mohammed, D. T. Eddington, C. P. Fall, P. Ifft and P. J. Rousche, *Journal of Neuroscience Methods*, 2008, **172**, 263–269.
- [154] V. Dragone, V. Sans, M. Rosnes, P. Kitson and L. Cronin, *Beilstein Journal of Organic Chemistry*, 2013, **9**, 951–959.
- [155] P. Kitson, M. Symes, V. Dragone and L. Cronin, *Chemical Science*, 2013, **4**, 3099–3103.
- [156] P. Kitson, M. Rosnes, V. Sans, V. Dragone and L. Cronin, *Lab on a Chip*, 2012, **12**, 3267–3271.
- [157] J. S. Mathieson, M. H. Rosnes, V. Sans, P. J. Kitson and L. Cronin, *Beilstein Journal of Nanotechnology*, 2013, **4**, 285–291.
- [158] M. Symes, P. Kitson, J. Yan, C. Richmond, G. Cooper, R. Bowman, T. Vilbrandt and L. Cronin, *Nature Chemistry*, 2012, **4**, 349–354.
- [159] Y. Sameenoi, M. M. Mensack, K. Boonsong, R. Ewing, W. Dungchai, O. Chailapakul, D. M. Cropek and C. S. Henry, *The Analyst*, 2011, **136**, 3177–3184.
- [160] C. Amatore, S. Arbault, Y. Chen, C. Crozatier and I. Tapsoba, *Lab on a Chip*, 2007, **7**, 233–238.
- [161] K. L. Adams, M. Puchades and A. G. Ewing, *Annual Review of Analytical Chemistry*, 2008, **1**, 329–329.
- [162] S. K. Sia and G. M. Whitesides, *Electrophoresis*, 2003, **24**, 3563–3576.
- [163] L. Gorton, *Electroanalysis*, 1995, **7**, 23–45.
- [164] E. Bakker, *Analytical chemistry*, 2004, **76**, 3285–3298.
- [165] R. Pomeroy and H. D. Kirschman, *Industrial and Engineering Chemistry Analytical Edition*, 1945, **17**, 715–716.
- [166] L. R. Pomeroy, J. E. Sheldon and W. M. Sheldon, *Applied and Environmental Microbiology*, 1994, **60**, 328–332.
- [167] H. Montgomery, N. S. Thom and A. Cockburn, *Journal of Applied Chemistry*, 1964, **14**, 280–296.
- [168] M. L. Rexius-Hall, G. Mauleon, A. B. Malik, J. Rehman and D. T. Eddington, *Lab on a Chip*, 2014, **14**, 4688–4695.

- [169] S. C. Oppegard, K.-H. Nam, J. R. Carr, S. C. Skaalure and D. T. Eddington, *PLoS ONE*, 2009, **4**, e6891.
- [170] H. Suzuki, A. Sugama and N. Kojima, *Sensors and Actuators B: Chemical*, 1993, **10**, 91–98.
- [171] H. Suzuki, T. Hirakawa, I. Watanabe and Y. Kikuchi, *Analytica Chimica Acta*, 2001, **431**, 249–259.
- [172] G. Jobst, G. Urban, A. Jachimowicz, F. Kohl, O. Tilado, I. Lettenbichler and G. Nauer, *Biosensors and Bioelectronics*, 1993, **8**, 123–128.
- [173] C.-C. Wu, T. Yasukawa, H. Shiku and T. Matsue, *Sensors and Actuators B: Chemical*, 2005, **110**, 342–349.
- [174] I. Klimant and O. S. Wolfbeis, *Analytical Chemistry*, 1995, **67**, 3160–3166.
- [175] M. T. Murtagh, M. R. Shahriari and M. Krihak, *Chemistry of Materials*, 1998, **10**, 3862–3869.
- [176] C. McDonagh, B. D. MacCraith and A. K. McEvoy, *Analytical Chemistry*, 1998, **70**, 45–50.
- [177] Z. Yang, S. Sasaki, I. Karube and H. Suzuki, *Analytica Chimica Acta*, 1997, **357**, 41–49.
- [178] J. R. Lakowicz, *Principles of Fluorescence Spectroscopy*, Springer Science and Business Media, 2007.
- [179] J. W. Severinghaus and P. B. Astrup, *Journal of Clinical Monitoring*, 1986, **2**, 125–139.
- [180] D. Dewulf and A. J. Bard, *Journal of Macromolecular Science - Chemistry*, 1989, **26**, 1205–1209.
- [181] A. Veicsteinas, M. Samaja, M. Gussoni and P. Cerretelli, *Journal of Applied Physiology*, 1984, **57**, 52–58.
- [182] H. Mairbaur, O. Oelz and P. Bartsch, *Journal of Applied Physiology*, 1993, **74**, 40–48.
- [183] E. G. Brown, R. W. Krouskop, F. E. McDonnell, C. C. Monge and R. M. Winslow, *Journal of Applied Physiology*, 1985, **58**, 1383–1389.
- [184] R. M. Winslow, C. C. Monge, N. J. Statham, C. G. Gibson, S. Charache, J. Whitembury, O. Moran and R. L. Berger, *Journal of Applied Physiology*, 1981, **51**, 1411–1416.
- [185] J. Metcalfe, D. S. Dhindsa, M. J. Edwards and A. Mourdjinis, *Circulation Research*, 1969, **25**, 47–51.
- [186] A. R. Pries and T. W. Secomb, in *Blood Flow in Microvascular Networks*, John Wiley and Sons, Inc., 2011.
- [187] B. J. Privett, J. H. Shin and M. H. Schoenfisch, *Chemical Society Reviews*, 2010, **39**, 1925–1935.

- [188] Y. Lee, B. K. Oh and M. E. Meyerhoff, *Analytical Chemistry*, 2004, **76**, 536–544.
- [189] J. M. Salhany, K. A. Cordes and E. D. Gaines, *Biochemistry*, 1980, **19**, 1447–1454.
- [190] H. Passow, in *Molecular aspects of band 3 protein-mediated anion transport across the red blood cell membrane*, Springer, 1986, pp. 61–203.
- [191] D. Jay and L. Cantley, *Annual Review of Biochemistry*, 1986, **55**, 511–538.
- [192] Y. Liu, C. Chen, S. Summers, W. Medawala and D. Spence, *Integrative Biology*, 2015.
- [193] Y. Wang, A. Giebink and D. M. Spence, *Integrative Biology*, 2014, **6**, 65–75.
- [194] The World Health Organization, *Antimicrobial Resistance Global Report on Surveillance*, report, 2014.
- [195] The White House, *National Strategy for Combating Antibiotic-Resistance Bacteria*, 2014.
- [196] J. A. DiMasi, R. W. Hansen and H. G. Grabowski, *Journal of Health Economics*, 2003, **22**, 151–185.
- [197] C. P. Adams and V. V. Brantner, *Health Affairs*, 2006, **25**, 420–428.
- [198] P. G. Ambrose, S. M. Bhavnani, C. M. Rubino, A. Louie, T. Gumbo, A. Forrest and G. L. Drusano, *Clinical Infectious Diseases*, 2007, **44**, 79–86.
- [199] E. I. Nielsen and L. E. Friberg, *Pharmacological Reviews*, 2013, **65**, 1053–1090.
- [200] P. M. Shah, *Journal of Antimicrobial Chemotherapy*, 1981, **8**, 93–99.
- [201] S. Y. Lockwood, *Thesis*, Michigan State University, 2014.
- [202] M. Furlanut, L. Brollo, E. Lugatti, E. Di Qual, F. Dolcet, G. Talmassons and F. Pea, *Journal of Antimicrobial Chemotherapy*, 2003, **51**, 101–106.
- [203] J. M. Blondeau, *Survey of Ophthalmology*, 2004, **49**, S73–S78.
- [204] H. Zhu, R. Zennadi, B. X. Xu, J. P. Eu, J. A. Torok, M. J. Telen and T. J. McMahon, *Critical Care Medicine*, 2011, **39**, 2478–2486.
- [205] Q. Ramadan and M. A. M. Gijs, *Lab on a Chip*, 2015, **15**, 614–636.
- [206] R. M. Cooper, D. C. Leslie, K. Domansky, A. Jain, C. Yung, M. Cho, S. Workman, M. Super and D. E. Ingber, *Lab on a Chip*, 2014, **14**, 182–188.
- [207] W.-H. Chang, C.-H. Wang, S.-Y. Yang, Y.-C. Lin, J.-J. Wu, M. S. Lee and G.-B. Lee, *Lab on a Chip*, 2014, **14**, 3376–3384.
- [208] D. Cai, M. Xiao, P. Xu, Y.-C. Xu and W. Du, *Lab on a Chip*, 2014, **14**, 3917–3924.
- [209] S. Bouguelia, Y. Roupioz, S. Slimani, L. Mondani, M. G. Casabona, C. Durmort, T. Vernet, R. Calemczuk and T. Livache, *Lab on a Chip*, 2013, **13**, 4024–4032.

- [210] K. A. Wichterman, A. E. Baue and I. H. Chaudry, *Journal of Surgical Research*, 1980, **29**, 189–201.
- [211] J. A. Buras, B. Holzmann and M. Sitkovsky, *Nature Reviews Drug Discovery*, 2005, **4**, 854–865.
- [212] D. Rittirsch, L. M. Hoesel and P. A. Ward, *Journal of Leukocyte Biology*, 2007, **81**, 137–143.
- [213] R. D. Piper, M. Pitt-Hyde, F. Li, W. J. Sibbald and R. F. Potter, *American Journal of Respiratory and Critical Care Medicine*, 1996, **154**, 931–937.
- [214] L. B. Hinshaw, *Critical Care Medicine*, 1996, **24**, 1072–1078.
- [215] M. Piagnerelli, K. Z. Boudjeltia, M. Vanhaeverbeek and J. L. Vincent, *Intensive Care Medicine*, 2003, **29**, 1052–1061.
- [216] O. Baskurt, D. Gelmont and H. Meiselman, *American Journal of Respiratory and Critical Care Medicine*, 1998, **157**, 421–427.
- [217] M. E. Astiz, G. E. DeGent, R. Y. Lin and E. C. Rackow, *Critical Care Medicine*, 1995, **23**, 265–271.
- [218] R. J. Powell, G. W. Machiedo and B. F. Rush Jr, *The American surgeon*, 1993, **59**, 65–68.
- [219] T. C. Hurd, K. S. Dasmahapatra, B. F. Rush and G. W. Machiedo, *Archives of Surgery*, 1988, **123**, 217–220.
- [220] P. C. Yodice, M. E. Astiz, B. M. Kurian, R. Y. Lin and E. C. Rackow, *American Journal of Respiratory and Critical Care Medicine*, 1997, **155**, 38–42.
- [221] J. E. Langenfeld, D. H. Livingston and G. W. Machiedo, *Surgery*, 1991, **110**, 398–403.
- [222] T. W. Chung, E. A. O’Rear, T. L. Whitsett, L. B. Hinshaw and M. A. Smith, *Circulatory Shock*, 1991, **33**, 178–182.